Development and Characterization of Absolute Dosimeters for Kilovoltage and Higher Energy Radiation

By

Emily J. King

A dissertation submitted in partial fulfillment of
the requirements for the degree of

Doctor of Philosophy
(Medical Physics)

at the
University of Wisconsin – Madison
2022

Date of final oral examination: 1/20/2022

This dissertation is approved by the following members of the Final Oral Committee:

Larry A. DeWerd, Professor, Medical Physics
Wesley S. Culberson, Associate Professor, Medical Physics
Bryan P. Bednarz, Associate Professor, Medical Physics
Michael A. Speidel, Associate Professor, Medical Physics
Douglass L. Henderson, Professor, Engineering Physics

Abstract

Energy dependent dosimeters used in clinics and research laboratories require calibration in a known radiation field of a closely matching energy to the radiation the dosimeters will be measuring. Primary standards labs, such as NIST in the United States, and secondary standards labs, such as the UW ADCL, have standard x-ray beams and radioactive sources like Cs-137 and Co-60 for the purpose of calibration. The standard x-ray beams established at NIST and matched at the UW ADCL have a maximum energy of 250 keV and the next energy step is Cs-137 which emits gamma rays with energy of 662 keV. There lies a gap in standard photon radiation between 250 keV and 662 keV which is an energy range that is increasingly becoming more commonly used. These applications in the higher energy range include radiobiology cabinet and conformal irradiators, Ir-192 brachytherapy sources, and the replacement of Cs-137 research irradiators with higher energy x-ray irradiators. The main goal of this work was to investigate the establishment of standard x-ray beams in this energy range and the development of the absolute dosimeters needed to establish them.

Outside of primary standards laboratories, a free-air chamber that could measure x-rays in the medium-energy range did not exist prior to this work. The free-air chamber designed, built and benchmarked for this work can measure photons up to 320 keV. To measure higher energy x-rays, known-volume ionization chambers were also established. These chambers typically require ultra-precise machining methods, but this work showed the possibility of establishing these chambers with μCT imaging and electric field modeling of commercial ionization chambers.

An industrial x-ray tube capable of producing x-rays up to 500 keV was used to establish the x-ray beams created in this work. The x-ray tube was modeled in the EGSnrc Monte Carlo code to investigate how filtration affected the x-ray spectra. This allowed for the x-ray beams created to match two common radiobiology irradiators to be matched in spectra as well as maximum energy and half-value layer. High density filters were investigated to establish x-ray beams with higher energies. A standard x-ray beam that lies in the 250-662 keV energy gap was established and possible filter combinations for the effective energy of an x-ray spectrum to be more closely aligned to the emitted gamma ray energies of Ir-192 brachytherapy sources.

Acknowledgements

I would first like to thank my advisor, Dr. Larry DeWerd, for his guidance and support throughout my time in graduate school. Thank you for believing in me since day one and pushing me to be the best student, researcher and physicist I could be. I would also like to thank Dr. Wesley Culberson for his advice, professional guidance, and willingness to always talk shop about free-air chambers. Thank you also to Drs. Bryan Bednarz, Michael Speidel, and Douglass Henderson for their guidance and development of this research and thank you all for still attending my preliminary exam on the day the world shut down.

One of the greatest benefits of the Cal Lab is the plethora of staff willing to assist us in so many ways. Thank you to Jennifer Hull who was my sidekick for this project. I feel like the free-air chamber is just as much your baby as it is mine, and it would never have been finished if it weren't for your tireless work. Words cannot express how indebted I am to you. Thank you to Ben Palmer for his engineering knowledge and forgiveness when I ordered a linear stage a millimeter too long. I also would like to thank Dan Anderson for his invaluable help at each stage of my project, from Monte Carlo to FAC control software. Thank you to Jeff Radtke for his advice on all things electrical and to Leif Lervik for his machining expertise. A final thank you to Keith Kunugi for helping me with a little bit of everything. I would also be remiss if I did not thank the UWADCL customers, whose continued calibration patronage helps support student research in our lab.

The biggest thanks goes to Autumn Walter and Leah Kisling, my best friends during my time in graduate school. I am so grateful for our hour long lunch breaks, wine nights, board games, corn mazes and many more adventures. You were both always there to offer a word of encouragement or a listening ear for me to complain. I am glad the Cal

Lab brought us together and transformed us into lifelong friends. I would also like to extend my gratitude to Natalie Viscariello for being my mentor while she was a student and also laying the groundwork for this project. Thank you to Blake Smith for waving your magic wand on my project aims. Your ability to turn rocks into gems is astounding, but not as astounding as your willingness to help so much with nothing but a thank you in return. Thank you to all the other Cal Lab students, past and present, I have had the privilege to work with: Jon, Sameer, Manik, Charlie, Vimal, Leonard, Lianna, Wil, Nick, Reed, Ash, Andrew, Jacob, Tommy, Jocelyn, Sean, Riley, Karsten, Autumn and Miguel. The camradarie of the Cal Lab is unmatched and each one of you has helped me in some capacity, whether that was working through a tough Monte Carlo problem with me or simply providing friendship during a rough time.

I would not be the person I am today without the support of my friends and family. First, I would like to thank my college roommates Elizabeth, Emma, Meghan, Rachel and Katherine for never losing touch, humoring me when I talk too much about nuclear physics and lending words of encouragement. My deepest gratitude goes to my parents, Greg and Amy King, and my siblings Whitney, Meredith and Landon for their unwavering support. Thank you for helping me move to Madison, visiting on many occasions, Fireball Fridays, and for always cheering me on. I would also like to thank my extended family, including my grandparents, I would not be here today without the foundation you built.

A final thank you to Christopher Dye for sticking by my side as I moved 500 miles away so I could pursue my dreams. Thank for consistently making the 1000 mile round trip journey to visit only for a weekend, being there for every up and down, and helping me keep my eye on the prize. It is through your unconditional love and dedication that I have made it through the gauntlet. I'll meet you at the altar.

Contents

List of Figures

List of Tables

Abbreviations

ADCL	Accredited Dosimetry Calibration Laboratory
CPE	Charge particle equilibrium
EGSnrc	Electron Gamma Shower National Research Council Canada
FAC	Free-air chamber
FWHM	Full-width half-maximum
HC	Homogeneity coefficient
HU	Hounsfield Units
HVL	Half value layer, typically referring to the first half value layer
MCNP6	**M**onte **C**arlo **N**-**P**article transport code **6**
μ**CT**	Micro-Computed Tomography
M-series	Moderately filtered, NIST-matched x-ray beams
NIST	National Institute of Standards and Technology
$\mathbf{N}_k$	Air kerma calibration coefficient
PDD	Percent depth dose
POM	Point of measurement
QVL	Quarter value layer
SSD	Source-to-surface distance
SNR	Signal-to-noise ratio

Chapter 1

Introduction

1.1 Overview

There are three areas of dosimetry standards in the kilovoltage and higher energy range that require attention. These include: radiobiology beams that use x-rays that are not traceable to NIST, the interim standard for Ir-192 brachytherapy sources which requires an interpolated calibration coefficient, and the replacement of Cs-137 sources, which is leading to a need for a higher energy x-ray standard.

The results from radiobiological experiments are dependent on sufficient description of the dose given. There are concerns with both dose calculation accuracy and the adequacy of reporting, which has been discussed over the past few decades [4–7]. High dosimetric precision is necessary due to the high biological uncertainty and steep dose-response curves associated with these experiments. Single field and conformal irradiators are commonly used in radiobiology studies. It is important that their calibration closely follows the TG-61 protocol with a NIST-traceable calibration of their ion chambers [8]. The available standard beams that are traceable to NIST are often at lower tube potentials and use more filtration than the common beams used in radiobiology experiments. This discrepancy leads to a higher uncertainty in the calibration of the cabinet and conformal irradiators, and decreases dosimetric precision.

In the United States, the current procedure for calibrating Ir-192 high-dose rate (HDR) brachytherapy sources utilizes the seven distance technique [9]. An air-equivalent ionization chamber with an interpolated calibration coefficient is used to determine the air kerma strength of a given source [10]. The calibration coefficient must be interpolated between the UW-250M standard x-ray beam and Cs-137 since a NIST-traceable standard beam does not exist at the average energy of Ir-192 brachytherarpy sources.

Lastly, the NNSA's Office of Radiological Security (ORS) is encouraging medical and research facilities to transition from radioactive sources to x-ray irradiators [11]. A standard x-ray beam with a higher energy than the standard UW-250M beam is desired for those facilities that are looking to transition from Cs-137 to x-ray irradiators. There is a wide breadth of research on the comparison of Cs-137 to medium energy x-rays for medical research, particularly for relative biological effectiveness (RBE) studies [12, 13]. However, a comparison of higher energy x-rays to Cs-137 has not been performed. The comparison will become increasingly more critical as the field moves away from the use of radioactive sources.

1.2 Aims of this work

For low- and medium-energy x-rays, dose determination requires traceable measurements of air kerma. NIST has three sets of standard x-ray beams that are matched at secondary standards laboratories: the lightly filtered L-series, the moderately filtered M-series, and the highly filtered H-series. The UWADCL has a matched L-series and M-series. The maximum energy of NIST's standard beams are 300 keV and the maximum energy of the UWADCL's standard beams are 250 keV. These standard x-ray beams are not sufficient for all x-ray applications, especially as higher energy x-rays are being increasingly used. This project addresses the lack of calibration standard x-ray beams in the kilovoltage and higher energy range. The aims of this thesis work were to (1) develop and characterize a free-air chamber and (2) known-volume ionization chambers for absolute air kerma dosimetry for (3) investigating standard x-ray beams for radiobiology irradiators, a high-energy beam comparable to Cs-137, and with an average energy equal to that of Ir-192 brachytherapy sources. It is believed that with the establishment of the standard x-ray beams matching radiobiology irradiators will reduce the uncertainties in the delivered dose for preclinical studies which may improve the efficacy of these studies. Similarly, bridging the gap in standard x-ray beams between the current medium-energy standard x-ray beams and Cs-137 will allow for more accurate calibration of dosimetry equipment in this energy range.

1.3 Description of upcoming chapters

The upcoming chapters present the investigation into calibration standards in the kilovoltage and higher energy range of x-rays.

Chapter 2 provides a description of the absolute dosimetry and its use in x-ray standards. It will describe detector design, operation, and considerations for use in this energy range.

Chapter 3 describes the design process, manufacturing, characterization and verification measurements of the medium-energy FAC. An in-depth analysis of the uncertainty of using the FAC to measure air kerma is presented.

Chapter 4 describes the imaging methods, volume calculation and verification measurements of the known-volume ionization chambers. An in-depth analysis of the uncertainty of measuring air kerma with the known-volume chambers is presented.

Chapter 5 presents the development and validation of a Monte Carlo model of the NDI-451Be x-ray tube. This Monte Carlo model is used to estimate the energy spectra of the x-ray tube to ensure accurate filter development for calibration beams for common radiobiology cabinet and conformal irradiators. This chapter includes the building of those filters and validation with air kerma measurements.

Chapter 6 builds off of the beam model developed in Chapter 5 to develop a standard x-ray beam for high energies and a beam with an average energy equal to Ir-192 brachytherapy sources. The process of choosing the filtration material is presented. Air kerma measurements to characterize the average energy, half-value layer and output are also presented in this chapter.

Chapter 7 provides a final summary and the overall conclusions of this investigation. Potential future directions for further x-ray beam development and improved beam quality accuracy are presented.

Chapter 2

Background and motivation

2.1 Absolute dosimeters

The quantity exposure was first defined by the International Commission on Radiological Units and Measurements (ICRU) in 1928 after nearly two decades of committee work on the subject. The purpose was to quantify the output of an x-ray tube. Exposure is, therefore, only defined for photons and may not be used for particles such as electrons, protons, and neutrons. It is a measure of the ionization abilities of x-ray and gamma radiation and is defined as

$$X = \frac{dQ}{dm}, \tag{2.1}$$

where dQ is the absolute value of the total charge of the ions of one sign produced in air when all of the electrons liberated by photons in a volume, with a mass dm, of air are completely stopped in the air [14]. Exposure can then be converted to other useful measured quantities, such as air kerma, with the equation

$$K_{air} = (\overline{W}/e)[1/(1-g)]\cdot X, \tag{2.2}$$

where $\overline{W}/e$ is the mean energy to create an ion pair and is equal to 33.97 J/C for air [15] and g is the fraction of the energy lost to bremsstrahlung. Air kerma has become the standard quantity for ionization of air stemming from the Technical Report Series (TRS) No. 277 report by the International Atomic Energy Agency (IAEA) in 1987 [16].

Absolute dosimeters allow for a direct measurement of fundamental quantities that are descriptive of the incident radiation, like exposure and air kerma, without first calibrating in a known field [15]. An ionization chamber is capable of absolute measurement when the volume within the chamber is precisely and accurately known so as to determine the mass of air within the chamber. Typical ionization chambers for clinical use require a calibration where the charge reading is related to a known quantity that is ultimately determined through the use of absolute dosimeters.

2.1.1 Free-air chambers

The free-air ionization chamber (FAC) not only satisfies the requirement of being an absolute dosimeter but is also ideal for measuring exposure since the definition requires the measurement of all the ionization produced by collision interactions in *air*. There are two primary types of free-air chambers that are used in laboratories across the world: the parallel-plate type and the cylindrical type. The parallel plate type is used at the National Institute of Technology and Standards (NIST) [17], the National Physical Laboratory(NPL, UK) [18] and the Electrotechnical Laboratory (ETL, Japan) [18] while the cylindrical type is used in Sweden [19] and Taiwan [20]. In 1961, Attix expanded on the cylindrical type by creating the design for a low-energy variable length FAC that has since been employed by the UWMRRC for decades. This low-energy FAC will be referred to as the Attix FAC throughout this thesis [21, 22].

The cylindrical-type free-air chamber works with the same physical principles as the parallel-plate type, only being different in geometry. Therefore, for simplicity, only the parallel-plate chamber will be discussed. An electric field is created between the high-voltage plate and the collector plate, while the guard plates are grounded to assist in producing field uniformity. There is a set of electrically biased wires that encircle the chamber which are the primary method of shaping the electric field and producing uniformity. The plates on either side of the x-ray beam are parallel and equidistant from the beam. The distance of the plates from the beam should be longer than the range of the secondary electrons created in the beam. This defines a collecting volume V', while V is the actual volume where the secondary electrons that are measured originate. The electric field creates paths followed by the positive or negative ions, generated as secondary electrons traverse the air cavity, to the collector plate which is electrically connected to an electrometer.

The definition of exposure requires the mass of the specified volume of air to be calculated. Instead of defining the mass, m, as the mass of the air in V', it is simpler to define it as the mass of the air at the beam-defining aperture which is referred to as the point of measurement (POM). This assumption is valid because each photon that passes through the aperture also passes through V' unless it is attenuated or scattered [15]. If the aperture area is A_0 (m^2) and the fluence entering the aperture is Φ_0 (photons/m^2), then $\Phi_0 A_0$ photons will enter. The fluence decreases according the inverse square law as the beam moves through the chamber and the cross-sectional area of the beam increases proportionally. Therefore the number of photons in V', ΦA, remains constant and is equal to $\Phi_0 A_0$ throughout the entire chamber. The exposure can be calculated simply at point P if the source of the x-rays is far enough that $l/\cos\theta \simeq l$ where l is the length of the collecting volume and θ is the angle the x-ray makes with the central axis [15]. The equation for the exposure in C/kg at point P is therefore

$$X = \frac{Q}{m} e^{\mu x'} = \frac{Q}{l A_0 \rho} e^{\mu x'}, \tag{2.3}$$

where Q is the charge produced in V' (C), μ is the air attenuation coefficient (m^{-1}), x' is the distance from P to P' (m), and ρ is the density of air ($\mathrm{kg/m^3}$) [15].

Since the X-ray beam passes through the entire chamber and not just the volume V, not all electrons will originate in V. Free-air chambers must employ the principle of charge-particle equilibrium (CPE) to account for these electrons. For x-rays of low- or medium-energy (up to 500 keV), the initial angular distribution of the secondary electrons causes most of the electrons to be emitted out of the beam rather than forwards or backwards in the beam, so those electrons are near equally likely to move forward and backward in the chamber [15]. This means that almost all of the electrons that leave the collecting volume will be replaced by electrons entering the collecting volume. Therefore, charge compensation is nearly exact and CPE is achieved. CPE is necessary for measuring exposure in free-air chambers because of the definition requiring the tracking and summing of *all* of the ionization charges created by each secondary electron over its entire range in the specified volume and mass of air. The distance from the vertical boundaries of V' and the walls at each end of the chamber must also be greater than the electron range to preserve CPE and keep electrons from being absorbed in the walls.

2.1.1.1 Correction factor definitions

Correction factors are required to account for imperfections in the collection efficiency of free-air chambers. It is possible for x-rays to be scattered out of the beam before interacting with the air to create secondary electrons. This can contribute to excess ionization in volume V' as shown by $h\nu_1$ and $h\nu_2$ in Figure 2.1. Bremsstrahlung x-rays, $h\nu_3$ in Figure 2.1, can also contribute to the ionization charge collected, but the definition of exposure does not include ionization due to bremsstrahlung. The fraction of the total ionization that is produced by scattered and bremsstrahlung x-rays is subtracted to calculate k_s, so it is always less than 1 to remove excess ionization from the measured exposure. Also, it can be possible that a fraction, k_e, of the ionization can be lost if the walls of the chamber are not adequately separated and electrons are stopped short of their full range. Similarly, k_{sh} accounts for the ionization lost due to electrons hitting the collecting rod before fully ionizing. The k_e and k_{sh} quantities are always greater than or equal to 1 to add in the lost ionization to the measured exposure. Finally, there is an aperture correction k_{ap} which accounts for photons that make it through the tungsten aperture and k_{att} which accounts for the attenuation of the beam between the POM and the center of the collecting volume. There are different ways to calculate these correction factors which will be discussed in Chapter 3. For now, it is important to note that Eq. 2.3 needs to be altered to

$$X = \frac{Q}{lA_0\rho} k_{att} k_{ap} k_s k_e k_{sh}. \tag{2.4}$$

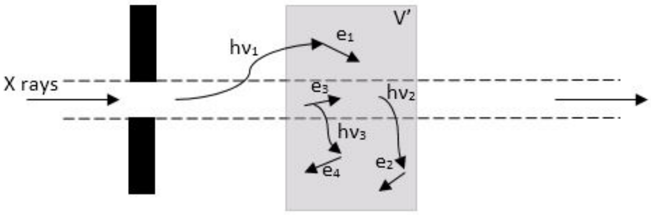

Figure 2.1: An example of how scattered and bremsstrahlung x-rays can contribute to the charge measurement in a free-air chamber causing an inaccurate exposure to be determined.

2.1.1.2 Attix-type variable-length chamber

Even with guard wires and plates, the electric field in this type of parallel-plate chamber is easily distorted if the plates are not perfectly parallel to each other and the beam axis or perfectly perpendicular to the boundaries of V'. The field can also be distorted if the collector and guard plates are not exactly coplanar, or if the collector plate is not kept at the same potential as the guard plates. Distortion makes defining the collecting volume, and therefore the mass, difficult. The error arising from the uncertainty in field uniformity is the largest source of error in these conventional chambers [21].

The variable-length type of free-air chamber was developed by Attix in 1961 to address the problems caused by the distortion of the electric field in parallel-plate chambers [21]. His design consists of two cylinders that can be pulled apart to extend the size of the chamber. The collecting rod is located a certain distance from the x-ray beam to ensure that no, or very few, electrons strike it causing a loss of ionization. The shell of the chamber is operated at a high potential and replaces the high-voltage plate.

Two measurements are taken with the Attix-type chamber: the first with the chamber in its collapsed position, and the second with the chamber extended so that the distance between the sides is increased by ΔL. For the first measurement, ionization in the entire chamber can be thought of as being made up of two parts: J_A is the ionization in volume A (the front half) and J_B is the ionization produced in volume B (the back half). Assuming that attenuation is linear, which is valid for the medium x-ray range that is being focused on [21], CPE exists throughout the chamber. Electrons escaping into the back wall of volume B will be replaced by electrons escaping from volume A and vice versa. Therefore, J_A and J_B will be almost equal and any correction for air attenuation is negligible with the linear attenuation assumption [21]. For the second measurement where the chamber is extended, there will be an increase in charge collected because of the larger volume. Instead of J_A and J_B, the ionization in the chamber is made up of $J_{A'}$ which has the same volume as J_A but moved closer to the x-ray source by $\Delta L/2$, $J_{B'}$ which has the same volume as J_B but moved farther from the x-ray source by $\Delta L/2$, and J_V which corresponds to the ionization produced in the volume V located in the center of the chamber and with a width of ΔL. $J_{A'}$ will be larger than J_A since the x-ray beam travels a shorter path to volume A' and therefore suffers less attenuation. The opposite is true for $J_{B'}$ and J_B. With the linear attenuation assumption $J_{A'}$ can be related to J_A by

$$J_{A'} = (1 + \frac{\mu \Delta L}{2}) J_A \tag{2.5}$$

and $J_{B'}$ can be related to J_B by

$$J_{B'} = (1 - \frac{\mu \Delta L}{2}) J_B, \tag{2.6}$$

where μ is the linear attenuation coefficient for air. These equations can be combined to create

$$J_{A'} + J_{B'} = J_A + J_B + \frac{\mu \Delta L}{2} J_A - \frac{\mu \Delta L}{2} J_B. \tag{2.7}$$

It can be deduced from Eq. 2.7 that $(J_{A'} + J_{B'}) = (J_A + J_B)$ if $J_A = J_B$. Even if the chamber is not built to be perfectly symmetrical or there is a slight CPE imbalance, it can almost always be assumed that $J_A = J_B$ if the chamber is built to keep these effects to a minimum. To illustrate this, consider the case where $J_B = 0.9J_A$ and $\mu\Delta L = 0.04$. From Eq. 2.5 we have

$$\begin{aligned} J_{A'} + J_{B'} &= J_A + J_B + J_A(0.02 - 0.9 \times 0.02) \\ &= 1.002J_A + J_B \\ &\approx 1.001(J_A + J_B). \end{aligned} \tag{2.8}$$

Even with a large difference of 10% between J_A and J_B, this case illustrates that there is only a 0.1% difference between $(J_{A'} + J_{B'})$ and $(J_A + J_B)$ [21]. As mentioned, carefully building the chamber can lead to the equality of $(J_{A'} + J_{B'})$ and $(J_A + J_B)$ being generally assumed. With these quantities being equal, the ionization created in the ends of the chamber cancel in the two measurements and the difference between the ionization measured in the two stages is just J_V, the ionization from the precisely known volume V. This volume takes the place of the collecting volume in the parallel-plate free-air chamber. The electric field uniformity, or lack thereof, does not affect the measurement as long as electron saturation does not change between the collapsed and extended chamber [21].

The exposure can be calculated in the same way that it was for the parallel-plate chamber: at the entrance of the aperture. Modifications are made to Eq. 2.4 to include the change in charge and length so that the exposure is calculated by

$$X = \frac{\Delta Q}{\Delta L}\frac{1}{\rho A_0}k_{att}k_{ap}k_sk_ek_{sh}, \tag{2.9}$$

where ΔQ is the incremental change in ionization charge for a known separation ΔL.

The main advantage of the Attix-type free-air chamber over the parallel-plate type is that there is less of a need for electric field uniformity so careful attention does not need to be paid to plate alignment or maintenance of the collector at ground potential. Similarly, the mass of the air can be defined more accurately by determining ΔL using a precision screw or gauge blocks.

2.1.2 Known-volume ionization chambers

Cavity ionization chambers are the most widely used type of dosimeter for precise measurements for higher energy x-rays [15]. A simplified diagram of a Farmer-type ionization chamber is shown in Figure 2.2. Cavity ionization chambers have a few advantages over free-air chambers. For this work, the primary advantages are that they are compact and, through the application of cavity theory, can measure air kerma from much higher energy photons. Cavity theory is described in the following section. The concept of ionization measurement is the same as a free-air chamber but on a smaller scale. The chamber consists of a gas-filled volume between an outer wall and a collecting electrode. The guard, located in the stem of the chamber, acts to define the collecting volume as it extends into the collecting volume. The high voltage, usually 300 V, is applied to the chamber wall with the collector connected to the electrometer input at or near ground potential. For minimal perturbation of the beam, ionization chambers often have “air-equivalent” wall materials which requires the effective atomic number to match that of air. Graphite is a material that has been historically used, but less fragile plastics have become more popular. The ionization chambers employed in this work are made of C552 air-equivalent plastic composed of polyvinylidene fluoride, carbon black, and silica. Carbon is incorporated into the plastic as it needs to be conductive. Cavity theories do not account for inhomogeneous wall media, so the collecting rod must be made of the same material.

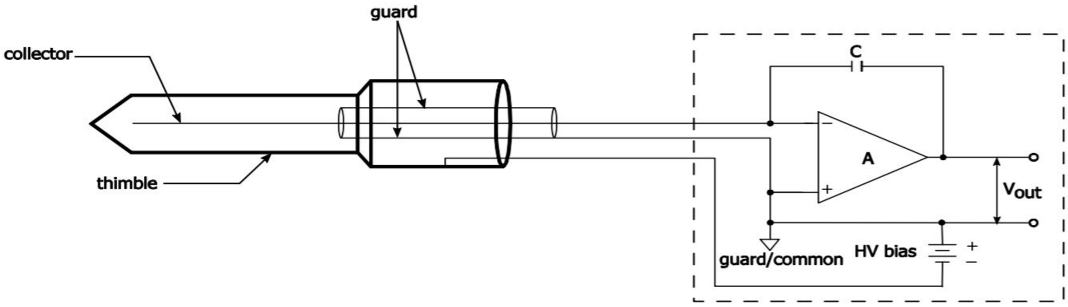

Figure 2.2: Schematic of thimble ionization chamber connected to an electrometer [1].

2.1.2.1 Cavity theory

A brief summary of Bragg-Gray cavity theory and restricted stopping powers is presented here, though a detailed description can be found in Attix [15]. If a fluence Φ of identical charged particles of kinetic energy T passes through an interface between two different media, g and w, the ratio of absorbed doses in the two media adjacent to their boundary can be written as

$$\frac{D_w}{D_g} = \frac{(dT/\rho dx)_{c,w}}{(dT/\rho dx)_{c,g}}, \tag{2.10}$$

where $(dT/\rho dx)_{c,w}$ and $(dT/\rho dx)_{c,g}$ are the mass collison stopping powers of the two media, evaluated at energy T. This equation can be applied to ionization chambers with walls as long as two Bragg-Gray conditions are met: (1) the thickness of the gas cavity is assumed to be so small in comparison with the range of the charged particles striking it that its presence does not perturb the charged particle field and (2) the absorbed dose in the cavity is assumed to be deposited entirely by the charged particles crossing it. For a differential energy distribution Φ_T the appropriate average mass collision stopping power in the cavity medium g is

$$_m\overline{S}_g = \frac{D_g}{\Phi} \tag{2.11}$$

and likewise for a thin layer of wall material w that may be inserted in place of g. Therefore, the ratio of absorbed dose in w to that in g is

$$\frac{D_w}{D_g} = \frac{_m\overline{S}_w}{_m\overline{S}_g} = {_m\overline{S}_g^w}. \tag{2.12}$$

The absorbed dose in the medium immediately surrounding the cavity can then be calculated by

$$D_w = \frac{Q}{m}\left(\frac{\overline{W}}{e}\right) {_m\overline{S}_g^w}. \tag{2.13}$$

Experiments in the 1950s found that δ-ray production had to be taken into account in cavity theory. Spencer-Attix restricted stopping powers are the stopping powers for electrons of energy T in medium w which includes only energy losses to δ-rays not exceeding Δ, which is the mean energy of electrons having projected ranges just large enough to cross the cavity. This is because electrons with $T < \Delta$ are assumed to have zero range and are assumed not to enter the cavity or transport energy. The dose in the medium immediately surrounding the cavity becomes

$$D_w = \frac{Q}{m}\left(\frac{\overline{W}}{e}\right)\left(\frac{\overline{L}}{\rho}\right)_g^w \tag{2.14}$$

where $\left(\frac{\overline{L}}{\rho}\right)_g^w$ is the ratio of Spencer-Attix restricted mass collision stopping powers.

2.1.2.2 Establishment of known-volume chambers

Known-volume ionization chambers are another method to measure dose absolutely. The mass of the air within the chamber can be determined using this known volume and the density of the gas in the chamber. Conventional known-volume chambers are specially made using graphite and high-precision machining techniques. NIST also independently verifies their known-volume chambers by filling the cavities with water and taking mass measurements with and without the water [23]. Given how complicated it is to fabricate and verify the volume of these chambers, they are currently limited to use at primary standards laboratories. This is why commercial ionization chambers used in the clinic or for research require calibration. The limitation on the accuracy of determining the volume depends on the chamber design. If any of the generated charge is collected on the grounded guard ring or is allowed to recombine in a locally weak pocket of the electric field, the effective volume will be smaller than the physical volume leading to an underestimation of the dose [15].

Another method of determining the volume of an ionization chamber has been developed with advancements in micro-computed tomography (μCT) imaging techniques [24]. With fine enough spatial resolution and a large enough chamber, it is possible to image ionization chambers and calculate their volumes through contouring. It is also imperative that the ionization chamber does not possess considerable metal that can lead to significant artifacts. As mentioned, the collection volume of the ionization chamber differs from its physical volume due to a portion of the electric field terminating in the guard instead of the collecting electrode. The electric field can be modeled in COMSOL Multiphysics to quantify this discrepancy [25]. The volume of the electric field that terminates in the guard can then be subtracted from the physical volume.

Air kerma is established at a point in the beam with a known volume ionization chamber with the following equation,

$$K_{air} = \frac{Q}{m(1-g)} \left(\frac{\overline{W}}{e}\right) \left(\frac{\overline{L}}{\rho}\right)^{wall}_{air} \left(\frac{\overline{\mu_{en}}}{\rho}\right)^{air}_{wall} K_h K_{wall} K_{an} K_{comp} K, \tag{2.15}$$

where $(\overline{L}/\rho)^{wall}_{air}$ is the ratio of Spencer-Attix collision mass stopping powers for the wall material to dry air, $(\overline{\mu_{en}}/\rho)^{air}_{wall}$ is the ratio of mass energy absorption coefficients averaged over the energy spectrum for dry air to the wall material, K_h is the humidity correction factor, K_{wall} corrects for attenuation and scatter in the chamber wall, K_{an} corrects for the axial nonuniformity due to the point source nature of the beam, K_{comp} corrects for any nonuniform nature of the wall material and K accounts for any other corrections needed [26]. The calculation of these correction factors is outlined in Chapter 4.

2.2 X-ray irradiator use in radiobiology studies

2.2.1 The importance of dosimetry in radiobiology studies

Cancer research requires the use of cell and animal models to understand the effects of ionizing radiation exposure and biological mechanisms of response and cancer progression in humans through preclinical radiobiology studies [27–30]. In human radiotherapy treatments, dosimetric accuracy within 5% is required for acceptable levels of tumor control probability and normal tissue complication probability for favorable outcomes [31], but the dose uncertainties in radiobiology studies tend to be on the order of ±10% [32]. It has been noted that in some cases, a variance in dose of 10% can lead to a 5-90% change in biological response due to the steepness in radiation biological response curves [33]. Though these uncertainties depend on the desired endpoint and the biological variation, it is important to provide accurate dose estimates in order to obtain meaningful and translatable results. This is especially true as more complex preclinical treatment techniques become commonplace. Ghita et al. estimated that a reduction in dose uncertainty from 10% to 5% would decrease the required number of animals from 23 to 10 in a discussion of the SARRP irradiator [34]. There has recently been increased concern over the difficulty of reproducibility in clinical trials [6] and one method of addressing the problem is focusing on accurate dose measurements and standardization in radiobiology [35, 36].

There are a large number of available dosimeters, experimental setups, and codes of practice to establish a reference dose rate for low and medium-energy x-rays [8, 37, 38]. There has also been a documented lack of consistency across institutions. A multi-institutional study by Pedersen et al. found that of the 5 surveyed sites using x-ray irradiators, only 1 delivered a dose that was within 10% of the intended dose [39]. Similar comparisons by Trompier et al. and Seed et al. found that 2/4 and 3/7 sites surveyed that used x-ray irradiators failed to deliver the intended dose within 5% [40, 41]. These studies lead to the conclusion that manufacturer-supplied dose rates or standard orthovoltage x-ray methods may not be appropriate for these irradiators and warrant investigation. These multi-institutional studies have focused on large-field irradiators without treatment planning systems. Treatment planning systems and onboard imaging can allow for overcoming the difficulty of estimating the dose in non-reference conditions, but treatment planning may be limited to calculating a beam-on time using tabulated output factors [42], and the reproducibility across instructions or irradiator types has not been investigated.

Dose determination for the low- and medium-energy x-ray range for the operation of radiobiology irradiators require measurements of air kerma that are traceable to a primary standards lab, such as NIST in the United States. This measured value of air kerma can then be used to determine absorbed dose to water for these preclinical studies. A FAC is the reference instrument for primary measurement of air kerma for x-ray beams

[43, 44]. An air kerma calibration for a user's equipment is determined at a primary standards laboratory or secondary standards dosimetry laboratory, such as an accredited dosimetry calibration laboratory (ADCL). These air kerma calibrations are done in a series of standard x-ray beams that have a standard tube potential, first and second half-value layer (HVL), and homogeneity coefficient (HC). Although HVL is not enough to specify a beam on its own, it is commonly used as a surrogate of the x-ray energy spectra. It is possible for two different beams with different maximum tube potential and spectra to have the same HVL. Studies show that simulated spectra with different tube potential and filtration but the same HVL can lead to an uncertainty in the calculated dose to water as large as 10% [45]. The American Association of Physicists in Medicine (AAPM) Task Group 61 (TG-61) has written a recommended protocol for determining dose to water in the energy range in which radiobiology x-ray irradiators operate [8]. To apply TG-61 to radiobiology beams, a number of assumptions are made. One such assumption is that the spectra in which dosimetry equipment is calibrated sufficiently matches the spectra of the radiobiology irradiators, even though these irradiators often operate at higher tube potentials and/or lighter filtration than available standard beams. This leads to higher uncertainty in the dose determination from these irradiators [46]. Therefore, it is desired to develop standard x-ray beams with spectra that more closely match the spectra of some common cabinet and conformal radiobiology irradiators. This work aims to establish those standard x-ray beams that can be used for calibration of the XRad320 and the SARRP, two common animal radiotherapy irradiators.

2.2.2 Cabinet irradiators

The x-ray tubes and generators used in radiobiology studies are modified from orthovoltage clinical units. The orthovoltage systems for human treatments use a movable x-ray tube with filters and cones that define the beam quality and collimation. Typically there is no use of pre-treatment imaging or treatment planning. Instead, the dose at the prescription point, typically at the surface or 2 cm depth, is calculated using defined dosimetry protocols, such as the TG-61 report. These orthovoltage x-ray irradiators were adapted for small animal radiation research because the photon energy range provides an ideal penetration depth and requires only limited shielding and maintenance [47]. Dedicated radiobiology x-ray irradiators are shielded units ("cabinet irradiators") with an x-ray tube mounted to the unit ceiling and a stainless steel tray to move the specimen to different distances from the source. The units typically have a maximum source-to-surface distance (SSD) of approximately 80 cm. Maximum voltage settings for typical radiobiology studies may range from 160 to 360 kVp [48]. Filters are typically sold as accessories with the unit. Nominal dose rates from these machines are 1-3 Gy/min at 50 cm from the source, but these values depend highly on the SSD, field size, beam filtration choice, and generator type. Figure 2.3 shows a photo of the XRad 320 by Precision X-Ray (PXi) (Branford, CT), previously located in the Small Animal Imaging Research Facility (SAIRF) at the University of Wisconsin. The XRad 320 has a maximum voltage of 320 kV, but may be operated at lower tube potentials [49]. This model uniquely has adjustable lead collimators that allow for field sizes between 2 x 2 cm^2 and 20 x 20 cm^2 at 50 cm SSD. The maximum stated dose rate is $>$ 3 Gy/min at 320 kVp and 12.5 mA without any beam hardening filtration. The irradiator is typically used with two commercial filters. F1 will refer to the more lightly filtered beam which is comprised of 2 mm Al added filtration. F2 will refer to the more heavily filtered beam which is comprised of 1.5 mm Al+0.25 mm Cu+0.75 mm Sn. Both of these beams operate with the maximum 320 kVp tube potential and 12.5 mA tube current. The XRad320 utilizes a Comet MXR-321 x-ray tube (Comet AG, Liebefeld-Berne, Switzerland) and a Gulmay 320 (Suwanee, GA) constant potential generator. The tube has a typical tungsten anode with a target angle of 30 degrees. It also has an inherent filtration of 1 mm Be along with a 2 mm Be exit window. The XRad 320 is used for whole-body irradiation of mice, as well as cell studies.

Single-field approaches have been used for studies of retinoblastoma [50] and fractionation in lung cancer [51], among many others. It is still a common technique, for example, to irradiate bone marrow before hematological studies [52]. X-ray irradiators are also used for high-throughput irradiation of cells in petri dishes [53] or blood vials [54]. Field sizes vary based on the irradiation setup. Collimating a beam may introduce scatter into the field and affects the electron backscatter in the specimen [55]. When a specific tumor site is required for small animal irradiations in these cabinet irradiators, custom restraining jigs and beam shaping collimators are made. For example, plastic cones with holes only for the protruding snout are used for experiments on oral mucositis [56] or a heterotopic tumor can be made to protrude through a plastic restraining tube [57]. Beam shaping may be accomplished with lead blocks with apertures around the target or the field size is collimated to as small as possible [58, 59]. These units are typically operated by users without physics support, and instead rely on manufacturer-supplied calibrations or lookup tables. Experiments can have widely varying methods of setup requiring complex calibration and dosimetry support. This has led to a documented lack of reproducibility in small animal studies [39]. It has been suggested that a large contributing factor in this is the lack of standardized dose delivery in small animals. In response to both the limitations of non-conformal delivery and limited dosimetric information, conformal small animal irradiators with treatment planning systems were invented for commercial use.

2.2.3 Conformal irradiators

As mentioned, the single-field, whole-body irradiation techniques commonly used in preclinical research presented a challenge in the translation of results from mice to humans [60]. In response, several commercial small irradiators have become commercially available in the past 10 years, including modification of a μCT scanner at Stanford University [61] and an Ir-192 hemi-brain system at Washington University [62]. Systems developed

Figure 2.3: XRad320 cabinet irradiator.

at Princess Margaret Hospital (PXi SmART) and Johns Hopkins University (XStrahl SARRP) have been the most successful commercially to date. The SMART and SARRP units integrate multi-modality imaging, radiation treatment planning, and conformal delivery techniques with brass stereotactic cone attachments [63, 64], which results in field sizes as small as 0.5 mm. The small animal radiation research platform (SARRP) by XStrahl (XStrahl Ltd., Camberley, UK) is capable of delivering multi-directional, kilovoltage radiation fields to targets in rodents using CBCT image guidance with sub-millimeter precision. Small animal conformal irradiators are shielded in a cabinet, as with the large-field irradiators described before. They consist of an x-ray tube mounted on a rotating gantry and a carbon fiber treatment couch capable of xyz translation, roll, and pitch. The tubes are typically used for imaging as well as treatment by adjusting the kVp and mA settings and using a mounted flat-panel imager. Varying field sizes are achieved by replacing the brass collimating nozzle. Figure 2.4 shows the SARRP unit at the University of Wisconsin with the 10 mm stereotactic cone in place. The SARRP utilizes a Varex NDI-225-22 x-ray tube attached to a gantry that can be rotated between -180 and 180 degrees. The maximum tube potential can be adjusted in 1 kV increments between 30 and 225 kVp. The x-ray tube has a 20 degree tungsten target and an inherent filtration of 0.8 mm Be.

There is a standard therapeutic beam for the SARRP that has a maximum tube potential of 220 kVp and a 13 mA tube current with 0.15 mm Cu filtration.

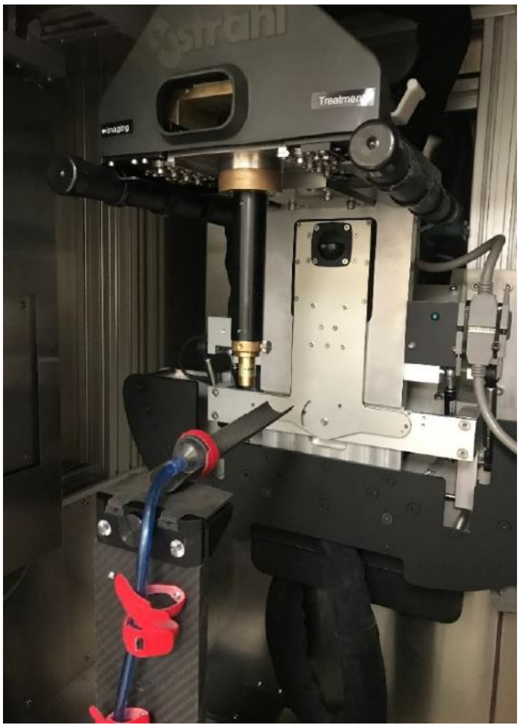

Figure 2.4: The SARRP unit at the University of Wisconsin.

2.3 Quality of x-ray beams

2.3.1 Beam quality definition

There are two mechanisms by which x-rays are produced: bremsstrahlung and fluorescence [15]. Electrons are accelerated into a target, typically tungsten for the medium-energy range and above, causing either of these interactions. Bremsstrahlung x-ray photons are emitted by radiative interactions with the Coulomb force field of atomic nuclei as the electron decelerates. Since an electron may have one or more bremsstrahlung interactions in the material and interaction may result in partial or complete loss of electron energy, the resulting bremsstrahlung photon may have any energy up to the initial energy of the electron. Fluorescence x-rays, also called characteristic x-rays, are emitted when hard collisons occur between charged particles and inner-shell electrons and energy is released to fill the inner-shell vacancy. Characteristic x-rays have discrete energies dependent on the material of the target as their energy is equal to the difference in the binding energy of the inner-shell and outer-shell electrons. For tungsten, the discrete energies of importance for the energy range investigated in this work lie between 58 and 69 keV [3]. The resultant x-ray spectra can be categorized by the range of energies present, where a "hard" beam has more penetrating power with a higher average energy, while a "soft" beam has lower average energy and is less penetrating. The initial output spectrum can be altered by placing various filtration material in the path of the beam. The principal result of adding filters to an x-ray beam is to remove photons preferentially at energies where the attenuation coefficient is largest. The photoelectric effect dominates at energies below approximately 300 keV so preferential attenuation of lower energy photons occurs which causes beam hardening. At energies higher than 300 keV, the Compton effect starts to dominate which mainly removes the photons below a few hundred keV without greatly modifying the spectral shape. This does not become impactful until reaching the MV energy range so it is not a concern for the energy range of this work.

Ideally, the energy fluence distribution would be used to describe each beam, but spectral distributions are difficult to measure. In most situations the beam quality is specified by its attenuation characteristics in a reference medium. This includes the peak voltage (kVp), the first and second HVL, and HC. The HVL is the thickness of a medium of specified composition required to attenuate the intensity of the beam to half its original value [3]. The second HVL is the additional thickness needed to reduce the intensity by half again, and the HC is the ratio of the first and second HVL. The HC approaches unity as the spectrum is narrowed by filtration to approach a monoenergetic beam. Aluminum is the typical reference medium for energies less than 120 keV and copper is the typical reference medium for energies between 120 and 500 keV. This work will primarily use copper as the reference medium. To determine the first and second HVL, an attenuation curve is typically measured with an ionization chamber. Essentially, the air kerma is measured with increasing thickness of the attenuating medium. The first HVL can then be easily determined by noting at which thickness the air kerma drops to half its original value. The second HVL can be determined by noting the quarter-value layer (QVL) and subtracting the first HVL thickness from this value. When measuring the HVL, a narrow-beam geometry is required, i.e. scattered x-rays from the attenuator must not reach the detector.

2.3.2 Filtration composition

The characteristic x-rays produced by tungsten cause significant peaks in the energy spectrum, known as K lines, as shown in Figure 2.5, that can lead to a low average energy despite a high maximum energy. These K lines can be preferentially filtered out by tin filters. Tin has a K absorption edge at 29.2 keV which will strongly absorb x-rays between 30 and 70 keV by the photoelectric effect [3]. The K-edge refers to a sharp and significant increase in the mass energy attenuation coefficient which causes the material to act as a bandpass filter. The x-rays in the specified energy range have a much higher probability of being absorbed than at energies outside of that range.

Tin does little to absorb x-rays below 29 keV and also produces its own characteristic x-rays. To preferentially reduce x-rays below 29 keV, a copper filter can be added as its K-edge is at 9 keV. Finally, an aluminum filter can be added to absorb the very low

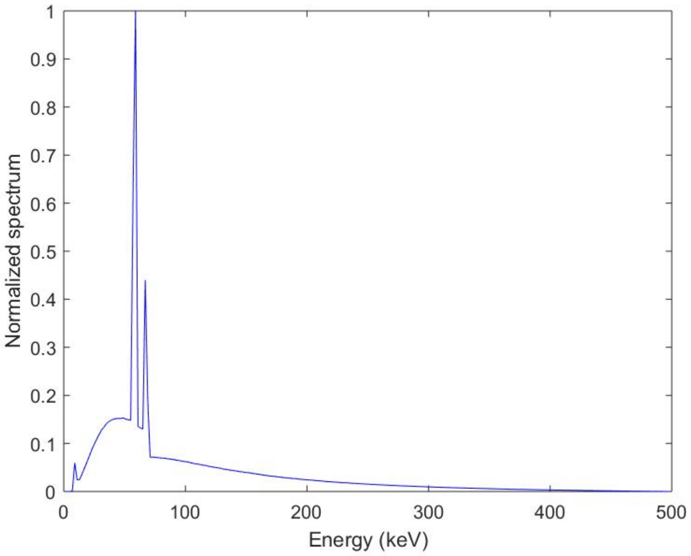

Figure 2.5: Example of an unfiltered x-ray spectrum with the tungsten x-ray lines produced by the tungsten target.

energy characteristic x-rays produced by copper. These combination filters of tin, copper and aluminum are called Thoraeus filters [65]. There are three standard Thoraeus filters used with orthovoltage x-rays which are not thick enough for the energy ranges used in this project. To increase the average energy even further, a more dense filter is needed. It is possible to use tantalum or tungsten for this purpose, but due to their characteristic x-rays, the filters must be backed by the tin, copper and aluminum filters as well. Lead is another common filter material and is used for NIST's highly filtered H-series x-ray beams, also requiring tin, copper and aluminum combination filters.

2.3.3 Moderately filtered x-ray beams at the UWADCL

This work will often mention the M-series x-ray beams, which are a series of moderately filtered x-ray beams maintained at the UWADCL. They are a set of beams that have been matched to standard beams at NIST and are used for calibrations of ionization chambers in terms of air kerma for both therapy and diagnostic x-ray applications. They match the NIST beams in tube potential, first HVL, second HVL, and HC. For beams with tube potentials higher than 50 kVp, the air kerma rate was established using an Exradin A3 spherical ionization chamber (Standard Imaging, Middleton, WI) that has been calibrated at NIST. Table 2.1 outlines properties of the M-series beams of interest to this work.

Table 2.1: UWADCL M-series beam properties.

Beam code	Tube potential (kVp)	Tube current (mA)	Added filtration (mm Al or Cu)	HVL (mm Al)	HC	Air-kerma rate (mGy/s)
UW50-M	50	25	1.08 Al	1.04	66	2.020
UW60-M	60	25	1.50 Al	1.65	67	1.796
UW80-M	80	25	2.75 Al	3.00	68	1.821
UW100-M	100	25	4.77 Al	4.98	72	1.822
UW120-M	120	25	3.0 Al + 0.10 Cu	6.77	75	2.365
UW150-M	150	20	2.83 Al + 0.28 Cu	10.1	87	2.173
UW200-M	200	15	1.00 Al + 1.01 Cu	14.8	95	1.930
UW250-M	250	12	1.96 Al + 2.36 Cu	18.3	98	1.633

2.4 Summary and project scope

This chapter gave an overview of absolute dosimetry, and the current state of a few x-ray standards in the medium and higher energy x-ray range. This work aims to improve the x-ray standard for radiobiology irradiators and Ir-192 brachytherapy sources. It also aims to develop an air kerma standard for high energy x-ray beams that is currently unavailable. These improvements and establishments will be achieved through the use of a free-air chamber and known-volume ionization chambers that were developed for this project.

Chapter 3

Free-air chamber development

3.1 Mechanical design

3.1.1 Size determination

When Attix originally proposed his new chamber design, he included comments on how large a free air chamber would need to be to account for medium energies. He said specifically "for a chamber covering the x-ray voltage range of 50-250 kV, a diameter of 30 cm would be appropriate, reducing the losses due to electrons terminating in the walls to a few tenths of a percent in the worst cases [21]". He included in a footnote that the estimate is based upon experiments done to determine the optimal plate separation for parallel plate free air chambers [66]. For the study, Attix and DeLaVergne acquired three measurements for various x-ray beams: (1) determine the ionization produced in parallel layers of air at various perpendicular distances from a narrowly collimated x-ray beam (which they call the grid chamber), (2) repeat (1) and include an "electron filter" interposed between the x-ray beam and ion-collecting region to absorb all the electrons originating in the beam but allow scattered x-rays to pass through with little attenuation, and (3) measure the ionization produced in a conventional free-air chamber by the same x-ray beam. Then the percent ionization lost by inadequate separation of the parallel plates was determined by the following equation:

$$\%\ \text{electron loss} = \frac{(100)(1.087)(2)\sum_{d}^{\infty}(I_{efo} - I_{eft})}{I_{sc}} \tag{3.1}$$

where I_{efo} is the grid-chamber ionization current with the electron filter out, I_{eft} is the grid chamber ionization current with the electron filter in place, I_{sc} is the corresponding ionization current in the standard free air chamber, and d is the variable distance from the collector plate to the x-ray beam in the grid chamber [66]. The factor of 2 was included because the grid chamber measured the ionization only on one side of the x-ray beam. The 1.087 was a correction factor that accounted for the area covered by nylon threads which absorbed electrons. Attix and DeLaVergne showed that once the collecting volume reaches 12 cm radius (or 24 cm diameter), electron losses reduce to within a percent for x-ray energies up to 250 kV [66]. The authors thought it would be desirable to convert the data for parallel plate chambers to a more general form that could be applied to any free-air chamber in which the cross-sectional shape of the collecting volume was known. From these results, a 30 cm diameter was chosen for the medium-energy free-air chamber for photon energies up to 300 keV. This was verified by calculations and a Monte Carlo simulation. The maximum energy of an electron produced by a 300 keV photon will be approximately 300 keV. The CSDA range of a 300 keV electron in air is 77.78 cm [67]. Although this is about 2.5x the proposed diameter, the interactions that produce 300 keV electrons will be very rare. For energies between 50 and 300 keV interacting in air, Compton scattering events dominate. The maximum energy that can be transferred to an electron in a single Compton interaction is given by the following equation [68]:

$$E_{e^-}|_{\theta=\pi} = h\nu\left(\frac{2h\nu/m_ec^2}{1+2h\nu/m_ec^2}\right), \tag{3.2}$$

where $h\nu$ is the energy of the photon and m_ec^2 is the rest mass energy of an electron. Therefore, the maximum energy transferred to an electron from a 300 keV photon in a Compton scattering event is

$$E_{e^-}|_{\theta=\pi} = 300\,\text{keV}\left(\frac{2\times 300\,\text{keV}/511\,\text{keV}}{1+2\times 300\,\text{keV}/511\,\text{keV}}\right) = 162\,\text{keV}. \tag{3.3}$$

The CSDA range of a 162 keV electron in air is 29.63 cm which is roughly the same as the proposed diameter of the collecting volume [67]. Since the probability of an interaction causing an electron to have a higher energy than 162 keV is very low, the effective range of the electrons will be about 30 cm. Combine this with the fact that the x-ray spectra have very few photons at these high energies to begin with, a 30 cm diameter collecting volume should be sufficient to collect the majority of electrons.

Finally, the Monte Carlo code Monte Carlo N-Particle transport code 6 (MCNP6) was used to confirm the experiments by Attix and the above calculations. An x-ray disk source was created to mimic an x-ray beam past the FAC's beam-defining aperture which was pointed at a cylindrical volume of air as shown in Figure 3.1. The length of the air volume was constant (30 cm) and the radius varied between 1 and 20 cm. A *F8 tally was used to determine the electron energy deposition within the volume for different photon energies. Those results are shown in Figure 3.2. The figure shows a positive slope at small radii for all energies indicating that some electrons are escaping the cylinder before depositing all of their energy. Each line corresponding to a different energy plateaus once the radius of the volume is large enough to collect all of the electron energy. The radius at which this happens is different for the different energies because the electrons have different ranges. Of importance is that by 12 cm radius, or 24 cm diameter, each line has leveled off regardless of photon energy which confirms Attix and DeLaVergne's measurements. This is shown more clearly by the slopes of the lines plotted in Figures 3.3 and 3.4. This concludes that a 30 cm diameter collecting volume should be sufficient in collecting all of the electrons produced by photons with energies up to 300 keV. In the actual design of the free air chamber the walls will contribute to scatter and electron loss, but those detriments will be accounted for with minimal correction factors.

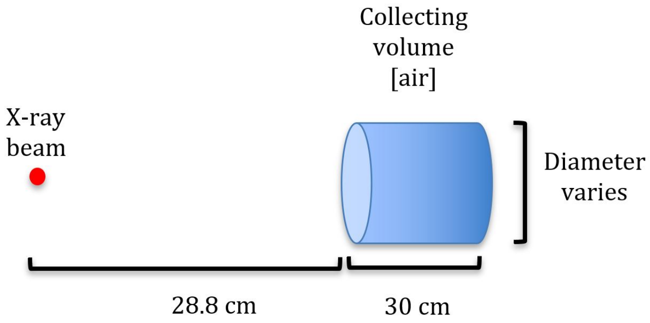

Figure 3.1: The geometry for the size test MCNP6 simulations. The disk source represents the x-ray beam after passing through the aperture and the distance between the source and the collecting volume is the distance between the aperture and collecting volume in the full design.

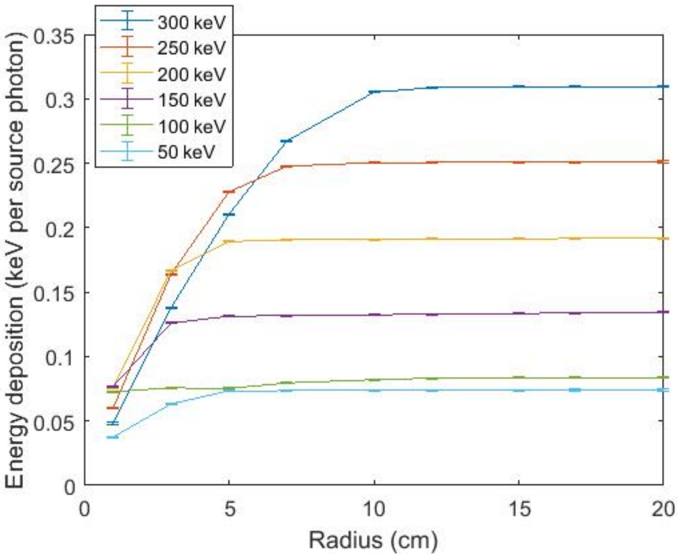

Figure 3.2: Electron energy deposition for various size volumes of air for electrons produced from different energy photons.

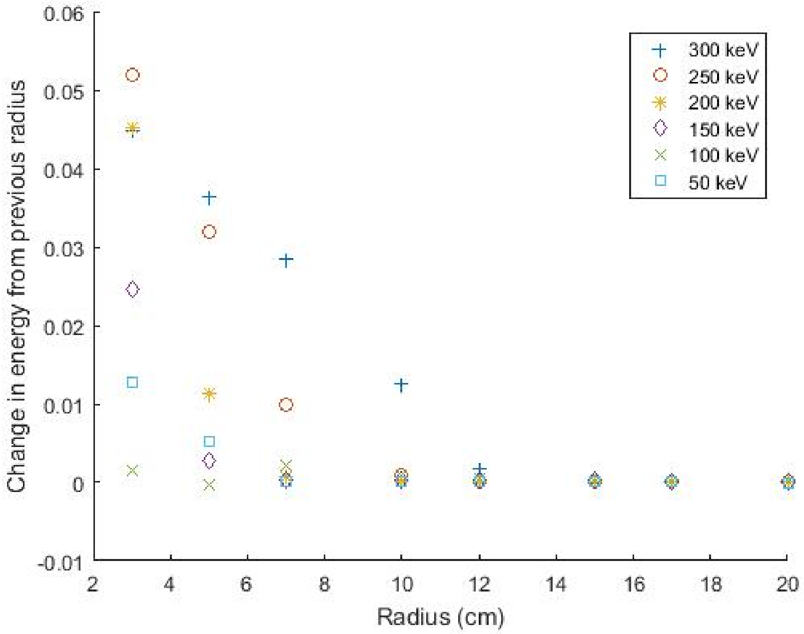

Figure 3.3: Slopes of the lines in Figure 3.2 indicating that the slopes plateau at radii larger than 15 cm.

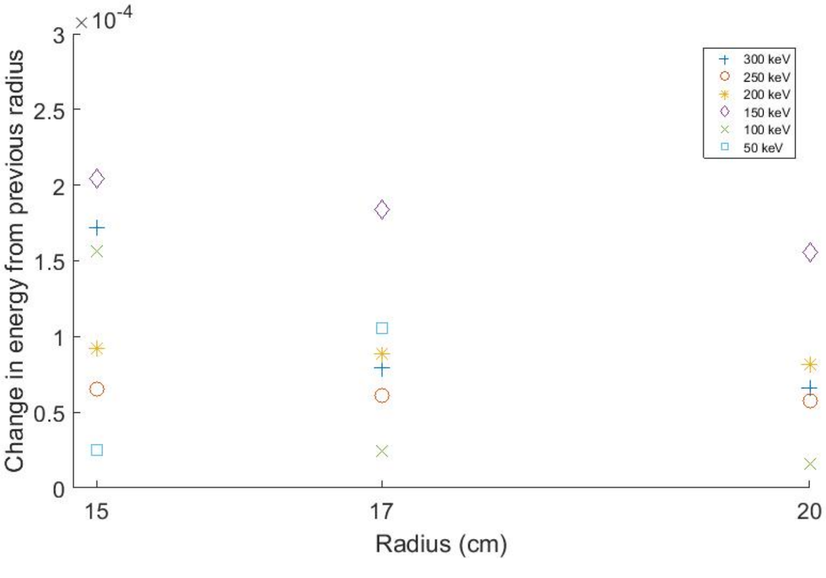

Figure 3.4: The higher radius portion of Figure 3.3 zoomed in.

3.1.2 Aperture flare and graphite window

Certain FAC designs include a 45° flare in the aperture to reduce sensitivity to imperfect alignment. With the advent of lasers for alignment, it is possible to align chambers within a millimeter of precision, so there is not as much need for this feature. There are significant disadvantages to the flare as well, including it being more difficult to manufacture and verify the diameter. Figure 3.5 shows there is no significant difference in the aperture correction with and without the flare. Therefore, no aperture flare was included in this FAC design.

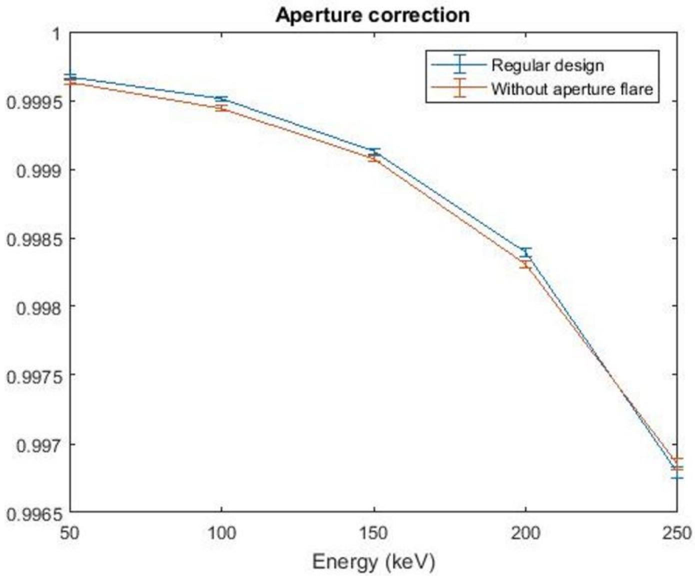

Figure 3.5: The aperture correction factor as a function of energy with and without an aperture flare.

Another FAC design possibility is the inclusion of graphite windows. The purpose of the graphite window is to provide a source for electrons to aid in achieving CPE. There are some concerns with including a graphite window: the graphite thickness would need to be 0.017 cm making it very fragile, an extra attenuation correction would be needed, and, most notably, the inclusion of a graphite window makes the chamber not technically a free-air chamber as it is no longer free-in-air. The scatter and electron loss correction factors were compared with and without the graphite window to investigate if this FAC could do without. Figure 3.6 and 3.7 show how these correction factors are affected by the removal of the graphite window. Since both correction factors were affected, the percent difference by removing the window as a function of energy was plotted as shown in Figure 3.8. The average scatter improvement was 0.27% and the average electron loss detriment was 0.05%. The improvement in the scatter correction is larger than the detriment to the electron loss so this, combined with the disadvantages listed, leads to the conclusion that the graphite window is not necessary. The minimal added loss of electrons will simply be corrected for with the electron loss correction factors.

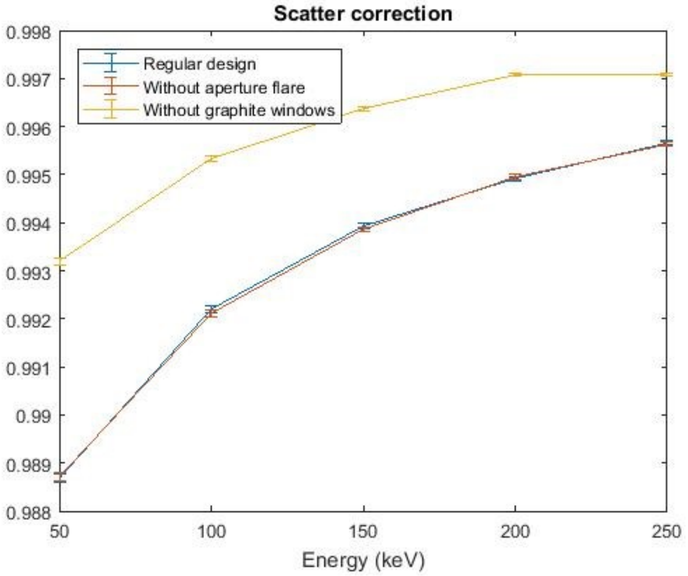

Figure 3.6: The scatter correction factor as a function of energy with and without a graphite window. Since unity would indicate no scatter, removing the graphite window improves the scatter correction.

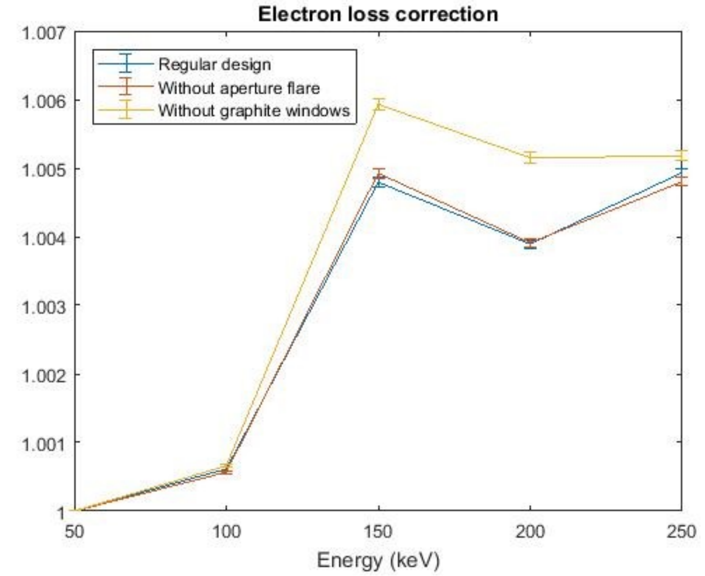

Figure 3.7: The electron loss correction factor as a function of energy with and without a graphite window. Since unity would indicate no electron loss, removing the graphite window worsens the electron loss correction.

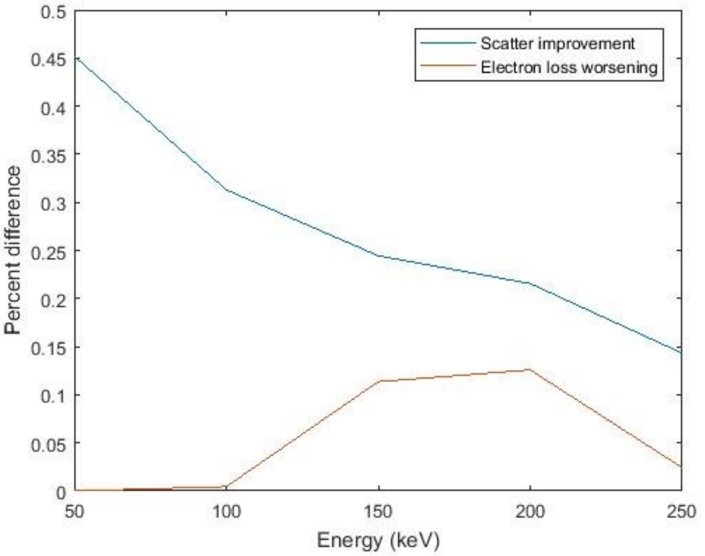

Figure 3.8: The percent difference in the scatter and electron loss correction factors when the graphite window is removed. Removing the graphite window improves the scatter correction but worsens the electron loss correction.

3.1.3 Aperture diameters

Two apertures with different diameters were desired to aid in validation of the FAC by providing multiple data points with different collecting volumes. One of the diameters was chosen to be 1 cm to be consistent with other FAC's of this size, but a smaller diameter aperture was desired. With a smaller diameter, it's possible that the signal would be too low for a decent signal-to-noise ratio (SNR) so the signal with aperture sizes of 1 cm, 0.5 cm, and 0.25 cm diameter were investigated. Air kerma rates, $\dot{K}$, for each relevant beam code from the UW M-series beams was converted to current, A, by

$$A = \dot{K} \cdot m \cdot \frac{1}{\overline{W}/e}, \tag{3.4}$$

where the mass, m, is calculated by

$$m = \pi r^2 h \rho, \tag{3.5}$$

where r is the radius of the aperture, h is equal to the length of the FAC collecting volume when it is collapsed and its signal will be lowest, and ρ is the density of air at STP. Figure 3.9 shows the results. The threshold with the use of a SuperMAX electrometer is 2 pA so there is no signal concern with any of the aperture sizes. A 0.5 diameter aperture was chosen as the second aperture.

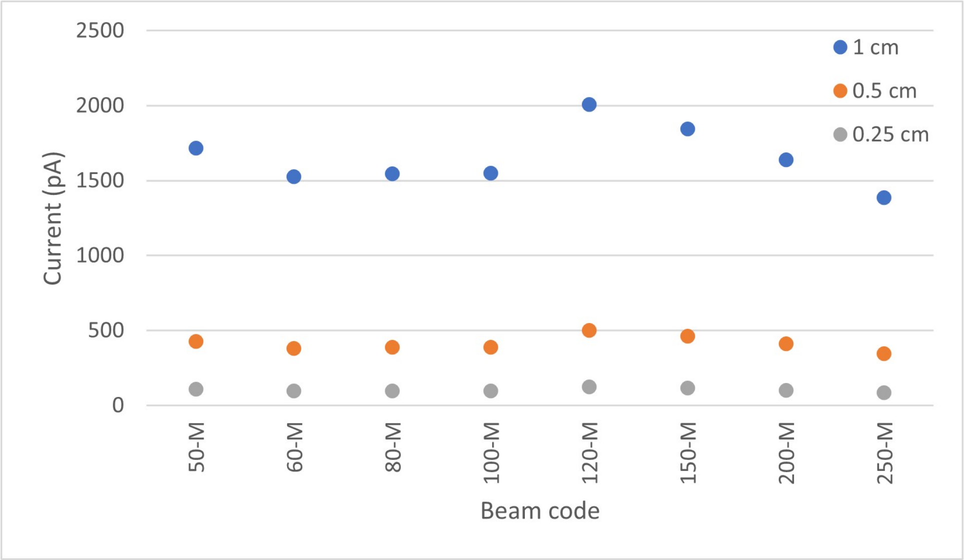

Figure 3.9: The signal of each beam code with the various aperture diameter options.

3.1.4 Shielding calculation

To prevent in-scattering of x-rays from room scatter, lead shielding is required to envelop the FAC. The concrete x-ray vault where the FAC will be used was modeled in MCNP6 based on room dimensions from building plans. The FAC shielding was also modeled inside the room at it's approximate location for measurements. A disk source of parallel photons was placed at the location of the x-ray tube exit window in the vault to approximate an x-ray beam of 320 keV photons. No aperture was included on this model so that any x-rays entering the shielding will be from scattered x-rays and not the primary x-ray beam. An F4 tally was used to calculate the flux of photons inside the shielding with various iterations of lead. The optimization of the lead shielding had two goals: to reduce the flux of scattered x-rays inside the shielding and to keep the weight of the shielding at a manageable level. The front shield requires significantly more lead than the other sides as the primary x-ray beam impinges directly onto this front face. The HVL of a material at a specific energy is given by

$$HVL = \frac{\ln 2}{\mu} \tag{3.6}$$

where μ is the attenuation coefficient of the material at that energy [3]. With the μ value from NIST's ESTAR database, the HVL of a 320 keV photon is 1.7 mm Pb [67]. The rule of thumb for sufficient shielding for primary barriers is 10 HVL's which is equivalent to 17 mm of lead. This was verified with the F4 tally directly behind the front face of lead as shown in Figure 3.10.

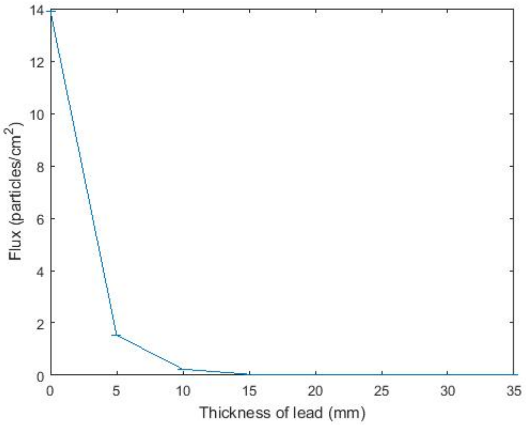

Figure 3.10: Flux of scattered x-rays that pass through the front face of the shielding box. The flux levels off by 15 mm of lead.

The amount of lead in the top/sides/back/bottom of the shielding was increased until the x-ray flux inside of the shielding reached a minimum. This occurred when the lead was 2 mm thick as shown in Figure 3.11. It was also found that the bottom shield of lead was not necessary and the aluminum plate that supports the FAC provides sufficient shielding. Removing that lead allows for a reduction in the weight of the shielding.

The shield plates were manufactured by Hopewell Designs. After consultation, the final shielding configuration was 20 mm of lead for the front face and 2 mm of lead for the other faces. The lead pieces were sandwiched between 2 mm aluminum plates for structural support and then painted for lead safety. Figure 3.12 shows the completed shielding.

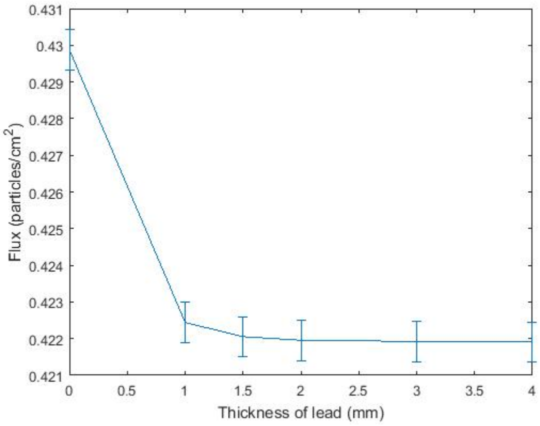

Figure 3.11: Flux of scattered x-rays that pass through the shielding box at various thicknesses.

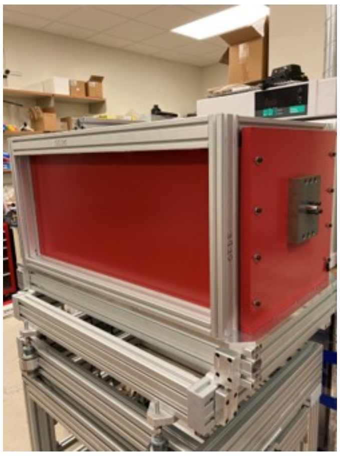

Figure 3.12: Assembled shielding for the FAC standing on the FAC cart.

3.1.5 FAC design

A variable-length FAC based on designs by Attix [22] and the National Radiation Standard Laboratory in Taiwan [20] was created using SolidWorks, a solid modeling computer-aided design and computer-aided engineering computer program published by Dassault Système (Waltham, MA). The FAC is composed of a stationary aluminum cylinder and two outer telescoping aluminum cylinders that are each attached to a stepper motor-controlled linear stage with precision lead screws for known cylinder separation distances.

The cylinders have “top hat” plates that are connected to the linear stages via trusses. The cylinders are all 30 cm in diameter and the three together are 30 cm in length when collapsed and double in length to 60 cm when fully extended. The stepper motors were programmed to move in 35 mm increments to acquire four measurements for each measurement set. This allows for the generation of a charge vs. cylinder separation graph with four data points rather than just two. In place of the change in charge over the change in length noted in Equation 2.9, the slope of this graph is used. An aluminum collecting rod is located halfway between the bottom of the FAC and the defined x-ray beam. The cylinders are biased and the collector kept at zero potential to establish an electric field for ions created by the x-ray beam to travel along to the collector. This is outlined further in the electric field simulation section. Electrically critical parts were cleaned to remove oil and other particles that could result in poor insulation or pockets of unreliable electric field. Polycarbonate guards surround the collector at both ends to separate it from the high voltage plates. A guard tube made of aluminum and polycarbonate is located at the back of the FAC to protect the collector when the cylinders are moving and to maintain the edge of the electric field at the back plate. A smaller aluminum guard is located at the front of the FAC to maintain the edge of the electric field at the front plate. Thick polycarbonate washers separate the trusses and the high-voltage plates to isolate the biased FAC from the linear stages. Two limit switches, a mechanical one and an electrical one, were placed so that if the shielding is lifted off of the FAC, the high voltage will switch off for safety. Two tungsten beam-defining apertures of known area were fabricated to be 20 mm thick and machined to nominal diameters of 5 and 10 mm. These apertures were measured with precision pin gauges and the diameters were 5.004 and 10.01 mm, respectively. Figure 3.13 shows the schematic of the FAC in a partially extended position. Figure 3.14 shows the FAC once it was fully assembled before the shielding was added. Figures 3.15 through 3.17 show stages of assembly of the FAC that are of interest.

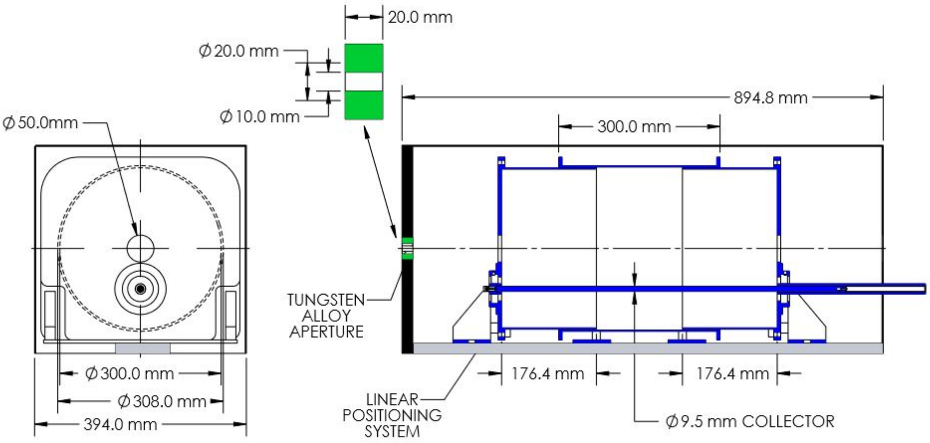

Figure 3.13: Schematic of the front and lateral view of the FAC when it is partially extended. The colors denote materials: green is tungsten alloy, black is lead and blue is aluminum.

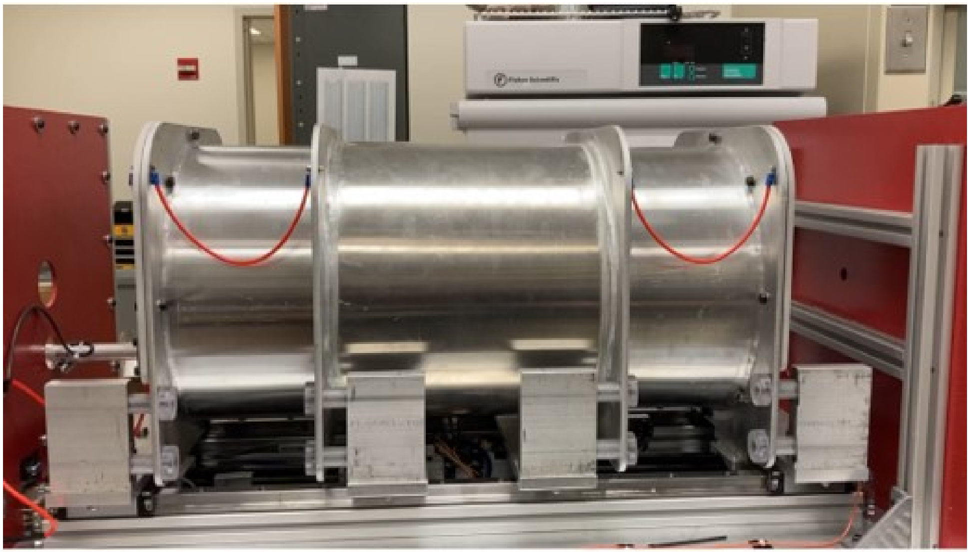

Figure 3.14: The FAC fully assembled in its extended position. The orange wires electrically connect all three cylinders. Note the thick plastic washers and screw sheaths that electrically separate the trusses from the biased plates.

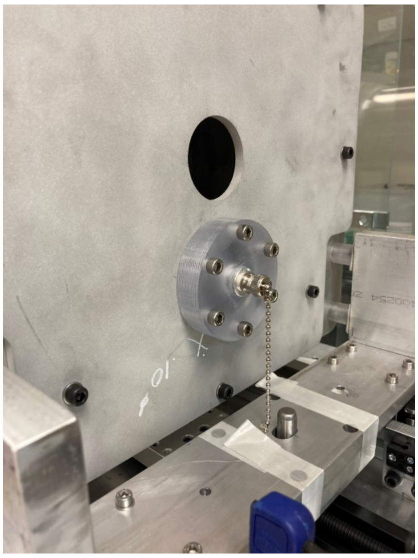

Figure 3.15: The front of the FAC showing the guard and the BNC connector that has been drilled into the collecting rod. The dust cap was temporarily on the the connector until it was wired to be accessible from outside the shielding.

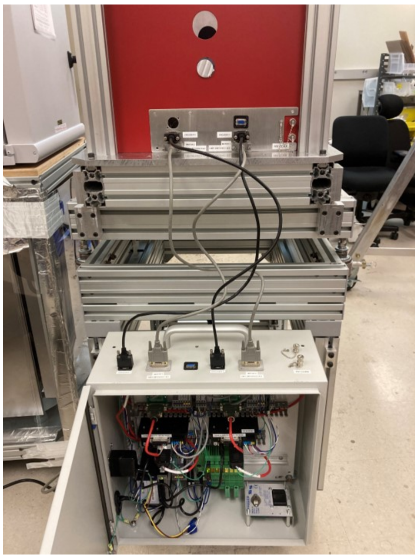

Figure 3.16: The back of the FAC showing how all of the wiring was run through the back of the shield to a control box. The box holds the power supplies and encoders for the stepper motors as well as the HV supply for the FAC. The wiring includes the HV wiring, the signal wire, and wires for the stepper motors and limit switches.

Figure 3.17: A front view of the 5 mm tungsten aperture. The aperture is held with the pins that have been press fit into the steel plate and the screws which can be removed to switch out the apertures. This picture was taken after alignment during a measurement course so the 1 m green laser can be seen at the back plane of the aperture at the POM and the cross laser can be seen shining through the aperture.

3.2 Correction factors

The FAC signal must be corrected for temperature, pressure, ion recombination, polarity and electrometer accuracy in the same manner as a typical ionization chamber. The temperature and pressure correction follows

$$P_{TP} = \frac{273.15 + T_{air}}{273.15 + T_0} \times \frac{P_0}{P_{air}}, \tag{3.7}$$

as outlined in TG-51 [69] where T_0 and P_0 are the standard temperature and pressure. The electrometer correction is simply the calibration coefficient reported on the electrometer. The ion recombination and polarity corrections require measurement and will be outlined in Section 3.4.2. Outside of these typical correction factors, free-air chambers require additional collection efficiency correction factors. They account for scatter contribution to the signal, signal reduction due to electron loss in the collecting volume and attenuation of the x-ray beam along the path from the POM to the center of the collecting volume. These correction factors were measured in past free-air chambers, but required dismantling for some of the measurements, which modifies a primary standard [17, 66, 70] . In response, Monte Carlo became the standard method for calculating the factors [71–73]. The EGSnrc user code, egs_fac, is a self-consistent Monte Carlo code that calculates each of the relevant correction factors [74]. EGSnrc is particularly well-suited for these correction factors because of its excellent approximation of electron transport at low energies [75]. Table 3.1 gives descriptions of each of the correction factors and their relationship to unity. The correction factors less than one remove the contribution of photons that penetrate through the tungsten aperture or that scatter out of the x-ray beam but still are collected. The correction factors that are greater than one replace electrons that collide with the wall or collecting rod before depositing all of their energy in the air, and replace x-rays that attenuate before reaching the collecting volume. The attenuation correction factor will be discussed in Section 3.4.3.

Table 3.1: Free-air chamber correction factors

Correction factor	Description	Relationship to unity
k_{ap}	Aperture penetration correction	<1
k_s	Scatter correction	<1
k_e	Wall electron loss correction	>1
k_{sh}	Collecting rod electron loss correction	>1
k_{att}	Attenuation correction	>1

The geometry model of the FAC is simplified for simulation and is shown in Figure 3.18. A number of settings were used universally across all the simulations in this work, regardless of the user code. Rayleigh scattering was turned on. The bremsstrahlung cross sections used the NRC library [76–78] and the bremsstrahlung angular sampling used the higher order Koch-Motz sampling technique [79]. Electron impact ionization was turned on, and the photon cross sections utilized the XCOM library [80]. All other parameters were set to their default values. The values for ECUT and PCUT, which respectively specify the electron and photon energy below which the particle history is terminated, were both set to 1 keV. The value for ECUT must be 512 keV to account for the rest mass energy of an electron. Each simulation was run with 10^8 histories. The source was a disk source of parallel photons to approximate an x-ray beam. With the use of the UWMRRC computing cluster, variance reduction was not required for these simulations.

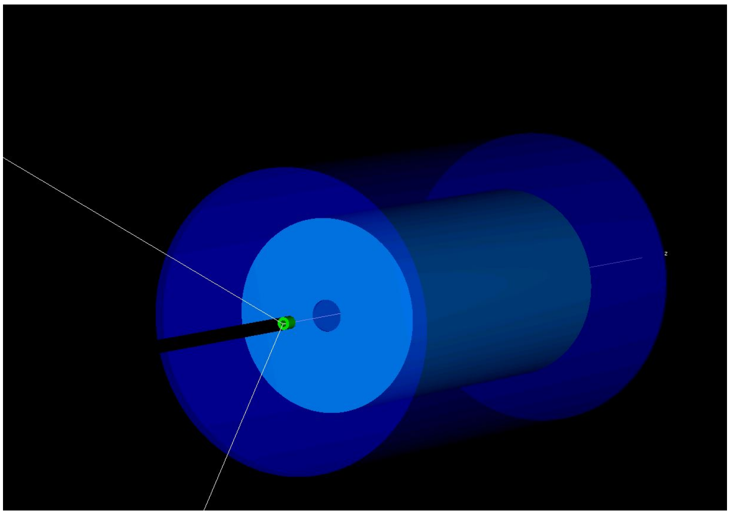

Figure 3.18: The simplified geometry of the FAC used in the Monte Carlo simulations. Dark blue represents the lead shielding, light blue is the aluminum FAC, and green is the tungsten aperture. The air cylinder has been removed for a clearer view.

The correction factors were determined for monoenergetic photons in 5 keV increments from 10 to 320 keV instead of simulating each x-ray beam quality. This was due to the large amount of beam qualities used or developed for this project. The weighted average of the correction factors could be calculated for any x-ray quality, including future qualities, without requiring a full simulation. For a photon fluence spectrum, $\phi(E)$, either measured or simulated, the weighted average for each correction factor, $k(E)$, were calculated by

$$\overline{k} = \frac{\int_{E_{min}}^{E_{max}} k(E)\phi(E)\mathrm{d}E}{\int_{E_{min}}^{E_{max}} \phi(E)\mathrm{d}E}. \tag{3.8}$$

Figure 3.19 shows the correction factors for monoenergetic photons and Figure 3.20 shows the weighted average correction factors for the M-series beams. The mononenergetic correction factors are consistent with the literature for FAC's of similar size [20]. Features of these graphs include the dip in the aperture penetration correction due to the tungsten K-edge that occurs at 69.5 keV and the local minima in the electron loss correction factors due to the dominant photon interaction process switching from the photoelectric effect to Compton scattering. This minimum occurs at a lower energy for the collecting rod because the collecting rod is closer to the x-ray beam than the walls. The error bars represent one standard deviation. To verify that the weighted average method works, the correction factors were simulated with the UW-250M x-ray spectrum that was measured as part of Jacqueline Moga's thesis work [81]. This comparison is shown in Table 3.2 which shows the values agree well and the weighted average approach is appropriate.

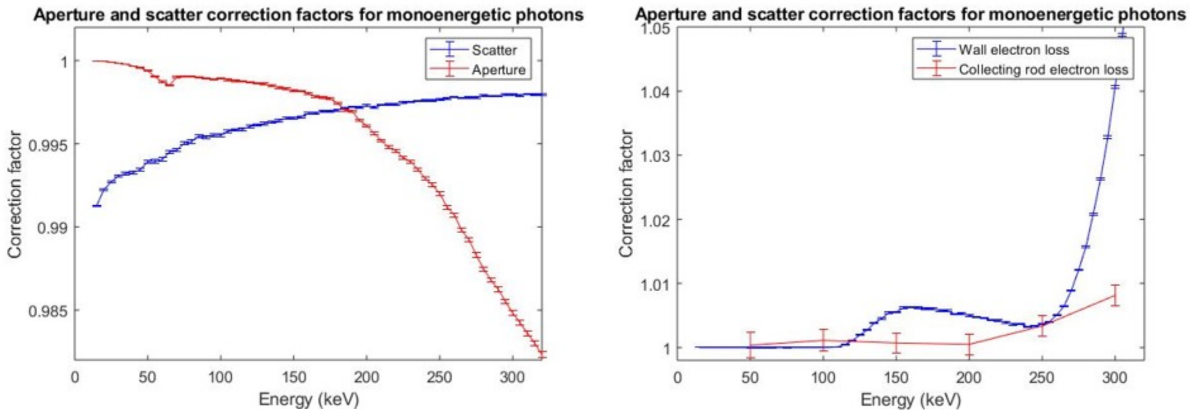

Figure 3.19: Correction factors for monoenergetic photons. The error bars represent one standard deviation.

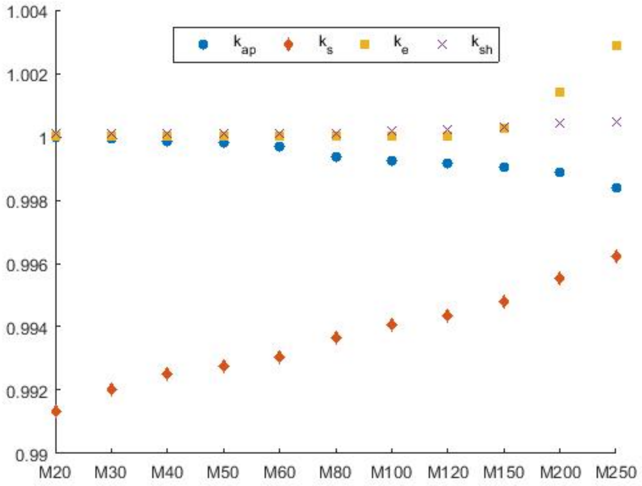

Figure 3.20: M-series x-ray beam collection efficiency correction factors for the FAC.

Table 3.2: UW-250M correction factor comparison

Correction factor	Weighted average value	Full simulation value	Percent difference (%)
k_{ap}	0.9981(6)	0.9982(6)	0.01
k_s	0.9962(8)	0.9964(7)	0.02
k_e	1.0029(6)	1.0034(10)	0.05

3.3 Electric field simulation

The electric fields inside the FAC and the known-volume ionization chambers were modeled using COMSOL Multiphysics® (Stockholm, Sweden) finite element analysis software. The 3D electric fields can be simulated with an axisymmetric 2D model using the AC/DC Electrostatic Application Module because the FAC and the ionization chambers are symmetric. The FAC was specifically designed so that electric field nonuniformity at the ends of the chamber is acceptable by using the variable-length design. The high voltage of the cylinders, especially at sharp corners and where it comes near the grounded guards, becomes a concern as a coronal discharge can occur when the electric field is above 3000 kV/m. This discharge is unsafe and can damage the FAC. Electric field simulations were used to design these areas of the FAC to keep the electric field below 1000 kV/m to be conservative. To determine the bias for the FAC, saturation curve measurements needed to be acquired which would not happen until the FAC was fully built. It was estimated that the bias would be between 2 and 4 kV so the simulations were performed with the HV plates biased to 4 kV to be conservative. Figure 3.21 shows the COMSOL rendering. The separation between the high voltage plates were increased and the radiusing of the HV plates was increased until the electric field dropped below 1000 kV/m. Radiusing in this context refers to the machining term to round edges to a specified radius. It was determined that the guards at ground and the high voltage plates needed to be separated by 1.5 cm and the 0.25 inch thick high-voltage plates needed to be radiused to at least 0.1 inch. Special attention was paid to these parameters during manufacturing and assembly of the FAC.

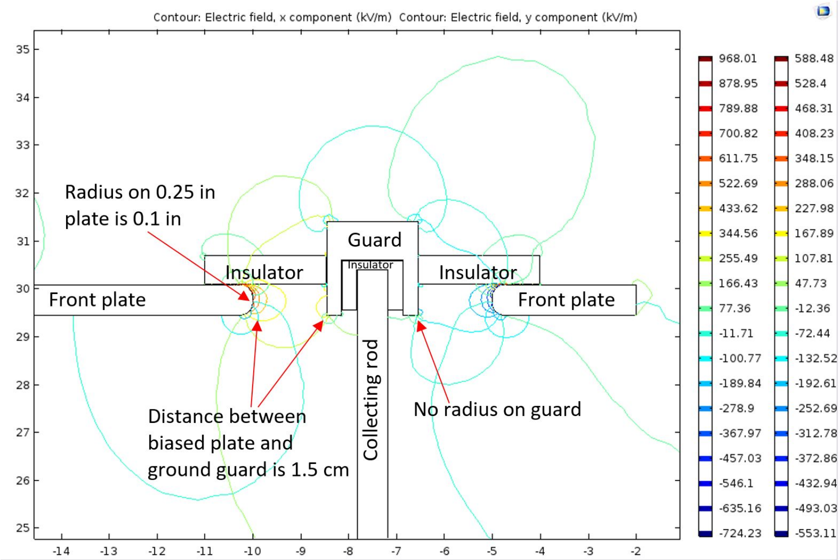

Figure 3.21: A 2D rendering of the collector guard system at the front of the FAC, with the electric field from the COMSOL simulation. This shows the optimized parameters needed to avoid a coronal discharge in the FAC. The same COMSOL simulation was run on the back of the FAC with the same results, so only the front of the FAC is presented here.

3.4 Measurements for establishment and validation

3.4.1 FAC tolerances

3.4.1.1 Alignment

Due to manufacturing tolerances and errors, there was the potential that the FAC could not be perfectly aligned from the perspective of the x-ray beam. To address these concerns, tolerances were calculated for manufacturing and assembly. This was done by investigating how the scatter and electron loss correction factors change with various possible alignment errors. Since the correction factors quantify the amount of scatter and electron loss occurring, these factors deviating from unity more than the perfect case would indicate that the misalignment is of concern. The misalignment errors that were investigated include a gap between the telescoping cylinders, translation of the FAC off center, and yaw of the FAC. The translation was done along the x-axis, but because the FAC is symmetric, translation in the y-direction should cause the same effect as in the x-direction. This is also the case with the pitch and yaw. It was found that a small misalignment not visible to the naked eye would not affect the correction factors. Essentially, as long as the x-ray beam could pass through the FAC unencumbered there would be no issue. Figures 3.22, 3.23, and 3.24 show the behavior of the correction factors with the various misalignments. During FAC assembly, shims were used between the trusses and the polycarbonate washers to keep the FAC level and reduce pitch and yaw misalignment.

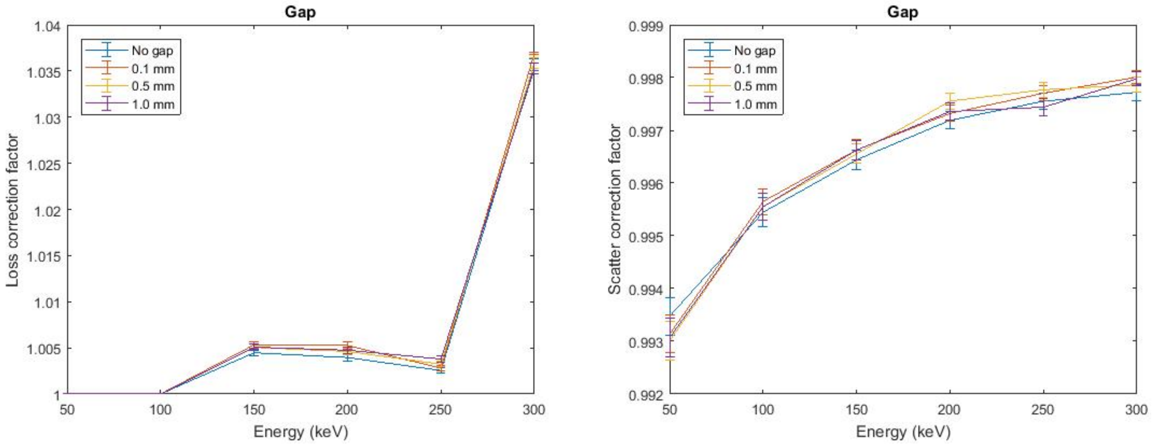

Figure 3.22: The electron loss correction factors (left) and photon scatter correction factors (right) with increasing gaps between the inner and outer cylinders. The maximum gap was determined to be 5 mm from manufacturing tolerances.

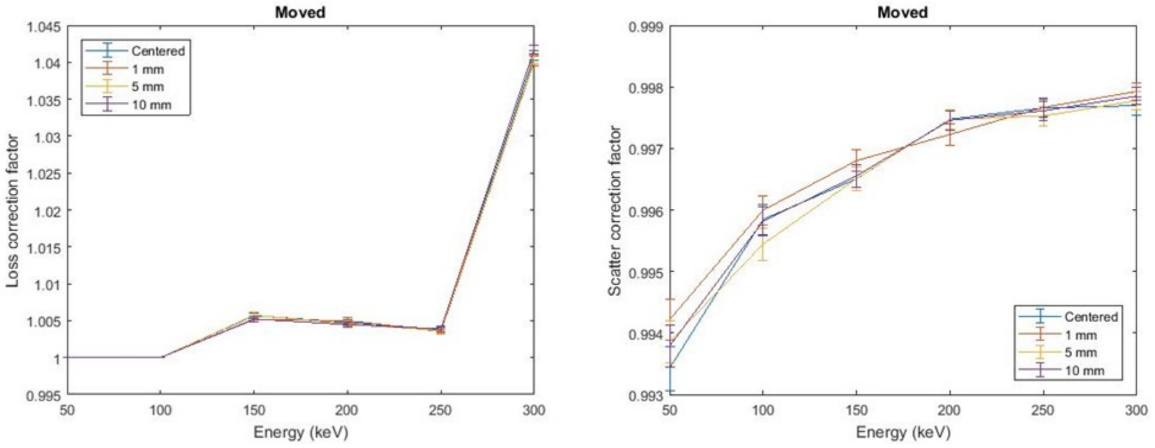

Figure 3.23: The electron loss correction factors (left) and photon scatter correction factors (right) with increasing translation of the FAC along the x-axis. Any movement beyond 10 mm would be visibly off center.

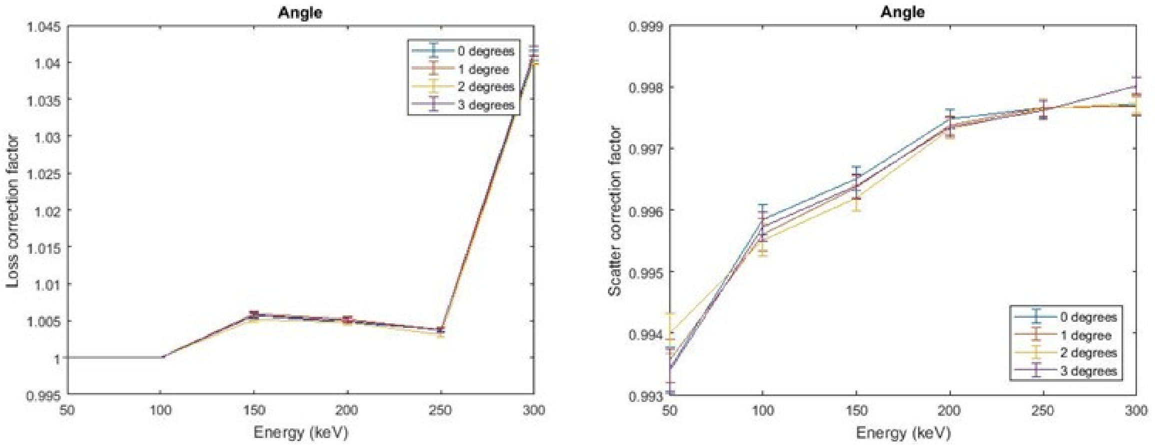

Figure 3.24: The electron loss correction factors (left) and photon scatter correction factors (right) with angle of the FAC relative to the z-axis. Larger angles would be noticeably misaligned.

3.4.1.2 Gaps in shielding

Since each shield piece is manufactured separately, it is not possible to get a perfect seal at the edges of the shielding box. Also, there needs to be some wiggle room between the sides and the front/back of the shielding since it will have the ability to be lifted off to have access to the FAC. The MCNP model for determining the shielding thickness was modified to ensure that a gap in the shielding up to 1 cm would not affect the flux of of particles significantly. The flux was 0.4144 particles/cm^2 without the gaps and was 0.4145 particles/cm^2 with the gap, both with a standard deviation of 0.13%. Therefore, a slight gap in the shielding does not affect the in-scatter. The shielding was designed with a 0.25 inch gap which equates to 0.635 cm.

3.4.2 Recombination and polarity measurements

Once the FAC was fully assembled, the first step was to check the SNR. There were efforts made when assembling the FAC to reduce the noise, specifically cleaning the electrically critical parts to remove oil and dust and then handling with gloves until permanently affixed. The leakage signal was found to be on the order of 50 fA and the actual signal was found to be on the order of 1 nA for the M-series beams which leads to an SNR of 50,000. The SNR was deemed acceptable for future measurements.

The next step was to determine the applied voltage by measuring the ionization saturation. The absorbed dose deposited in a gas by ionizing radiation is proportional to the charge produced in the gas, but the amount of charge collected is less than the charge produced because of recombination of some positive and negative ions within the gas. An ionization chamber is said to be "saturated" when ionic recombination is absent. Increasing the bias on the chamber generally decreases the recombination and asymptotically approaches saturation. It's not possible to increase the applied potential indefinitely to completely eliminate recombination because of electrical breakdown of insulators or gas multiplication. It is necessary to calculate the magnitude of the charge deficiency and make a correction to obtain the charge produced in the chamber. The ionization saturation as a function of applied collecting potential was measured with the UW-250M beam which has a nominal air kerma rate of 1.633 mGy/s. The measurements were acquired with the FAC in its fully open and fully closed positions and with a negative applied voltage. The amount of charge collected is less for the fully closed position but the slope of the saturation curves should be the same for both, which was the case. The 1/charge readings vs. 1/voltage (Jaffe plot) is plotted in Figure 3.25 and extrapolated to the (1/voltage)=0 axis to obtain the ionization for complete saturation. The data shows that the linear region of the curve lies between -5000 V to -3000 V. An applied voltage of -3600 V was chosen which leads to a recombination correction factor of 1.01. The measurements were repeated with positive applied voltages to determine the polarity correction factor. The difference in the charge readings with the different polarities was very small as shown in Figure 3.25. At -3600 V, the polarity correction is 1.002.

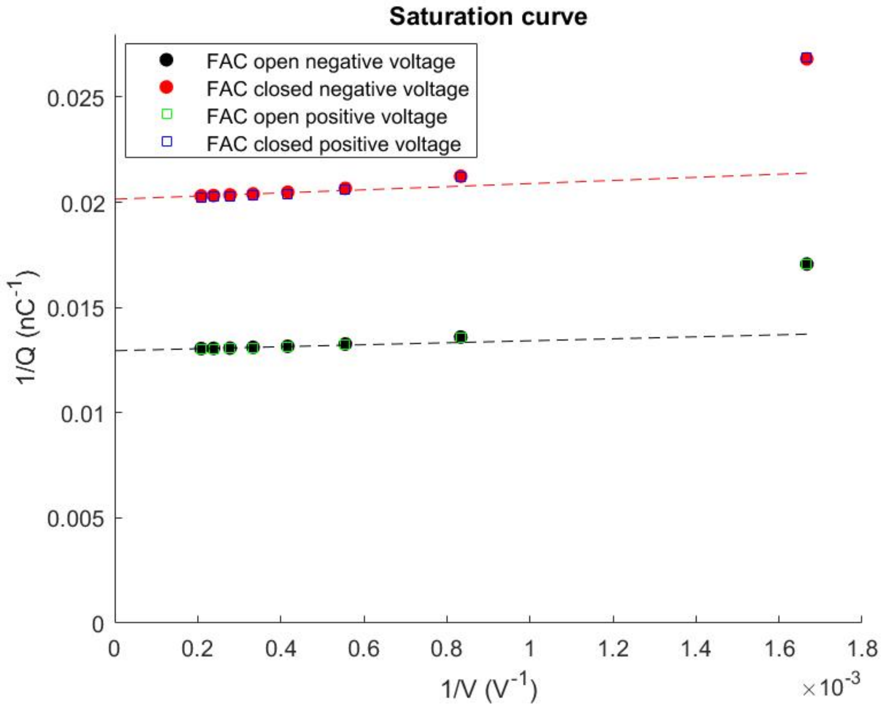

Figure 3.25: Saturation plot for the FAC used to determine the applied voltage. The dashed lines indicate the best fit lines of the linear regions of the curves to extrapolate to an infinite voltage.

3.4.3 Air attenuation measurements

For the Attix FAC, air attenuation was measured before each set of measurements. This was a relatively easy measurement due to its rail positioning system and was necessary due to the computational limitations at the time of its development. This medium-energy FAC is currently on a simple cart that makes alignment a difficult and long process and performing air attenuation measurements that require multiple alignments would be a prohibitive process. Since the establishment of the Attix FAC, Monte Carlo and computing power has improved significantly and it is now possible to simulate the air attenuation correction factors which are part of the egs_fac user code as mentioned previously. Simulated air attenuation correction factors are not as commonly used as measured factors, so these correction factors required benchmarking. The UW-150M and UW-250M beams on the NDI-451Be x-ray irradiator were used for this purpose. The spectra of the beams were simulated using the beam model that will be discussed in Chapter 5. A weighted average was then taken with these spectra using the attenuation correction factors that were simulated for monoenergetic photons. The attenuation correction factors were then measured by taking two measurements: one with the POM at 1 m from the focal spot of the x-ray tube (the standard position of the FAC) and one with the center of the collecting volume at 1 m from the focal spot. The ratio of the measurement with the collecting volume at 1 m to the POM at 1 m, corrected for $1/r^2$, is the measured correction factor. They were measured with the FAC in its open position and closed position which were found to be consistent with each other. Table 3.3 shows that the simulated and measured air attenuation correction factors agree well within 0.1%.

Table 3.3: Air attenuation correction factor benchmarking

Beam code	Measured correction factor	Simulated correction factor	% difference
UW-150M	1.0207	1.0203	0.039
UW-250M	1.0183	1.0176	0.070

3.4.4 Inter-comparison measurements

The medium-energy FAC was compared to the Attix FAC and the medium-energy x-ray standard at the UWADCL to verify its accuracy. The standard is an Exradin A3 ionization chamber as outlined in Chapter 1. Timed charge versus cylinder separation measurements were made on the UWADCL Comet (Flamatt, Switzerland) MXR-320/26 tube assembly with the UW M-series x-ray beams. The slopes of the charge versus cylinder separation data were determined and the air kerma rates were calculated from Equation 2.9. All corrections outlined above were applied for each specific beam. Tables 3.4 and 3.5 shows the air kerma rate measured by the FAC with the 1 cm diameter aperture and the 0.5 cm aperture, respectively, compared to the air kerma rate measured by the A3 chamber. Table 3.6 shows the air kerma comparison between the medium-energy FAC and the Attix FAC which can only be measured in the UW50-M beam. The A3 chamber measurements are the two most recent standard measurements at the time of compiling this data, averaged. The FAC measurements are three measurements taken over the course of three different days across the span of a few months to evaluate the reproducibility. The repeatability of the FAC is evaluated in the Uncertainty Analysis section. The medium-energy FAC data yield consistent air kerma rates when compared to the A3 ionization chamber and the Attix FAC, agreeing to better than 0.8%, within the medium-energy FAC uncertainty of 1.33% and the uncertainty of 0.9% for the A3 chamber calibration.

Table 3.4: FAC benchmarking data with 1 cm aperture

Beam code	Average standard measurement (mGy/s)	Average FAC measurement (mGy/s)	Percent difference (%)
UW-50M	2.0033	2.010	0.334
UW-60M	1.7793	1.789	0.545
UW-80M	1.8092	1.806	-0.177
UW-100M	1.8113	1.819	0.425
UW-120M	2.3530	2.358	0.212
UW-150M	2.1597	2.165	0.245
UW-200M	1.9188	1.913	-0.302
UW-250M	1.6242	1.633	0.542

Table 3.5: FAC benchmarking data with 0.5 cm aperture

Beam code	Average standard measurement (mGy/s)	Average FAC measurement (mGy/s)	Percent difference (%)
UW-50M	2.0033	2.002	-0.065
UW-60M	1.7793	1.785	0.320
UW-80M	1.8092	1.801	-0.453
UW-100M	1.8113	1.817	0.315
UW-120M	2.3530	2.360	0.297
UW-150M	2.1597	2.174	0.662
UW-200M	1.9188	1.926	0.375
UW-250M	1.6242	1.637	0.788

Table 3.6: Attix FAC compared to medium-energy FAC in the UW-50M x-ray beam

Attix FAC (mGy/s)	Medium-energy FAC 1 cm aperture (mGy/s)	Medium-energy FAC 0.5 cm aperture (mGy/s)	Max. percent difference (%)
1.992	1.998	1.990	0.301

3.5 Uncertainty Analysis

The method of this uncertainty assessment, as well as all other uncertainty assessments presented in this thesis, followed the recommendation of the Bureau International des Poids et Mesures (BIPM) [82]. The uncertainty estimates are of two kinds: Type A are random uncertainties derived as standard deviations of the mean of quantities that are repeatedly measured. Type B are subjective best estimates of uncertainties based on experience and are estimated to correspond to approximately a 67% confidence limit. Type A can be thought of as the precision of the measurement while Type B represents the accuracy. Type A and B uncertainties are combined by taking the quadratic sum of each type separately and then are combined by the same quadratic method to obtain the coverage factor of k=1 uncertainty for A and B types together. This is doubled to yield the expanded uncertainty of the measurement, that is its coverage factor of k=2 or 95% confidence level.

For the medium-energy FAC, this uncertainty assessment was performed for each of the parameters affecting the quantities of Equation 2.9. For charge, Type A is the repeatibility of the measurement or the standard deviation in the charge measurement taken four times in succession. The various diameters of the aperture were measured with precision gauges to an accuracy of 25 μm. The pitch of the screw drive controlling the cylinder separation is 2 mm and is driven by a stepping motor with 20,000 steps per revolution. The uncertainty associated with the ability to return to the same cylinder separation is reflected in the precision of the first and last charge measurements. The correction factor uncertainty is the combined uncertainty of the highest uncertainties reported from the spectral weighed average of simulations done in the EGS user code egs_fac. It also includes the uncertainty in the energy spectra of the M-series as reported in the thesis work of Dr. Moga [81] which is the dominant contribution to the uncertainty. The uncertainty in air density refers to the uncertainty in correcting charge measurements to dry air conditions. Since the FAC has a large volume, it is more sensitive to ambient radiation background than the much smaller volume field instruments. The reported uncertainty of the fluence of particles that penetrate the shielding in MCNP simulations is used for the penetration of chamber by scattered x-rays. This analysis, details of which are shown in Table 3.7, yielded an expanded uncertainty for air kerma measurements of 1.33% at the k=2 level for the medium-energy FAC.

Table 3.7: Medium-energy FAC uncertainty budget

Quantity	Type A (%)	Type B (%)
Charge measurement	0.01	
Aperture area		0.207
Change in length, ΔL	0.006	0.01
Correction factors		0.59
Air density		0.1
$\frac{W}{e}$		0.15
Humidity		0.03
Radiation background		0.01
Recombination loss	0.01	
Polarity difference	0.007	
Penetration of chamber by scattered x-rays		0.075
Electrometer calibration		0.1
Distance from source	0.033	
Rotation, tilt off-axis error		0.058
Standard Uncertainty (k=1)	0.667	
Expanded Uncertainty (k=2)	**1.33**	

Chapter 4

Known-volume ionization chamber development

4.1 Volume calculation

Exradin A3 ionization chambers are often used at the secondary standards level for standard measurements in the medium-energy x-ray range. They have a nominal volume of 3.6 cm^3 but due to variations in machining and uncertainty in the shape of the electric field within the chamber the exact volume is not known. For this reason, these chambers, and all commercial ionization chambers, require calibration in a known field. Standard ionization chambers at secondary standards laboratories are calibrated at NIST against the primary standards, and then clinical or research chambers are calibrated against this secondary standard. To develop an absolute dosimeter that can measure higher energies than the medium-energy FAC, the volumes of two Exradin A3 ionization chambers were measured to be known-volume ionization chambers.

4.1.1 Imaging and surface determination

A Siemens Inveon microCT/microPET hybrid scanner at the University of Wisconsin's Small Animal Imaging Facility (UW SAIRF) was used to image the chambers. The scanner specifications and scan techniques are listed in Table 4.1. The Siemens Inveon scanner is designed for mouse imaging with a bed that the ionization chambers were placed on horizontally.

Table 4.1: Known volume spherical chamber correction factors

Parameter	Value
Resolution	50 μm
kV	80 kVp
Rotation range	360 deg
Convolution kernel	Filtered backprojection
Nominal voxel size	0.0315 x 0.0315 x 0.0315 mm^3

The two ionization chambers were manufactured with different techniques in different eras and were both quantified to verify the reproducibility of the methods. To calculate the volume, the air within the chamber needs to be segmented from the walls, collector, guard, etc., within the chamber. The imaging software is then able to calculate the contoured volume. Due to the finite resolution, a partial volume effect occurs where material and background partially overlap resulting in an intermediate gray value which gives the appearance of blurring. A well-defined surface is needed for proper volume calculation. The ISO-50% method is a global method of surface determination based on a static threshold value that is commonly used in additive manufacturing quality assurance [83]. The ISO50 value is half of the sum of the average material grey Hounsfield Unit (HU) and the average background grey HU value. This ISO50 value is used as a threshold where every HU value greater than or equal to the threshold is considered material and every HU value below is considered background. The ISO-50% method is used in this work to define the inner and outer walls of the ionization chamber to determine the physical volume and wall thickness of the chambers. To properly determine the physical volume, the surfaces of the collecting electrode and the guard were also defined. A MATLAB script was written to import the DICOM data and calculate the ISO50 value for each chamber. An ISO50 value was calculated for each slice of the chamber and then averaged. Figure 4.1 shows an example of the raw DICOM data for a single slice of a chamber and how the ISO50 value was calculated. The ISO50 value for the S/N: 256 chamber was -743 HU and the value for the S/N: XR191680 chamber was -825 HU.

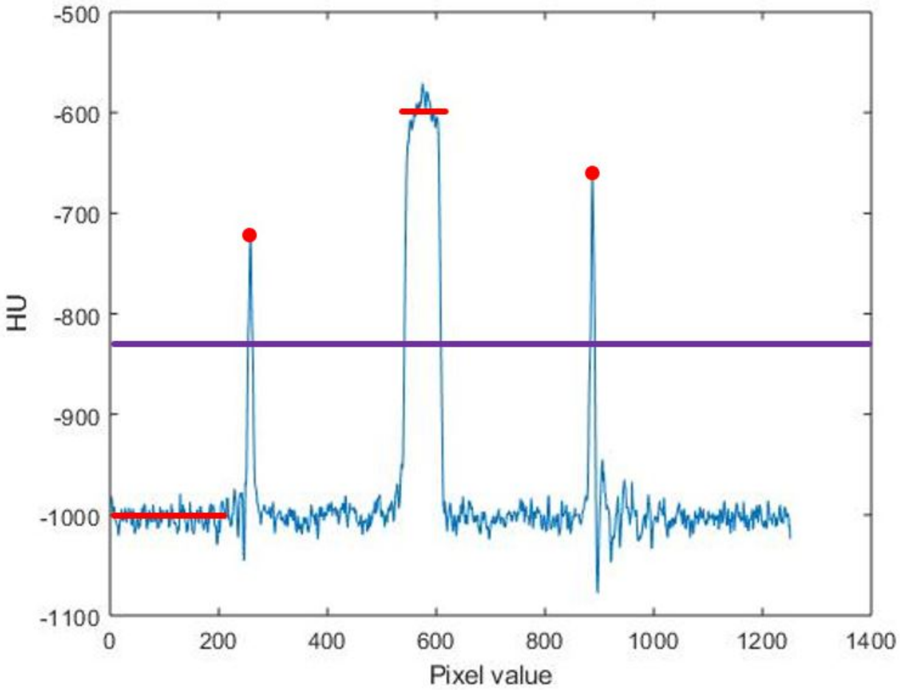

Figure 4.1: An example DICOM slice from one of the A3 ion chambers. The red lines and dots indicate the material and background values used to calculate the ISO50 value indicated by the purple line.

The ISO50 values were then used as the thresholds for contouring the chambers in the Siemens Inveon Research Workspace imaging software, as shown in Figure 4.2. The start of the guard marks the lowest contoured slice as made evident by Figure 4.2. From these contours the software calculated a gross volume that required an electric field and magnification correction. There was originally a concern that the buildup cap on the S/N: 256 chamber was compressing the chamber causing the volume to be smaller than when the buildup cap was absent. Originally, an arbitrary surface threshold was chosen for both chambers which caused the S/N: 256 chamber volume to be underestimated. By applying separate ISO50 thresholds for each chamber, no appreciable difference between the volumes was found with or without the buildup cap. The raw imaging volumes were 4.00 cm^3 and 3.83 cm^3 for the S/N: XR191680 and the S/N: 256 chamber, respectively.

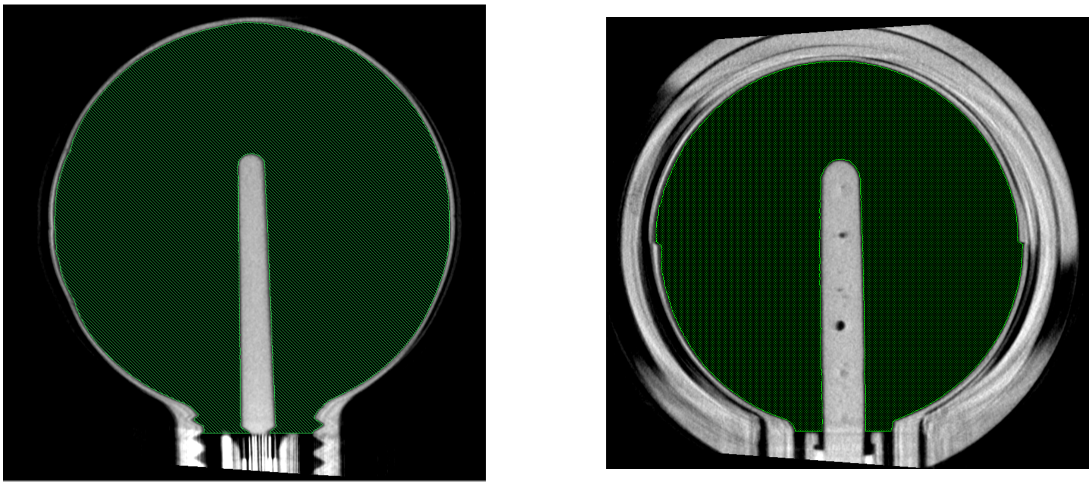

Figure 4.2: A coronal view of the ionization chambers with the contours shown in green. The newer model (S/N: XR191680) is on the left and the older model (S/N: 256) is on the right.

4.1.2 Electric field simulation

The collecting volume of the ionization chambers differ from the physical volumes due to a portion of the electric field terminating in the guard instead of the collecting electrode. The electric field was modeled in COMSOL Multiphysics to quantify this discrepancy [84], as shown in Figures 4.3 and 4.4. The measurements used for the COMSOL models were performed with the measure tool in the imaging software as shown in Figure 4.5. The area under the curve where the electric field still reaches the collecting electrode, rather than the guard, was converted to a volume by rotating the area around the collecting rod. Assuming the electric field is symmetric about the collecting rod, the equation for rotating this area is

$$V = 2\pi \int_a^b r \cdot f(r)\mathrm{d}r \tag{4.1}$$

where a is the radius at the collecting rod, b is the radius at the stem, r is the radius of each bin and $f(r)$ is the height of the electric field at each bin. This volume was then subtracted out of the volume determined by the contours in the previous section. After electric field subtraction, the volumes were 3.99 cm^3 and 3.82 cm^3 for the S/N: XR191680 and the S/N: 256 chamber, respectively.

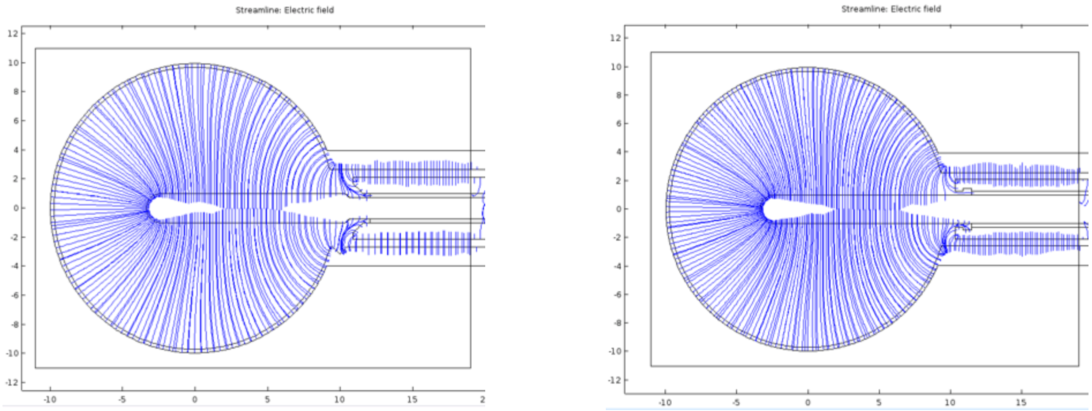

Figure 4.3: The electric field simulations in both ionization chambers. The newer model (S/N: XR191680) is on the left and the older model (S/N: 256) is on the right.

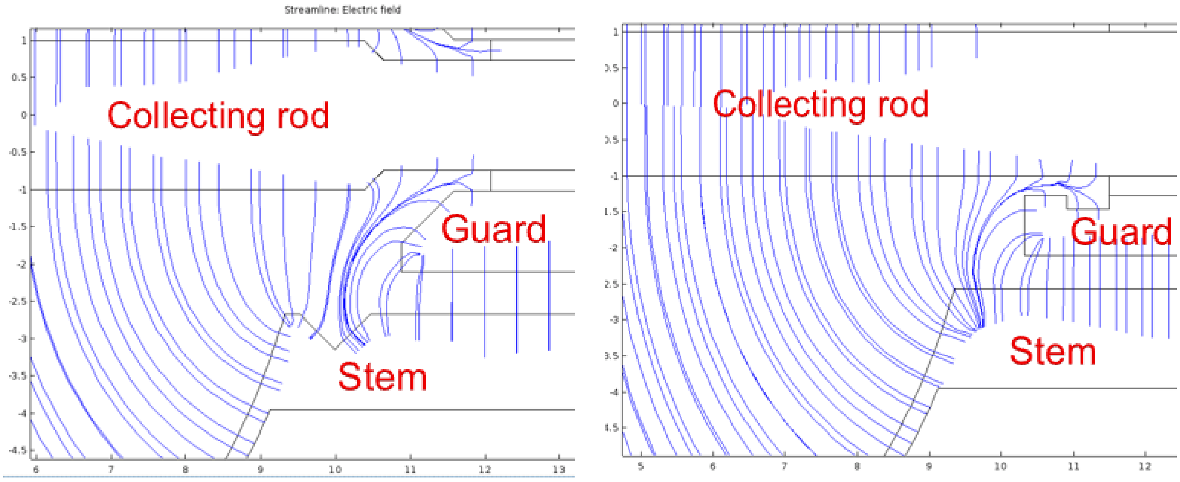

Figure 4.4: A close up of the electric field near the guard in the ionization chambers. The newer model (S/N: XR191680) is on the left and the older model (S/N: 256) is on the right.

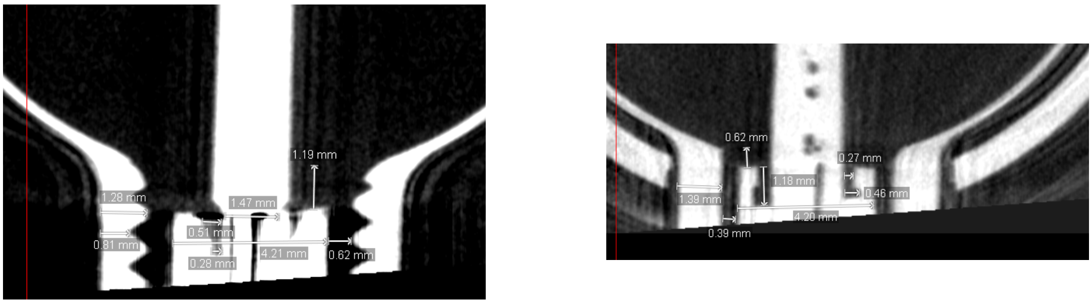

Figure 4.5: Measurements of the guard area of the chambers used for the COMSOL models. The newer model (S/N: XR191680) is on the left and the older model (S/N: 256) is on the right.

4.1.3 Magnification factor

The "Geometry calibration number" is a feature of the Siemens Inveon Scanner that automatically corrects for magnification that occurs. This factor is within the machine's tolerances but was not accurate enough for the level of precision required for this application. Therefore, a new magnification factor needed to be applied. A phantom with a known-diameter (confirmed with calipers) was imaged at the same medium-high magnification setting as the ionization chambers. The center slices from an axial and coronal view were taken, smoothed to remove the different HU plugs in the phantom, and the full-width half-maximum (FWHM) computed. Figure 4.6 shows the image of the phantom and the axial slice HU data used to calculate the FWHM. The magnification factor is then the ratio of the two averaged FWHMs to the phantom's measured diameter. The reader should note that the FWHM is equal to the ISO-50 method in this case. At the medium-high magnification setting the magnification factor is 1.04 in each dimension. The volume that was calculated from the contour with the electric field subtracted out is then divided by this factor, cubed. The factor must be cubed to account for 3-dimensional volume. After applying the magnification factor, the final volumes were 3.55 cm^3 and 3.40 cm^3 for the S/N: XR191680 and the S/N: 256 chamber, respectively.

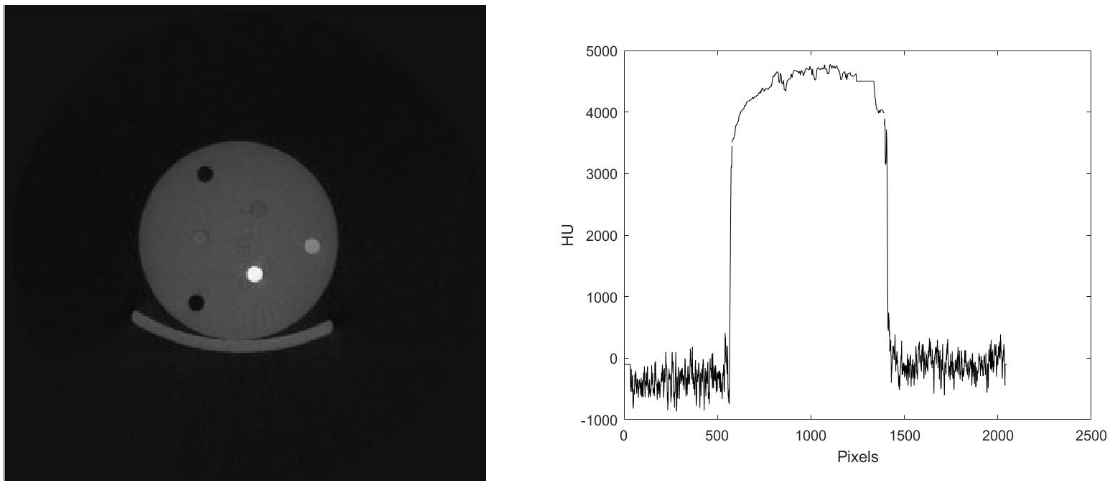

Figure 4.6: The image of the phantom used for calculating the magnification factor on the left and the center axial slice HU data on the right.

The μCT scanner used in this project was not designed for metrology where dimensional accuracy is essential, although these scanners do exist. The key to known volume calibration is to perform the geometry calibration described in this section that converts nominal voxel dimensions to actual dimensions. This calibration should be established for the specific reconstruction parameters that are used to scan the chamber.

4.2 Correction factors

Like free-air chambers, known-volume ionization chambers also require correction factors. The correction factors needed to determine air kerma using the known-volume spherical chamber were calculated using various EGSnrc user codes and NIST mass attenuation values. As described in Equation 2.15, the measurement of air kerma with known-volume ion chambers can be determined by,

$$K_{air} = \frac{Q}{m(1-g)}\left(\frac{W}{e}\right)\left(\frac{\overline{L}}{\rho}\right)_{air}^{wall}\left(\frac{\overline{\mu_{en}}}{\rho}\right)_{wall}^{air} K_h K_{wall} K_{an} K_{comp} K. \tag{4.2}$$

A description of these correction factors is shown in Table 4.2. Two of the correction factors can assumed to be unity: the axial nonuniformity and wall composition factors. The axial nonuniformity correction is unity because the ionization chamber will be far from the x-ray source and the wall composition correction is unity because these chambers are made of air-equivalent plastic instead of graphite. The humidity correction factor is 0.997 when the humidity is between 15% and 75% [15] which it always is in the air-conditioned UWMRRC. These correction factors were also computed for monoenergetic photons and a weighted average was taken with relevant spectra mirroring the methods that were used to determine the FAC correction factors with the M-series spectra in Chapter 3. The known-volume chambers were benchmarked in Cs-137 and Co-60 along with x-ray sources and those correction factors were simulated directly with the source spectra.

4.2.1 Stopping power ratios

A description of the purpose of stopping power ratios in the calculation of air kerma with known-volume ionization chambers is detailed in Chapter 2. The Spencer-Attix

Table 4.2: Known volume spherical chamber correction factors

Correction factor	Description	Calculation method
$\left(\frac{\overline{L}}{\rho}\right)^{wall}_{air}$	Spencer-Attix collision mass stopping power for the wall material to dry air	SPRRZnrc
$\left(\frac{\overline{\mu_{en}}}{\rho}\right)^{air}_{wall}$	Ratio of mass energy absorption coefficients averaged over the spectrum for dry air to the wall material	NIST values
K_h	Humidity correction	0.997
K_{wall}	Corrects for attenuation and scatter in the chamber wall	CAVSPHnrc
K_{an}	Corrects for axial nonuniformity due to the point source nature of the beam	Assumed to be 1
K_{comp}	Corrects for nonuniform nature of the wall material	Assumed to be 1
K	Any other corrections needed	

mass restricted stopping powers were calculated with the EGSnrc user code SPRRZnrc [85]. The SPRRZnrc code scores the total dose deposited in two different media: the wall material and air. The δ events are recorded by scoring electrons that deposit energy below the Δ cutoff. The code then outputs the total dose and the fraction of the total dose excluding δ events. The stopping power ratios are calculated by taking the ratio of the dose components of the wall material to that of the air, both without the δ events.

For these simulations, PCUT was set to 1 keV. The Δ cutoff is set by adding the energy cutoff amount to the rest mass energy. The definition of Δ is usually taken as the energy of an electron having a residual range in air equal to L, the mean chord length of electrons in the cavity of the ion chamber [26]. For isotropic electrons uniformly entering a convex cavity,

$$L = 4V/S, \tag{4.3}$$

where V is the volume and S is the surface area [15]. Although electrons do not enter the ionization chambers isotropically, the literature shows that this simple formula is sufficiently accurate [26]. The volumes of the ionization chambers are 3.55 cm^3 and 3.40 cm^3 so the chord lengths are approximately 11.3 cm and 10.9 cm, respectively. The CSDA residual range corresponding to these chord lengths are 26.1 keV and 25.2 keV [67]. Therefore, ECUT was set to 537 keV and 536 keV. Due to the proximity of these values, any difference in stopping power ratios observed from changing ECUT was investigated to be found negligible. Therefore, only one stopping power ratio reported for both known-volume ionization chambers. The x-ray source for these simulations was a monoenergetic broad parallel photon beam with 1E6 histories and variance reduction was not required.

4.2.2 Wall correction factors

The wall correction accounts for scatter and attenuation in the chamber wall. The traditional way to calculate k_{wall} is to measure the chamber response as a function of wall material by adding material on all sides and extrapolating to zero wall thickness. This is then multiplied by a factor to account for the downstream deposition of the electrons' energy. Recently. Monte Carlo methods have been employed to calculate this correction. In this work, it is calculated using the EGSnrc user code CAVSPHnrc, which has been shown to be accurate within 0.1% [86]. The calculation method for k_{wall} used in this code is detailed in the work of Rogers and Bielajew [87]. Essentially, k_{wall} is equal to the inverse of A_{wall} which is expressed as

$$A_{wall} = A_{sc} A_{at}, \tag{4.4}$$

where A_{sc} accounts for scatter in the wall and is tallied by

$$A_{sc} = \sum_i (r_i^0 + r_i^1) \left(\sum_i r_i^0 \right)^{-1}, \tag{4.5}$$

and A_{at} accounts for attenuation in the wall and is tallied by

$$A_{at} = \sum_i r_i^0 \left(\sum_i r_i^0 e^{+d_i} \right)^{-1} . \tag{4.6}$$

The tallied energy variables include r_i^0 which is the energy deposited by electrons generated by the ith primary photon interaction, r_i^1 is the energy deposited by electrons generated from the second and higher order scattered photons that arise from the ith primary photon and d_i is the number of mean free paths in the chamber to the point of interaction of the ith primary photon.

The cavities are defined as spheres with the same volume and wall thicknesses of the two chambers. The nominal wall thickness of an Exradin A3 chamber is 0.25 mm. The actual wall thicknesses were determined by contouring the outside of the chambers with the same ISO50 threshold used in defining the inner walls. The one-dimensional magnification factor was also applied. The S/N: 256 chamber has a wall thickness of 0.33 mm without the buildup cap and 3.16 mm with the buildup cap. The S/N: XR191680 chamber has a thickness of 0.21 mm without the buildup cap and 2.71 mm with the buildup cap. The x-ray source was a monoenergetic broad parallel photon beam with 1E9 histories. ECUT and PCUT were set to 512 keV and 1 keV, respectively. Variance reduction was not required for these simulations.

4.2.3 Correction factor results

The monoenergetic correction factors are shown in Figure 4.7. The difference in the wall correction factors for the two ionization chambers is due to the difference in the wall thicknesses. Figure 4.8 shows the correction factors for the M-series beams, Cs-137, and

Co-60. The discontinuity for the Cs-173 and Co-60 wall correction factors is due to the introduction of the buildup cap.

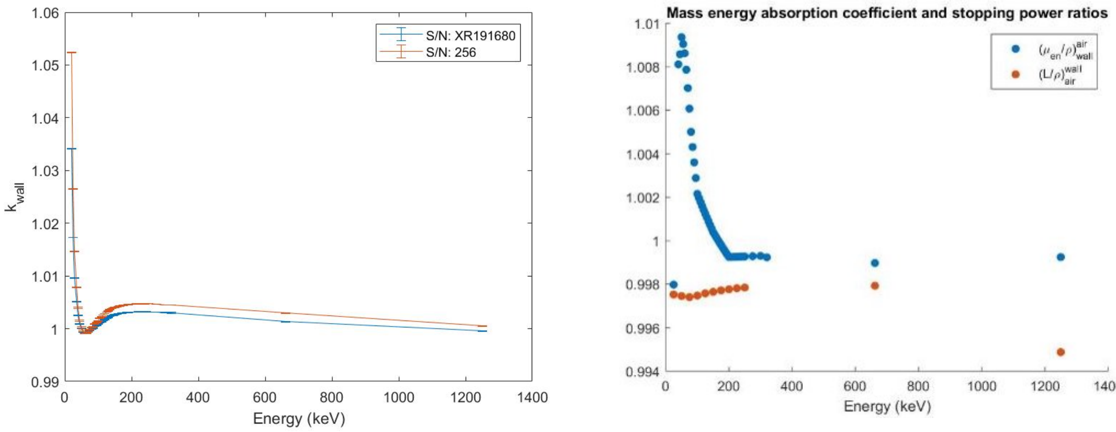

Figure 4.7: The monoenergetic correction factors for the known-volume ionization chambers are on the left and the monoenergetic mass attenuation and stopping power ratios are on the right.

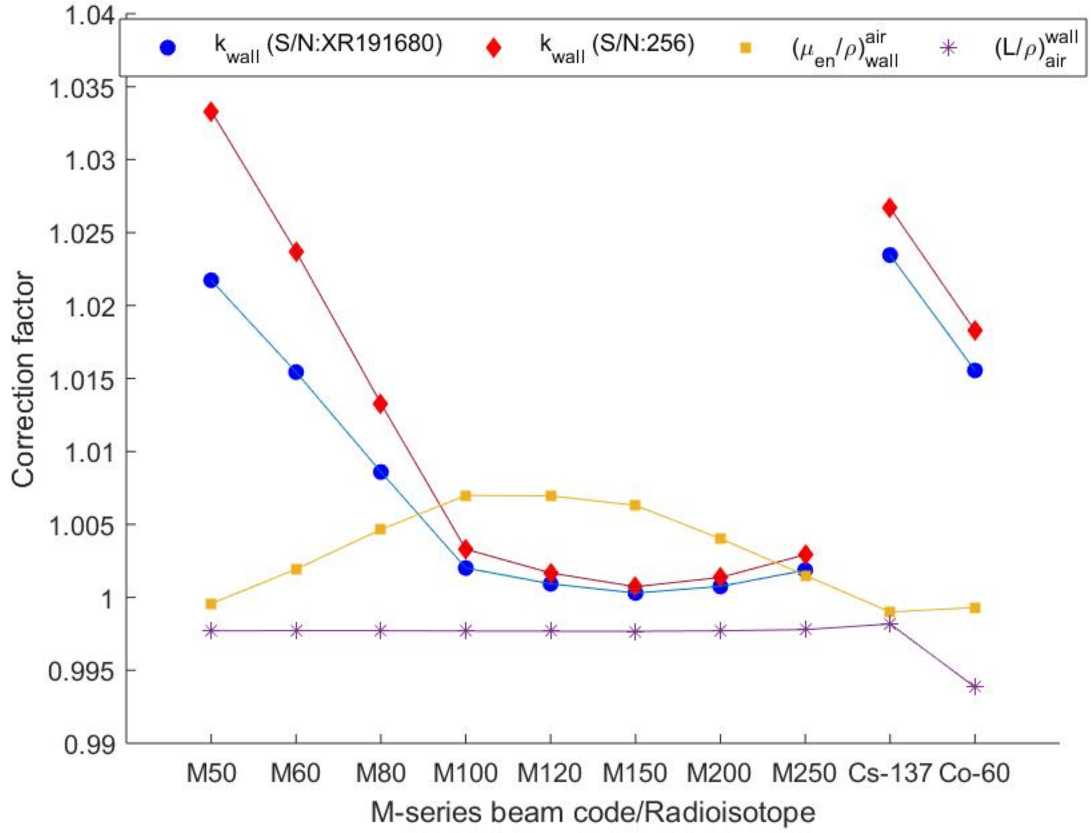

Figure 4.8: Correction factors for the known-volume chambers. The increase in the wall correction for Cs-137 and Co-60 is due to the introduction of a buildup cap.

4.3 Volume and correction factor validation

4.3.1 Calculation from air kerma calibration

The volume of ionization chambers can be estimated from their exposure calibration coefficient. As outlined in Chapter 2, the definition of exposure is

$$X = \frac{Q}{m}, \tag{4.7}$$

and calibration allows for a substitution of the calibration coefficient for the mass, N_x, so the exposure equation becomes

$$X = N_x Q. \tag{4.8}$$

By setting these equations equal to each other and changing mass to the product of the density of air, ρ, and the volume, V, we can rearrange the equation to calculate the volume as

$$V = \frac{1}{\rho N_x}. \tag{4.9}$$

Both ionization chambers were calibrated in Co-60 against the secondary standard at the UWADCL to obtain exposure calibration coefficients. The outside diameters of the ionization chambers were physically measured with calipers and the nominal wall thickness and collector width were subtracted to estimate the volume of the chambers. All of these values, for both chambers, are within the calibration uncertainty of each other which gives us confidence that the volumes of these chambers have been accurately characterized. These volumes are shown in Table 4.3.

Table 4.3: Comparison of imaging volumes to calibration and physical measurement

	Imaging volume [cm^3]	Calibration volume [cm^3]	Physical measurement volume [cm^3]	Max. deviation from imaging volume
Chamber 1 (S/N:XR191680)	3.55 ±0.90%	3.52 ± 1.50%	3.53	0.85%
Chamber 2 (S/N:256)	3.40 ± 0.90%	3.36 ± 1.50%	3.37	1.20%

4.3.2 Comparison to NIST-traceable ionization chambers

The two known-volume chambers were compared to NIST-traceable ionization chambers by measuring and comparing air kerma rates. The NIST-traceable chambers used were the Exradin A3 standard ionization chamber described in Chapter 2 and an Exradin A12 ionization chamber which was calibrated for air kerma in both Cs-137 and Co-60. The correction factors outlined in Section 4.2.3 were applied to the known-volume chamber measurements while the NIST-traceable ionization chambers had their calibration coefficients applied. Pressure and temperature corrections were applied to all chambers. All measurements were comprised of four 30-second charge readings which were then averaged. The UW-250M x-ray measurements were taken at 1 m from the focal spot with a 10x10 cm^2 field and without the buildup cap. Both the Co-60 and Cs-137 measurements were also taken 1 m from the source and with the buildup cap. Table 4.4 shows the comparisons of the results in the UW-250M x-ray beam, Cs-137 and Co-60. The known-volume chamber data yield consistent air kerma rates when compared to the calibrated ionization chambers, in agreement within 0.63%, less than the known-volume chamber uncertainty of 1.80 (k=2) and the uncertainties of 0.9% and 1.50% for the A3 and A12 chamber calibrations respectively.

Table 4.4: Known-volume ionization chamber benchmarking data

UW-250M x-ray beam	Chamber 1 S/N: XR191680	Chamber 2 S/N: 256	A3 Chamber S/N: XR022483
Air kerma rate (mGy/s)	1.642	1.644	1.634
Percent difference from A3	**0.50**	**0.63**	–
Cs-137			A12 Chamber S/N: XA060332
Air kerma rate (mGy/s)	0.1732	0.1733	0.1732
Percent difference from A12	**0.01**	**0.03**	–
Co-60			A12 Chamber S/N: XA060332
Air kerma rate (mGy/s)	16.79	16.76	16.83
Percent difference from A12	**0.23**	**0.43**	–

4.3.3 Comparison to FAC

A comprehensive comparison was compiled between both known-volume chambers, the Attix FAC, the medium-energy FAC with both apertures, the standard A3 ionization chamber and the nominal air kerma values. This is shown in Figure 4.9. The medium-energy FAC and known-volume chambers have error bars indicating the uncertainty at the k=1 level. It can be seen that all of these air kerma values agree as they are all within the error bars of each other indicating they are all within 1.36% of each other.

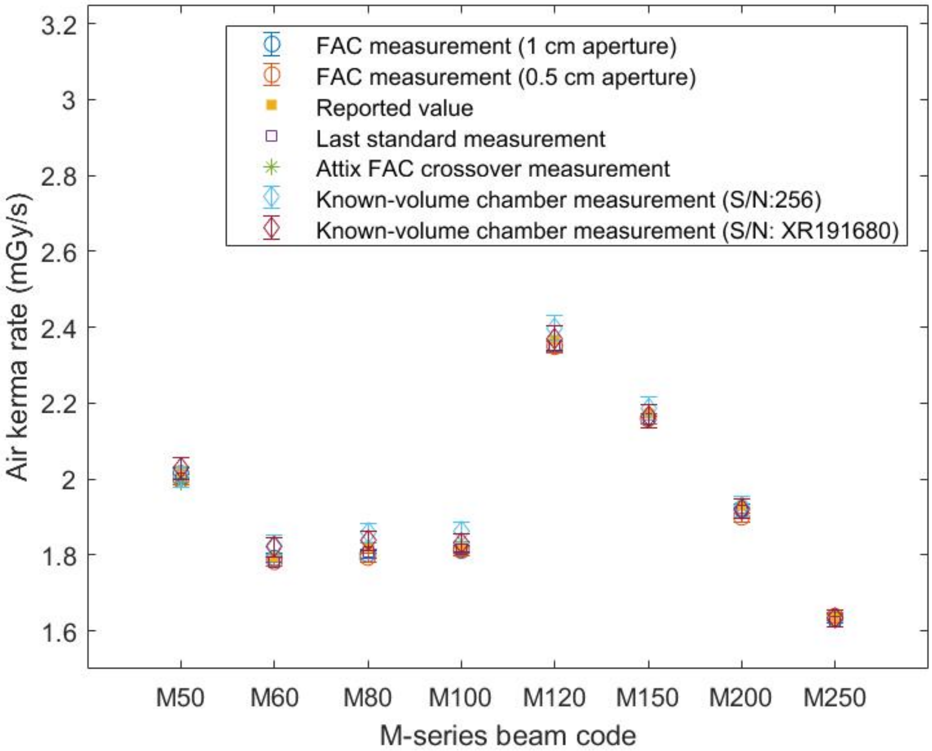

Figure 4.9: A comparison of the known-volume chambers, free-air chambers, standard ionization chamber and nominal air kerma values. All of the values are within the error bars of each other. The error bars indicate the uncertainty of air kerma at the k=1 level.

4.4 Uncertainty analysis

Four components of uncertainty were evaluated for the volume including: the resolution of the CT, determination of HU thresholds for the walls of the chamber by the ISO50 method, the electric field location, and the magnification factor. The uncertainty in the ISO50 surface determination is the standard deviation of the ISO50 value with a triangular distribution assumed. The COMSOL electric field uncertainty was determined by taking the average of the volume removed based on the electric field on either side of the collecting rod in the 2D simulation and calculating the standard deviation. For both the ISO50 surface determination and electric field correction, the higher uncertainty between the two chambers was used to be conservative. The magnification factor uncertainty was determined by calculating the magnification factor from an axial and coronal slice of the phantom and applying a rectangular distribution to the bounds of uncertainty. It also includes the uncertainty on the diameter of the phantom and accounts for the magnification factor having to be cubed.

Table 4.5: Uncertainty in the volume of the known-volume spherical chamber

Quantity	Type A (%)	Type B (%)
Resolution of CT		8.4×10^{-6}
ISO50 surface determination		0.89
COMSOL electric field correction		0.13
Magnification factor		0.04
Standard Uncertainty (k=1)	**0.90**	
Expanded Uncertainty (k=2)	**1.80**	

The uncertainty in the volume is then applied to the uncertainty in measuring air kerma. This includes typical contributions to uncertainty when measuring air kerma with ionization chambers as well as the uncertainty in the correction factors. The correction factor uncertainty is composed of the uncertainties reported by the various EGSnrc user codes and from NIST's mass attenuation coefficient database added in quadrature. It also includes the uncertainty in the energy spectra as reported in Dr. Moga's thesis [81].

Table 4.6: Uncertainty in measuring air kerma with the known-volume chambers

Quantity	Type A (%)	Type B (%)
Charge measurement	0.035	
Volume of ion chambers		0.90
Correction factors		1.0
Air density		0.1
Ionic recombination		0.03
Electrometer calibration		0.1
Distance from source s		0.033
Rotation, tilt, off-axis error		0.058
Standard Uncertainty (k=1)	**1.36**	
Expanded Uncertainty (k=2)	**2.74**	

Chapter 5

Radiobiology x-ray calibration beams

5.1 Beam model of the NDI-451Be x-ray tube

A Varex NDI-451Be (Salt Lake City, UT) x-ray tube was used for the creation of the standard beams as shown in Figure 5.1. It is an industrial x-ray tube primarily used for nondestructive testing and has a maximum tube potential of 500 kV with an inherent filtration of 5 mm of beryllium. A collimator to produce a 10x10 cm^2 field at 1 m from the focal spot was attached. A Monte Carlo model of the irradiator was developed to simulate various spectra to determine the energy-dependent FAC correction factors and for testing the matching of the beams with a wide range of filtration combinations. The EGSnrc user code BEAMnrc [88] was used to develop the model. The user code requires specification of a number of component modules which correspond to the physical components of the x-ray tube. The accelerator was built by specifying the x-ray tube components and their spacing along the beam axis. A rendering of the x-ray tube, its housing, and the beam collimation system is shown in Figure 5.2.

The Bremsstrahlung production process is inefficient, so variance reduction techniques were implemented to reduce the simulation times. Directional bremsstrahlung splitting (DBS) was used to increase the number of bremsstrahlung photons produced per bremsstrahlung event and the statistical weight of each photon is reduced accordingly. Following previously published work, the bremsstrahlung splitting number was set to 2000 [2, 89]. This means that when a bremsstrahlung event occurs, instead of generating a single bremsstrahlung photon, 2000 photons are created with weight 1/2000. Furthermore, if the produced bremsstrahlung photons are not directed into the user-specified field, Russian roulette is performed on those photons with survival probability 1/2000. This methodology allows for the production of a large amount of bremsstrahlung photons in the field of interested while not wasting computing time tracking photons that will be attenuated by the collimation system. The DBS radius was set to be 10 cm at a distance of 100 cm from the source to encompass the entire field and to ensure that ample scatter from the collimation system was included.

The code generates a phase space file which stores the position, energy and direction of each particle that crosses a plane below the filtration. This phase space file acts as a source for other EGSnrc codes. The filtration can be switched out in the beam model to produce a new phase space file for each filter combination investigated. Subsequent simulations and measurements were performed to benchmark the beam model which were made at maximum tube potentials of 320 kVp and 500 kVp. A readily available filter combination of 2.36 mm Cu + 1.96 mm Al was added to harden the beam to be representative of the standard beams being developed.

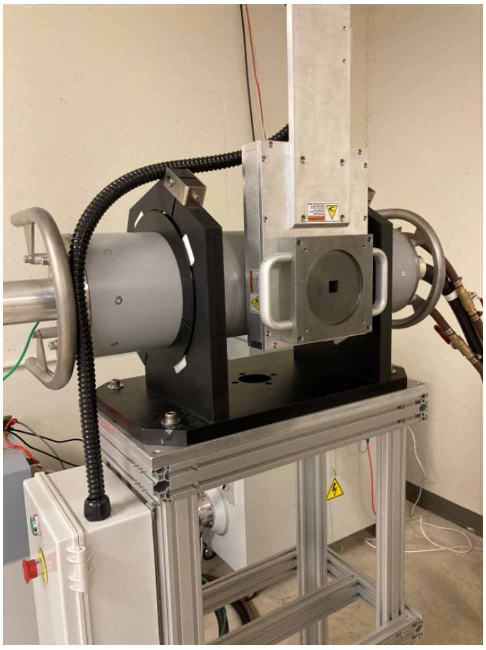

Figure 5.1: The NDI-451Be x-ray tube at the UWMRRC. The detachable collimator produces a 10x10 cm^2 field at 1 m from the focal spot.

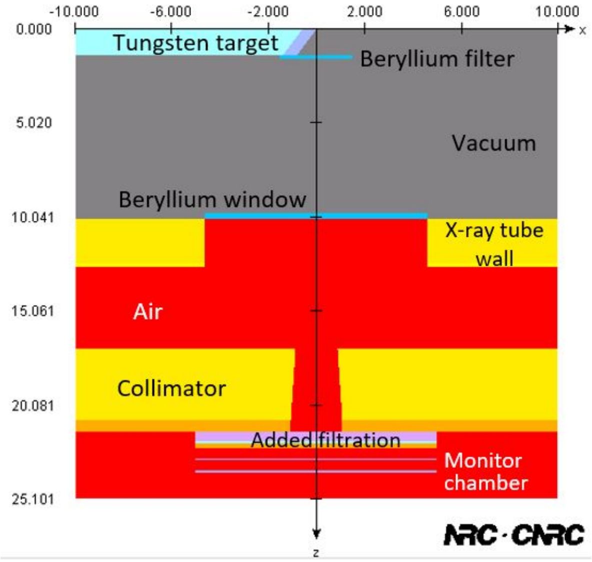

Figure 5.2: BEAMnrc rendering of the NDI-451Be x-ray tube and housing at the UWMRRC.

5.1.1 PDD simulations and benchmarking measurements

The first way the x-ray irradiator beam model was benchmarked was with depth profile measurements. The egs_chamber user code [85] simulates ionization chambers and was used to simulate an Exradin A1SL ionization chamber at various depths in a water tank to compare to depth profile measurements. This water tank was developed by Dr. Michael Lawless to measure depth profiles of horizontal-facing x-ray irradiators [2]. The Monte Carlo model of this water tank and the A1SL were validated as part of this work by Lawless et al. and a rendering of the ionization chamber in the water tank is shown in Figure 5.3. It was shown that the A1SL does not exhibit depth-dependent response changes in the kilovoltage energy range [90]. To increase efficiency of the simulations, range-based Russian roulette and photon cross-section enhancement variance reduction techniques were implemented [91]. In range-based Russian roulette, the user specifies a cavity region with the geometry. The residual range of each electron is calculated in the medium of interest and if it is determined that the electron cannot reach the cavity region, Russian roulette is played with survival probability $1/N_r$ where N_r is a user-specified value. This serves to terminate histories of electrons that would otherwise not contribute to dose in the volume of interest. Photon cross-section enhancement allows for the user to specify which regions will use an enhanced cross sections. A factor is assigned to each region chosen by the user which increases the generation of electrons along the path of photons in these regions. These techniques greatly increase the efficiency of dose calculations in low-density regions, such as the collecting volume of the ionization chamber, and in regions with relatively few photon interactions, such as deep in the water in the kilovoltage energy range. In these simulations a range based Russian roulette was implemented with a rejection value of 32 in air and a cross section enhancement factor of 16 was implemented in regions inside and surround the collecting volume based on the literature [2].

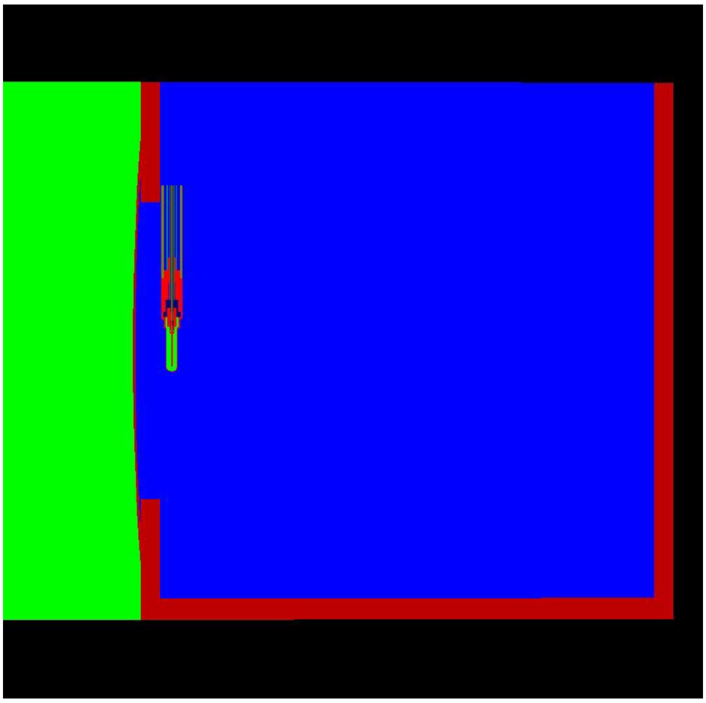

Figure 5.3: Rendering of the A1SL ionization chamber inside the thin-window water tank developed by Dr. Michael Lawless [2].

The measured and simulated A1SL depth profiles for the NDI-451Be x-ray tube are shown in Figure 5.4. The measured ionization curves as a function of depth were normalized to a depth of 3 cm in order to create a percent depth ionization (PDD) curve. The dose to the collecting volume of the A1SL ionization chamber obtained from the egs_chamber simulations was also normalized to a depth of 3 cm and compared to the measured PDD curve. All simulated PDD points were within 2% of the corresponding measured PDD point except the most shallow depth due to its steep dose gradient which was within 3%.

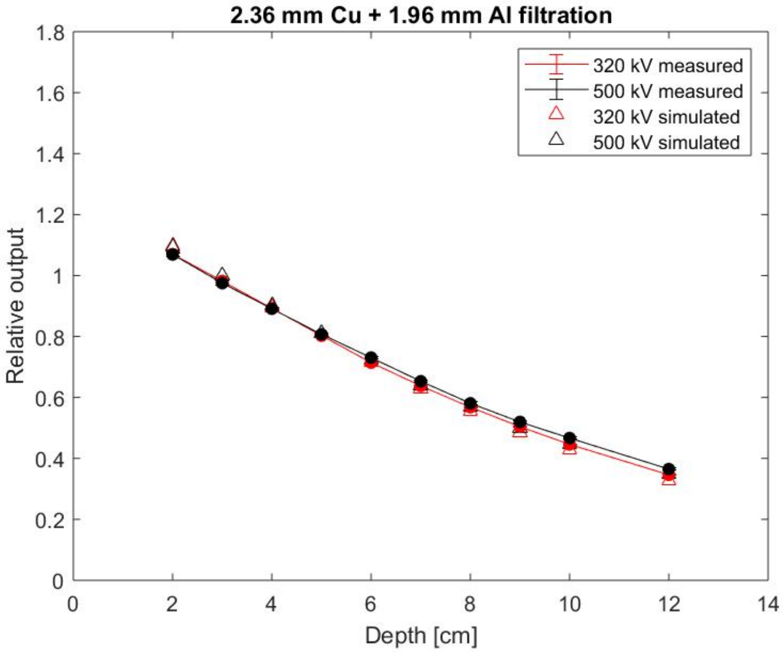

Figure 5.4: Measured and simulated depth profiles for the two energy benchmarking beams of the NDI-451Be x-ray tube with 1.96 mm Al + 2.36 mm Cu filtration.

5.1.2 Spectra simulations and benchmark measurements

The FLURZnrc user code [85] simulates photon and electron spectra in simple geometries and was used to compare the measured and simulated HVL's of each x-ray tube. The spectra were tallied in a cylinder of air with a radius and thickness of 1 cm at a distance of 100 cm from the focal spot. The air kerma for each spectrum can be calculated by

$$K_{air} = \sum_{i=1}^{N} E_i \phi_i \left(\frac{\mu_{en}}{\rho} \right)_i , \tag{5.1}$$

where N is the number of energy bins, E_i is the mean energy of bin i, ϕ_i is the fluence in energy bin i, and $(\mu_{en}/\rho)_i$ is the mass energy absorption coefficient of air at the mean energy of bin i.

For the NDI-451Be x-ray tube, HVL measurements were taken for beams with 1.96 mm Al + 2.36 mm Cu filtration and maximum tube potentials of 320 kVp and 500 kVp. Measurements were taken with an Exradin A12 ionization chamber with a NIST-traceable calibration in Co-60. The added amount of copper was iterated until the HVL was found and refined through a semilogarithmic interpolation [92]. This process was repeated for the QVL. A phase space file was then created with just the added filtration and another phase space file was created with the measured HVL amount of copper added. A third phase space file was created with the measured QVL amount of copper added. The spectra were simulated in the FLURZnrc user code and the air kerma for each beam was calculated by Equation 5.1. The HVL's of the measured and simulated beams match when the air kerma ratio of beams with and without the added filtration is equal to 0.5. The QVL's match when the air kerma ratio with and without the added filtration is equal to 0.25.

From the simulated spectra obtained from the FLURZnrc simulations, the measured HVL and QVL were validated. The actual inherent filtration was found to match the manufacturer specified values as the HVL and QVL of the 320 kV beam matched without any adjustments made. It was found that the tube potential is unstable at its maximum, so the actual maximum tube potential is about 497 kV. When developing the higher energy beams, the maximum tube potential is set at 495 kV to avoid this instability. The comparisons of the air kerma ratios are shown in Table 5.1. These values show agreement within 0.8% as the air kerma fraction should be 0.5 for the HVL and 0.25 for the QVL.

Table 5.1: Validation that the beam model produces the correct air kerma ratio for the measured HVL and QVL for the benchmarking beams of the NDI-451Be x-ray tube. These measurements were taken with a maximum tube potential of 500 kVp and 320 kVp with the same filter as designated.

	Max. tube potential: 500 kV 1.96 mm Al + 2.36 mm Cu filtration	Max. tube potential: 320 kV 1.96 mm Al + 2.36 mm Cu filtration
Measured HVL (mm Cu)	4.803	3.540
Simulated air kerma ratio with measured HVL	0.500	0.499
Measured QVL (mm Cu)	10.582	7.905
Simulated air kerma ratio with measured QVL	0.250	0.248

5.2 Filter development

5.2.1 Matching HVL through simulations

The Varex NDI-451Be x-ray tube at the UWMRRC was used as the source for the beams being matched to the F1 and F2 beams in the XRad320 and the SARRP therapeutic beam. Matched beams will be denoted as MatchF1, MatchF2 and MatchSARRP. The tube voltage and mA were set to be the same as the radiobiology irradiators: 320 kV and 12.5 mA for the XRad320 and 220 kV and 13 mA for the SARRP. The starting point for the filtration optimization was the added filtration for the radiobiology irradiators: 0.15 mm Cu for the SARRP beam, 2 mm Al for the XRad320 F1 beam, and 1.5 mm Al + 0.25 mm Cu + 0.75 mm Sn for the XRad320 F2 beam. This amount of filtration was added to the NDI-451Be x-ray tube beam model and the spectra simulated. The spectra were then simulated again with the amount of copper equal to the HVL for each beam added. The HVL values reported in Table 5.2 are the measured values from Dr.

Viscariello's thesis work [93]. The air kerma with just the added filtration and with the added HVL of copper was calculated with Equation 5.1. The ratio of the air kerma with the HVL filtration to without the HVL filtration was then determined. If the ratio was between 0.485 and 0.515, as recommended by the IAEA TRS No. 457 [94], then the added filtration was considered matched. If not, the added filtration was increased or reduced accordingly. The amount of added filtration for each beam to achieve the correct HVL was then validated with HVL measurements with the medium-energy FAC.

Table 5.2 shows the final beam parameters for the matched x-ray beams developed for the SARRP and XRad320. The added filtration column indicates the final added filtration for the matched beams after the iterative process was complete. The amount of added filtration for each beam is minimally higher than the added filtration of the radiobiology irradiators.

Table 5.2: Final beam parameters of the matched radiobiology standard x-ray beams with simulated and measured air kerma ratio results. Both simulated and measured air kerma ratios are within 3% of 0.5 indicating these matched beams have the correct HVL.

Matched beam	Added filtration	HVL (mm Cu)	Simulated air kerma ratio	Measured air kerma ratio
MatchF1	3.484 mm Al	0.82	0.504	0.503
MatchF2	0.772 mm Sn + 0.509 mm Cu + 1.524 mm Al	3.93	0.492	0.502
Match-SARRP	0.21 mm Cu	0.71	0.504	0.506

5.2.2 Spectral comparisons

As a secondary check, the simulated spectra of the matched beams and the original radiobiology beams were compared. The spectra of the radiobiology beams were regenerated from the beam models developed as part of Dr. Viscariello's thesis work [93].

Figures 5.5 and 5.6 shows the simulated spectra comparison of the XRad320 and the matched x-ray beams and Figure 5.7 shows the same for the SARRP. These figures qualitatively show that matching the x-ray beams by HVL created relatively matched spectra. They also show the M-series x-ray beams that are commonly used for calibration of detectors used in radiobiology irradiators. The M-series spectra are the measured spectra by Dr. Moga [81]. For a quantitative comparison, the average energy of each spectrum was calculated by

$$E_{ave} = \sum_{i=1}^{N} = E_i \frac{\phi_i}{\phi_{total}}, \tag{5.2}$$

where N is the number of energy bins, E_i is the mean energy of bin i, ϕ_i is the fluence in energy bin i, and ϕ_{total} is the total fluence summed over all bins. Table 5.3 shows that the average energy of the simulated spectrum of each radiobiology x-ray beam agrees to the simulated spectrum of its matched x-ray beam within 2.4%. Figures 5.5 - 5.7 show that the standard M-series x-ray beams do not approximate the radiobiology beams well. The poor approximation is especially true for the XRad320 F2 beam which includes a tin filter that hardens the beam well beyond the shape of the M-series beams.

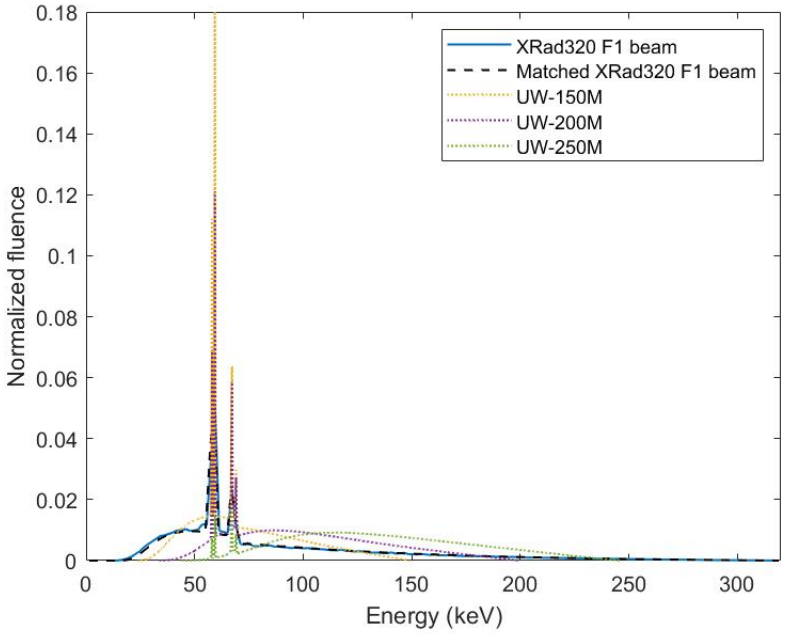

Figure 5.5: XRad320 (solid) and matched beams on the NDI-451Be (dashed) spectra for the F1 beam compared to relevant M-series beams (dotted). Spectra are normalized to give the same integral area under the curve.

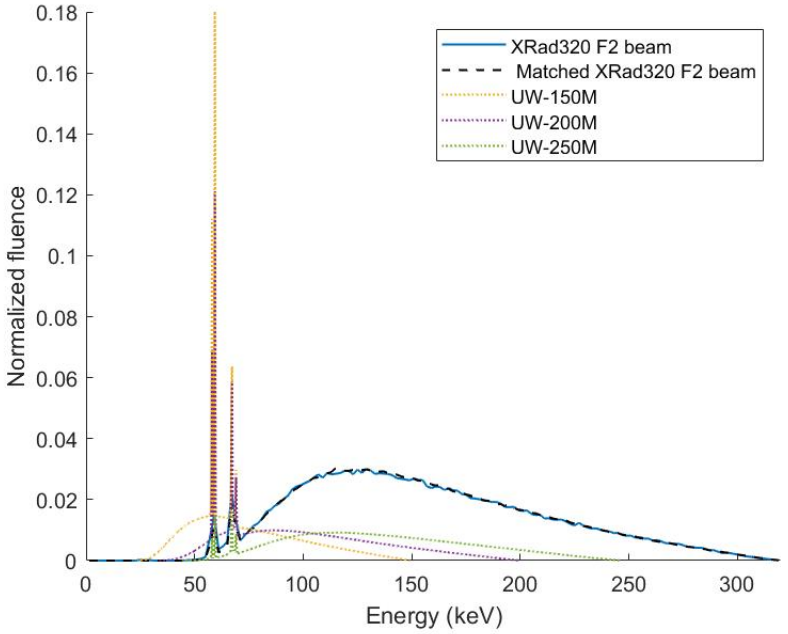

Figure 5.6: XRad320 (solid) and matched beams on the NDI-451Be (dashed) spectra for the F2 beam compared to relevant M-series beams (dotted). Spectra are normalized to give the same integral area under the curve.

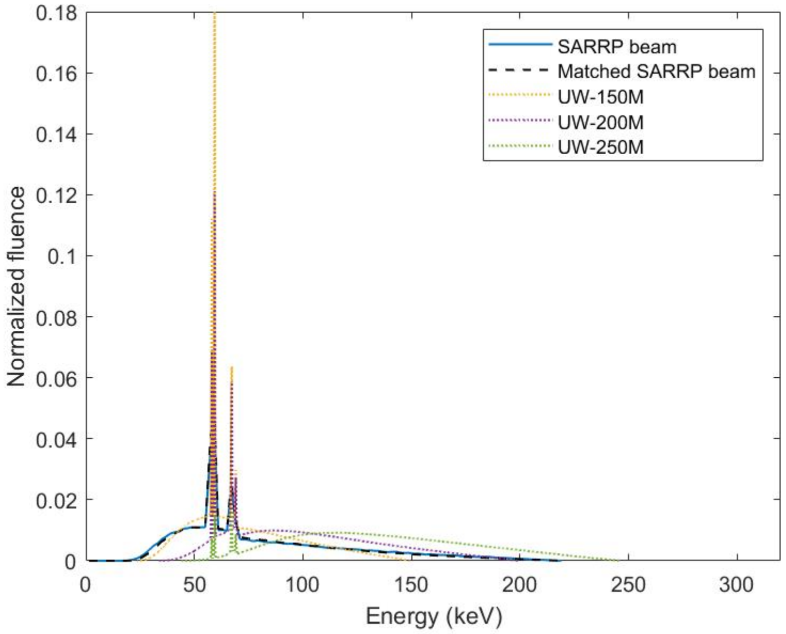

Figure 5.7: SARRP (solid) and matched beams on the NDI-451Be (dashed) compared to relevant M-series beams (dotted). Spectra are normalized to give the same integral area under the curve.

Table 5.3: Comparison of the average energy of the simulated spectra of the radiobiology irradiators and the matched x-ray beams.

Beam	Simulated spectrum average energy (keV)	Matched beam simulated spectrum average energy (keV)	Percent difference (%)
XRad320 F1	86.9	89.0	2.4
XRad320 F2	156	156	0
SARRP	81.5	80.1	1.7

The use of these matched beams for calibration of these irradiators would lead to dose determination that is more accurate due to the calibration being more representative of the energy distribution of the x-rays in these irradiators. The NDI-451Be x-ray tube required more added filtration than the radiobiology irradiators, but the amount added was minimal. This is due to the difference in inherent Be filtration of the NDI-451Be x-ray tube and the radiobiology irradiators.

5.3 Ionization chamber calibration comparison

An Exradin A12 Farmer-type ionization chamber was calibrated in the matched x-ray beams to compare the air kerma calibration coefficients, N_k, to the M-series x-ray beams that are commonly used to calibrate dosimetry equipment used in radiobiology irradiators. The air kerma calibration coefficient is calculated by

$$N_k = \frac{K_{air}^Q}{M_{raw} P_{TP} P_{pol} P_{elec} P_{ion}}, \tag{5.3}$$

where K_{air}^Q is the air kerma (in Gy) in the specific beam quality, Q, at the point of measurement of the ion chamber in the absence of the chamber. It is measured with an absolute dosimeter, in this case the medium-energy FAC. The other values are M_{raw} which is the raw ionization chamber readings in Coulombs, P_{TP} is the temperature-pressure correction, P_{pol} corrects for any polarity effects, P_{elec} is the electrometer calibration factor, and P_{ion} corrects for incomplete ion collection efficiency [69]. The air kerma calibration coefficients for the M-series beams were acquired by submitting the A12 ionization chamber through the UWADCL service to be calibrated in the same way as any user's chamber would be. It is the user's choice in which x-ray beams their equipment will be calibrated. For example, an ionization chamber used in the SARRP may be calibrated in the UW-200M beam or the UW-250M beam as the maximum energy, 220 kV, lies between the two. The chamber could also be calibrated in both and the calibration coefficient interpolated between the two. Alternatively, it could be calibrated in the UW-150M beam as the HVL, 0.71 mm Cu, most closely matches the UW-150M HVL, 0.66 mm Cu. Therefore, the air kerma calibration coefficients of the matched beams will not be compared to a single beam but all three relevant beams: UW-150M, UW-200M, and UW-250M.

Table 5.4 shows the air kerma calibration coefficients of the A12 ionization chamber in the matched beams compared to the relevant M-series beams. The N_k values for the matched x-ray beams are a few percent higher than the N_k values for the M-series beams. The largest difference occurs for the MatchF2 beam because of the introduction of the tin filter which hardens the beam to a significantly different shape than the M-series beams as illustrated in Figure 5.6. The difference in the N_k values is greater than the uncertainty in the air kerma measurement taken with the medium-energy FAC and the uncertainty in the UWADCL calibration indicating a significant difference between these calibration coefficients.

Table 5.4: Comparison of the air kerma calibration coefficients of an Exradin A12 ionization chamber in the matched radiobiology x-ray beams and relevant x-ray beams.

Beam	A12 N_k value (Gy/C)	Average percent difference from M-series (%)
MatchF1	4.566×10^7	3.19
MatchF2	4.707×10^7	6.37
MatchSARRP	4.549×10^7	2.81
UW-150M	4.408×10^7	–
UW-200M	4.422×10^7	–
UW-250M	4.445×10^7	–

Chapter 6

High energy x-ray beams

6.1 High energy x-ray beam

6.1.1 Filter development

The NDI-451Be x-ray tube was used a source to develop a high energy x-ray beam that could be used as a surrogate for Cs-137. Due to the limitations of the maximum energy of the x-ray tube it is not possible to exactly match the energy and HVL of Cs-137 but it is also not necessary. The goal of this x-ray beam was for it to be at a higher energy than what is currently available. A filter that acts as a high-pass filter was needed to harden the beam to a high average energy. The amount of added filtration needed is arbitrary, but a high average energy is desired without over-filtering and reducing the output to a level that gives a very low signal. A sufficient signal is needed for use with ionization chambers, TLD's and other detectors that require a high signal to operate.

The inspiration for the high-energy x-ray beam filter was taken from Thoraeus filters as discussed in Chapter 2. The standard Thoraeus filters are shown in Table 6.1, which are used for x-rays in the orthovoltage range [3]. The maximum energy of the high-energy beam being developed is 495 keV, so the filter must be considerably thicker than the standard Thoraeus filters.

Table 6.1: Thoraeus filters used with orthovoltage x-rays [3]

Filter	Composition
Thoraeus I	0.2 mm Sn + 0.25 mm Cu + 1 mm Al
Thoraeus II	0.4 mm Sn + 0.25 mm Cu + 1 mm Al
Thoraeus III	0.6 mm Sn + 0.25 mm Cu + 1 mm Al

The beam model developed in Chapter 5 was used to investigate how the filtration would affect the spectra. First, the spectra of the NDI-451Be x-ray tube with the Thoraeus III filter was modeled, and it was found that the amount of tin was not sufficient in completely reducing the tungsten K lines. At least 2 mm of tin would be needed to eradicate those lines and the amount of copper and aluminum was also increased. Figure 6.1 shows how the K lines are reduced between 1 and 2 mm of tin filtration. The average energy of the spectra of each filter combination was calculated with Equation 5.2. As the average energy increases, the effectiveness of the filtration decreases as the lower energy photons that primarily interact by the photoelectric effect are filtered out and Compton scattering becomes more prevalent. The average energy started to level off at the higher filtration amounts, and it was found that adding 1.5 mm of copper only added around 4 keV to the average energy while adding 1.5 mm of tin added around 10 keV. The filter needed to be kept thin enough to fit in the filter holder on the x-ray tube, so increasing the tin was prioritized. With increasing tin, the spectrum becomes more monoenergetic and has a higher average energy which is ideal for an x-ray beam being used to approximate Cs-137.

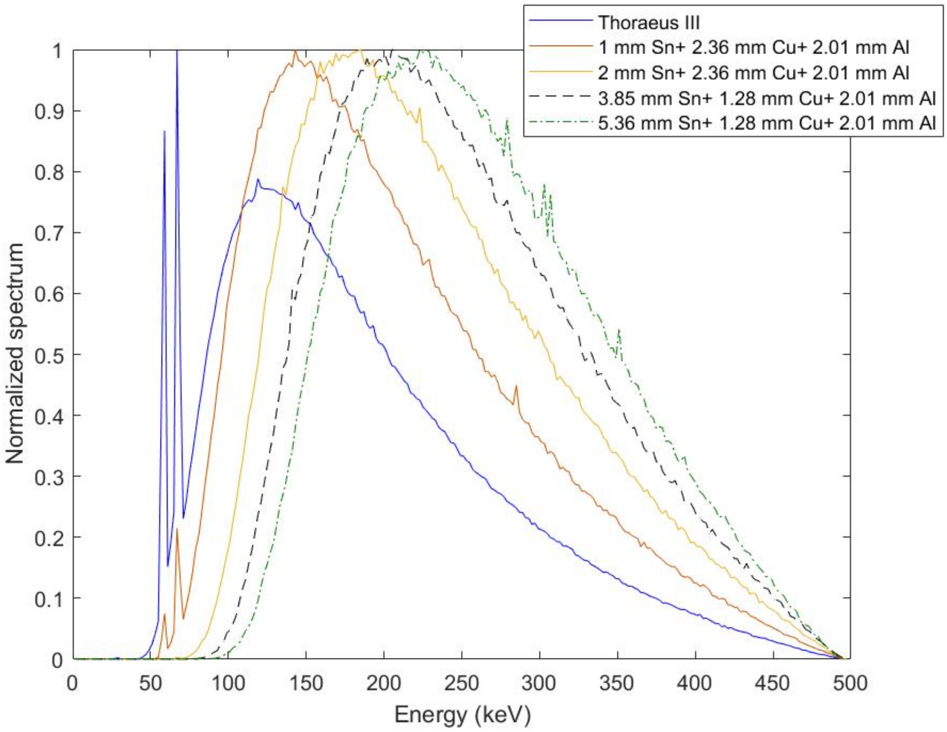

Figure 6.1: Simulated spectra of multiple iterations of the high-energy beam filter. The K lines of the tungsten target disappear between 1 mm and 2 mm of tin filtration.

6.1.2 Beam quality and intensity measurements

Air kerma measurements were taken with different combinations of tin, copper and aluminum to determine the filtration that achieves a high average energy without too much of a reduction in the beam intensity. The measurements were taken with the known-volume ionization chambers at 1 m from the focal spot in a 10 x 10 cm^2 field and their measurements were averaged. The spectral simulations provided the energy distribution used to calculate the known-volume correction factors. The buildup caps were included due to the high energy of the spectra. The goal of this investigation was to keep the air kerma rate higher than the most highly filtered NIST-matched x-ray beam, UW-250M, which has an air kerma rate of 1.64 mGy/s. The mA was maximized at the maximum energy of 495 kV, which is 9 mA. With several iterations, it was found that the beam intensity is not an issue with these combination filters as shown in Table 6.2. Even with the thickest filter, the air kerma rate is above 1.64 mGy/s.

Table 6.2: Air kerma rate at 1 m for various high energy beam filter combinations

Composition	Air kerma rate (mGy/s)
1.90 mm Sn + 1.28 mm Cu + 2.01 mm Al	5.117
3.85 mm Sn + 1.28 mm Cu + 2.01 mm Al	3.539
3.85 mm Sn + 2.55 mm Cu + 2.01 mm Al	3.064
5.36 mm Sn + 1.28 mm Cu + 2.01 mm Al	2.742

The air kerma rate of the maximum filter thickness investigated was 1.1 mGy/s higher than that of the UW-250M beam. Therefore, this filter was chosen as the filter combination used for developing this Cs-137 surrogate beam. Table 6.3 shows the final parameters of this beam. Similar to the benchmarking of the rad bio beams, the HVL and QVL were measured to compare to the simulated air kerma ratios. The known-volume chambers were used to measure for these HVL and QVL measurements. The results agree within the IAEA recommended 3% agreement of 0.5 and 0.25, respectively, as shown in Table 6.4 [94].

Table 6.3: Final beam parameters for the high energy beam

Beam code	Filter composition (mm)	HVL 1 (mm Cu)	HVL 2 (mm Cu)	HC (%)	1 m A_k rate (mGy/s)	mA
UW495-H	5.36 Sn + 1.28 Cu + 2.01 Al	6.64	6.86	97	2.742	9

Table 6.4: Air kerma ratios to benchmark the high energy beam spectrum

	Measured (mm Cu)	Simulated air kerma fraction
HVL	6.635	0.500
QVL	13.499	0.248

6.2 Ir-192 brachytherapy source x-ray beam

6.2.1 Filter development

The fluence weighted average energy of Ir-192 brachytherapy sources, neglecting the two strong L x-ray lines that are attenuated by the source encapsulation, is 397 keV. From the Cs-137 surrogate beam study, it became apparent that tin as the highest density filter would not be sufficient to increase the average energy of the x-ray beam enough to match this energy. Tungsten, tantalum and lead filters were subsequently investigated. All three filters produce characteristic x-rays between 57 and 85 keV, so a combination filter of tin, copper and aluminum would also be required with these filters to reduce those K lines. All filters discussed below include a combination of 5.36 mm Sn + 1.28 mm Cu + 2.01 mm Al along with the high density filter.

The beam model developed in Chapter 5 was used to calculate the amount of high density filter that would be needed to achieve a fluence weighted average energy of approximately 397 keV. The average energy was calculated by taking a weighted average of the spectra produced by the FLURZnrc user code. Figures 6.2 - 6.4 show how the spectrum is affected by various thicknesses of the high density filter. Table 6.5 shows the optimized filtration thicknesses and the corresponding average energy.

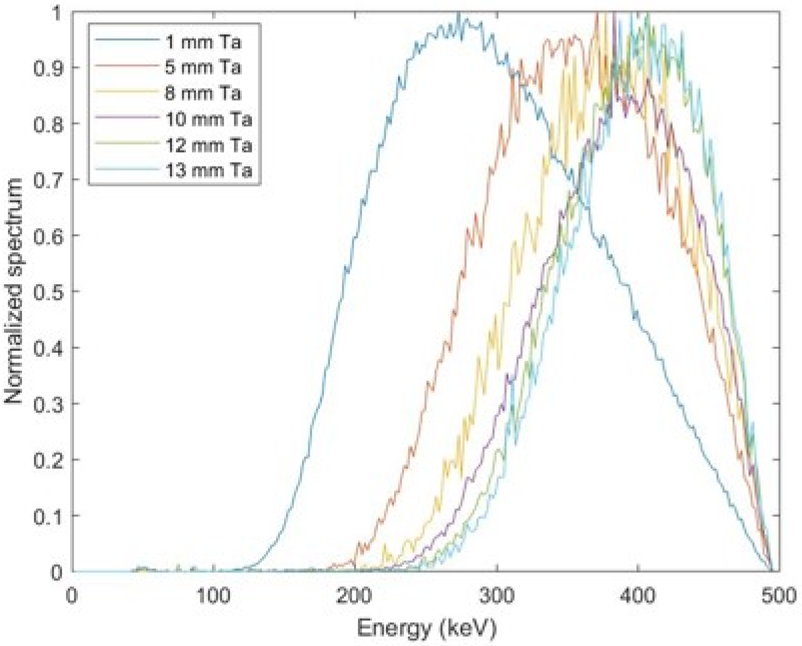

Figure 6.2: Simulated spectra of multiple iterations of the beam with various thicknesses of tantalum.

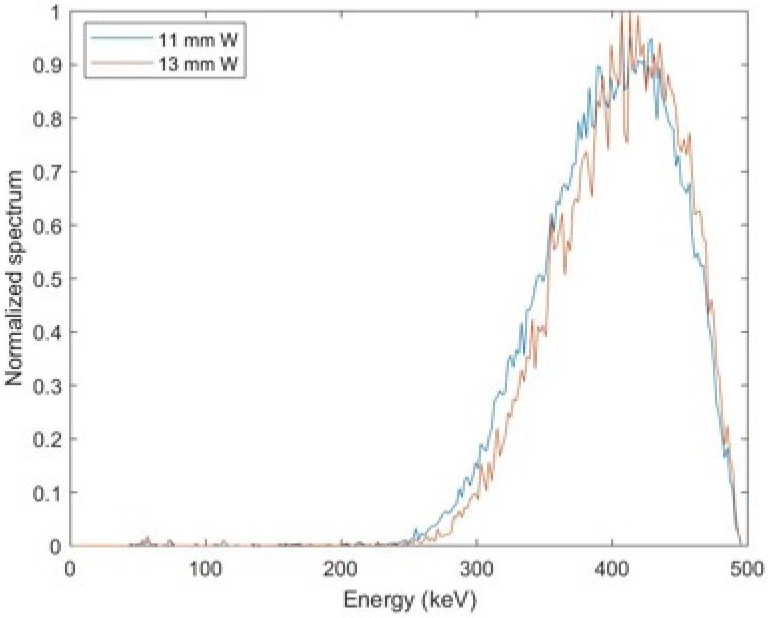

Figure 6.3: Simulated spectra of multiple iterations of the beam with various thicknesses of tungsten.

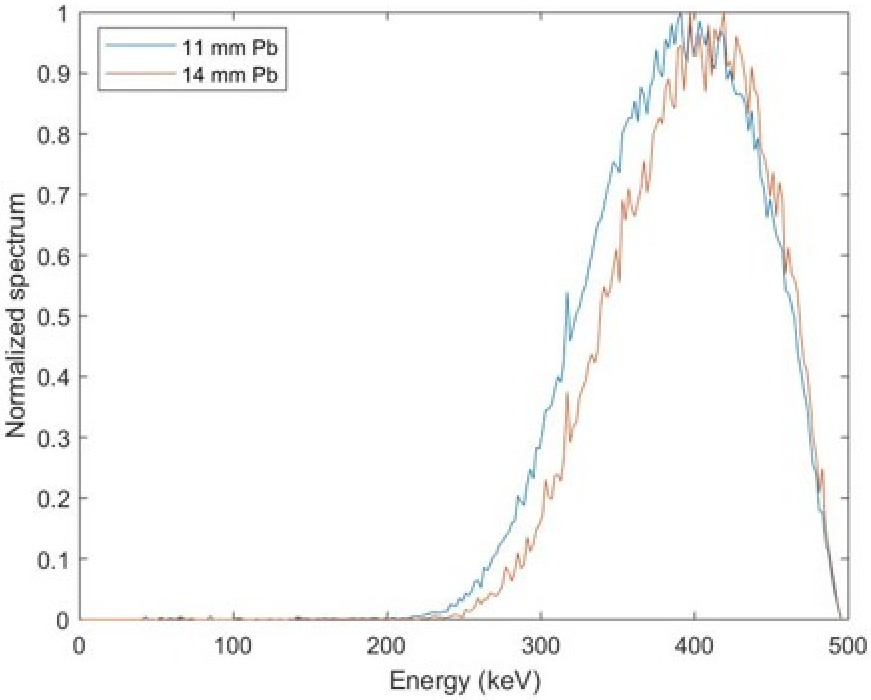

Figure 6.4: Simulated spectra of multiple iterations of the beam with various thicknesses of lead.

Table 6.5: Optimized filter thicknesses and corresponding average energy

Material	Thickness (mm)	Average energy (keV)
Tantalum	13	396.7
Tungsten	11	397.2
Lead	14	396.3

All three filter combinations require between 1 and 1.5 cm of the high density filter. There is not a clearly obvious choice in which filter material to use as there are advantages and disadvantages to each. Tantalum is less brittle than tungsten but is considerably more expensive. Lead poses a health concern that would require encasing the filter in another metal and/or painting. Lead is also a softer metal which is not ideal for a filter that is handled often. There are no reasons associated with how these filters affect the spectra that make one filter better than the others.

6.2.2 Air kerma measurements

Air kerma measurements were performed with the combination filter of lead, tin, copper, and aluminum. Since there was no clear advantage of one filtration material over another, lead was chosen as it was readily available. Due to limitations in machining tolerances, the actual amount of lead used was 13.2 mm which produces an average energy of 393.6 keV. The measurements were taken with the known-volume ionization chambers at 1 m from the focal spot in a 10 x 10 cm^2 field. The spectral simulations provided the energy distribution used to calculate the known-volume correction factors. The buildup caps were included due to the high energy of the spectra. The mA was maximized at the maximum energy of 495 kV, which is 9 mA. The air kerma measurements were compared to measurements taken with an Exradin A12 ionization chamber with an interpolated calibration coefficient for 393.6 keV using NIST-traceable UW-250M and Cs-137 calibration coefficients. Table 6.6 shows this comparison and it shows how the known-volume chamber measurement agrees well with the current measurement technique, but the known-volume chambers offer the advantage of direct measurement.

Table 6.6: Air kerma rate at 1 m for the Ir-192 brachytherapy source average energy matching beam measured by the known-volume chambers and a calibrated ionization chamber. Standard deviations are listed in parenthesis.

Ionization chamber	Air kerma rate (mGy/s)	Average percent difference (%)
Chamber 1 S/N: XR191680	0.0680(0.0008)	–
Chamber 2 S/N: 256	0.0679(0.0013)	–
Exradin A12	0.0676(0.0012)	0.593

Chapter 7

Conclusions and future work

7.1 Conclusions

In this work, two types of absolute dosimeters were developed to investigate establishing standard x-ray beams. The establishment of the FAC as a primary measurement tool reduced the uncertainty on the air kerma of x-ray beams as it negated the need for energy corrections of other dosimeters or an interpolated calibration on an ionization chamber. Outside of primary standards laboratories, a FAC that can measure x-rays in the kilovoltage range did not exist until this work. The medium-energy FAC can only measure x-rays up to 320 keV as it would become prohibitively large if designed to measure higher energy x-rays. Therefore, known-volume spherical ionization chambers were established using μCT methods to measure x-rays up to 500 keV as well as Cs-137 and Co-60. Typical known-volume chambers exist only in primary standards laboratory as they require ultra-precise machining methods. This work showed that it is possible to establish a known-volume chamber with a commercial ionization chamber and a μCT scanner.

This work has also produced dosimetric models of the NDI-451Be x-ray tube at the UWMRRC so that the x-ray beams could be investigated with Monte Carlo. Validation measurements were performed with a well-characterized water tank and ionization chambers. This validation of depth profiles and spectral comparisons produced Monte Carlo models that could be used with confidence for establishing x-ray beams. Standard x-ray beams were created to match the XRad320 and SARRP radiobiology irradiator x-ray beams by iterating the amount of added filtration needed on the NDI-451Be x-ray tube until the HVL matched the corresponding HVL of the radiobiology beam, as validated by FAC HVL measurements. The air kerma fraction of each of these beams, both measured and simulated, fell within the 0.485-0.515 range recommended by IAEA TRS-457 [94]. The creation of the Monte Carlo beam models allowed for the direct comparison of simulated spectra of the radiobiology irradiators and matched x-ray beams instead of a comparison of HVL alone. These spectra showed that the matched beam spectra sufficiently match the radiobiology irradiator spectra as the average energies agreed within 2.4%.

It was shown that standard x-ray beams can be established for higher energy x-rays with the use of higher density filters and an industrial x-ray tube like the NDI-451Be tube. First, a high energy beam was created with inspiration from Thoraeus filters. These combination tin, copper and aluminum filters created a a beam with a maxmimum energy of 495 keV and an average energy of 265 keV as determined by the Monte Carlo beam models. The air kerma and HVL of this beam was validated with measurement by the known-volume ionization chambers. This accomplishes the goal of a high energy beam that lies in the gap between the highest energy beam available at the UWMRRC, UW-250M, and Cs-137, but still does not sufficiently increase the average energy for certain applications. One of those applications is an x-ray beam for an ionization chamber to be calibrated in to measure air kerma strength from Ir-192 brachytherapy sources with an average energy of 397 keV. A higher density material than tin is needed, so in combination with tin, copper, and aluminum, about 14 mm lead was determined to match Ir-192 average energy through optimization performed with the Monte Carlo models. Air kerma measurements with the known-volume ionization chambers confirmed that this method is comparable to the calibration coefficient interpolation method, but with the advantage of direct measurement.

Overall, the work of this thesis emphasized the need for the introduction of new, higher energy standard x-ray beams as the current standard beams are insufficient for many applications. To create standard beams, absolute and primary dosimeters are required and this work established those tools for the standard beams created for this work and for future standard x-ray beams.

7.2 Recommendations for future work

7.2.1 Spectral measurements to benchmark NDI-451Be x-ray tube beam model

One of the highest sources of uncertainty for both the FAC and known-volume chambers are the energy dependent correction factors due to the fact that the spectra are simulated rather than measured for each beam besides the M-series beams. As shown in Dr. Moga's thesis work, x-ray spectral measurements are very involved and were outside the scope of this thesis [81]. If spectral measurements could be taken to at least benchmark the spectra simulated by the NDI-451Be x-ray tube beam model, it would aid in reducing the uncertainty on both absolute dosimeters.

7.2.2 More rigorous surface determination for known-volume ionization chambers

One of the highest sources of uncertainty on the known-volume ionization chambers is the uncertainty on the surface determination algorithm. The ISO50 method for surface determination is a relatively simple algorithm and there may be room for improvement in image processing and a more rigorous surface determination algorithm. There is software that performs the image processing, ISO50 surface determination and contouring automatically, which may also aid in reducing the standard deviation compared to the Matlab script developed for this thesis. At the time of this thesis, this software was unavailable due to the COVID-19 pandemic restrictions, but may be worth exploring in the future. If this portion of the uncertainty could be reduced, the overall uncertainty may be more on the order of magnitude of conventional known-volume ionization chambers.

7.2.3 Use of high-energy x-ray beam for survey meter calibration

The current process for calibrating survey meters is to place the survey meter at different distances from a Cs-137 source for various exposure rates to calibrate each scale on the meter. Due to a New York City law that requires the surveying of electronic brachytherapy sources, there is interest in calibrating survey meters in x-rays [95]. The main barrier to an x-ray calibration is that the exposure rate of x-ray irradiators is much too high for the sensitive meters. Even with the lowest mA setting and placing the survey meter far from the irradiator it is often still too high and does not allow for adjusting the exposure rate to calibrate multiple scales. The high density filters like tantalum, tungsten, or lead could help reduce the exposure rate to a sufficient level, but the filtration would need to be larger than the Ir-192 brachytherapy source matching beam investigated in this thesis.

To adjust the exposure rate to calibrate multiple scales the amount of filtration or mA would need to be adjusted which would affect the energy spectrum, so how that would affect calibration would need to be investigated as well.

7.2.4 Establish Ir-192 brachytherapy source standard x-ray beam

Further work needs to be done in establishing the Ir-192 brachytherapy source standard beam. Primarily, more precise machining could be utilized to achieve a filter with a thickness closer to the optimized thickness. Once the filter is established, it should be used to calibrate the standard A3 ionization chamber used for calibrating Ir-192 brachytherapy sources in the 7-D apparatus to compare to the current interpolated calibration factor method more directly. A full uncertainty investigation should be completed to explore if this method would have a comparable or a lower uncertainty than the interpolated correction factor method. It's also possible that the known-volume ionization chambers could be used in place of the calibrated ionization chamber, but the uncertainty would need to be reduced via the methods discussed above before that would be a viable option.

7.3 Closing remarks

Accurate dose measurements are essential for improving and maintaining reproducibility across institutions and experiments. As the field moves toward using x-rays in the kilovoltage and higher energy range more routinely, dosimetry that is traceable to primary standards is paramount to maintaining pace with these movements. This work sought to advance kilovoltage dosimetry practices for radiobiology by establishing standard x-rays beams in which dosimeters can be calibrated against. It also investigated the establishment of higher energy standard x-ray beams in an energy range that lacks standard beams. Future investigations will be able to use the methods in this work to further study the the establishment of standard x-ray beams in this energy range.

Bibliography

[1] Larry A. DeWerd et al. Ionization Chamber Instrumentation. https://www.aapm.org/meetings/09SS/documents/06DeWard-IonChambersInstrumentation.pdf.

[2] Lawless M et al. Monte Carlo and ^{60}Co-based kilovoltage x-ray dosimetry methods. *Med. Phys.*, 45:5564–5576, 2018.

[3] Faiz M. Khan. *The Physics of Radiation Therapy.* Lippincott Williams & Wilkins, 4th edition, 2010.

[4] Desrosiers M et al. The Importance of Dosimetry Standardization in Radiobiology. *J Res Natl Inst Stand Technol*, 118:403–418, 2013.

[5] Emily Draeger et al. A Dose of Reality: How 20 Years of Incomplete Physics and Dosimetry Reporting in Radiobiology Studies May Have Contributed to the Reproducibility Crisis. *Int J Radiation Oncol Biol Phys*, pages 1–10, 2019.

[6] Alexander Kamb. What's wrong with our cancer models? *Nat Rev Drug Discov*, 4: 161–165, 2005.

[7] DeWerd L and Kunugi K. Accurate Dosimetry for Radiobiology. *Int. J. Radiat. Oncol. Biol. Phys.*, 111(5):e75–e81, 2021.

[8] C. M. Ma et al. Aapm protocol for 40 - 300 kv x-ray beam dosimetry in radiotherapy and radiobiology. *Med. Phys.*, 28(6):868–893, 2001.

[9] Steven J. Goetsch et al. Calibration of ^{192}Ir high-dose-rate afterloading systems. *Med. Phys.*, 18(3):462–467, 1991.

[10] Brian E. Rasmussen et al. Comparison of air-kerma strength determinations for HDR ^{192}Ir sources. *Med. Phys.*, 38(12):6721–6729, 2011.

[11] Strengthening radiological security through alternative technology in California. `https://www.energy.gov/nnsa/articles/strengthening-radiological-security-through-alternative-technology`. Accessed: July 2019.

[12] Charles A. Potter et al. Radiobioligcal Studies Using Gamma and X Rays. Technical report, Sandia National Laboratories, February 2013.

[13] Brian Smith et al. University of California Systemwide Radioactive Source Replacement Workgroup Recommendations, April 2018.

[14] Harold Elford Johns and John Robert Cunningham. *The Physics of Radiology*. Charles C Thomas, 4th edition, 1983. ISBN 0398046697.

[15] F. H. Attix. *Introduction to Radiological Physics and Radiation Dosimetry*. Wiley, 1986. ISBN 0471011460.

[16] Absorbed Dose Determination in Photon and Electron Beams. *IAEA Report No 277*, 1992.

[17] H. O. Wyckoff and F. H. Attix. Design of free-air ionization chambers. NBS Handbook 64, 1957.

[18] International Atomic Energy Agency. National and international standardization of radiation dosimetry. *Proc. Ser. STI/PUB/471*, 1 and 2, 1978.

[19] R. Thoraeus and H.O. Wyckoff. Calibration of the portable swedish free-air chamber equipment at the u.s. national bureau of standards. *Acta Radiol.*, 46(6):741–746, 1956.

[20] W. L. Chen et al. Improved free-air ionization chamber for the measurement of x-rays. *Metrologia*, 26(1):19–24, 1999.

[21] F. H. Attix. Electronic equilibrium in free-air chambers and a proposed new chamber design. NRL Report 5646, 1961.

[22] J. G. Coletti et al. Mammography exposure standard: Design and characterization of free-air ionization chamber. *Rev. Sci. Instrum.*, 66(3):2574–2577, 1995.

[23] New Detector Design Improves Gamma-Ray Measurements. https://www.nist.gov/news-events/news/2012/04/new-detector-design-improves-gamma-ray-measurements, 2012.

[24] Andrea L. McNiven et al. Ionization chamber volume determination and quality assurance using micro-ct imaging. *Phys. Med. Biol.*, 53(18):5029–5043, 2008.

[25] C K Ross. Comments on 'ionization chamber volume determination and quality assurance using micro-ct imaging'. *Phys. Med. Biol.*, 54(6):L23–L27, 2009.

[26] D.W.O. Rogers and Iwan Kawrakow. Monte Carlo calculated correction factors for primary standards of air kerma. *Med. Phys.*, 30(4):521–532, 2003.

[27] Micewicz ED et al. The aftermath of surviving acute radiation hematopoietic syndrome and its mitigation. *Radiat Res*, 191(4):323–334, 2019.

[28] Soloviev AI and Kizub IV. Mechanisms of vascular dysfunction evoked by ionizing radiation and possible targets for its pharmacological correction. *Biochemical Pharmacology*, 159:121–139, 2019.

[29] Falls KC et al. Radiation-drug combinations to improve clinical outcomes and reduce normal tissue toxicities: Current challenges and new approaches: Report of the symposium held at the 63rd annual meeting of the radiation research society. *Radiat Res*, 190(4):350–360, 2018.

[30] Schaue D. A century of radiation therapy and adaptive immunity. *Front Immunol*, 8(431), 2017.

[31] Halperin EC et al. *Perez & Brady's principles and practice of radiation oncology.* Lippincott Williams & Wilkins, 2013.

[32] Desrosiers M et al. The importance of dosimetry standardization in radiobiology. *Journal of research of the National Institute of Standards and Technology*, 118(403), 2013.

[33] Stewart F et al. ICRP publication 118: ICRP statement on tissue reactions and early and late effects of radiation in normal tissues and organs–threshold doses for tissue reactions in a radiation protection context. *Annals of the ICRP*, 41(1-2):1–322, 2012.

[34] Ghita M et al. Small field dosimetry for the small animal radiotherapy research platform (SARRP). *Radiat Oncol*, 12(1):204, 2017.

[35] Brodin NP et al. Dosimetry Formalism and Implementation of a Homogeneous Irradiation Protocol to Improve the Accuracy of Small Animal Whole-Body Irradiation Using a Cesium-137 Irradiator. *Health Physics*, 110(201):S26, 2016.

[36] Yoshizumi T et al. Specific issues in small animal dosimetry and irradiator calibration. *International journal of radiation biology*, 87(10):1001–1010, 2011.

[37] Musolino SV. Absorbed Dose Determination in External Beam Radiotherapy: An International Code of Practice for Dosimetry Based on Standards of Absorbed Dose to Water; Technical Reports Series No. 398. *Health Physics*, 81(5):592–593, 2001.

[38] Peixoto J and Andreo P. Determination of absorbed dose to water in reference conditions for radiotherapy kilovoltage x-rays between 10 and 300 kV: a comparison of the data in the IAEA, IPEMB, DIN and NCS dosimetry protocols. *Physics in Medicine and Biology*, 45(3):563, 2000.

[39] Pedersen K et al. Radiation Biology Irradiator Dose Verification Survey. *Radiation Research*, 185:163–168, 2016.

[40] Trompier F et al. Investigation of the influence of calibration practices on cytogenetic laboratory performance for dose estimation. *International Journal of Radiation Biology*, 93(1):118–126, 2017.

[41] Seed TM et al. An interlaboratory comparison of dosimetry for a multi-institutional radiobiological research project: Observations, problems, solutions and lessons learned. *International journal of radiation biology*, 92(2):59–70, 2016.

[42] Thomas A et al. Commissioning and benchmarking a 3D dosimetry system for clinical use. *Med Phys*, 38(8):4846–4857, 2011.

[43] D T Burns and L Büermann. Free-air ionization chambers. *Metrologia*, 46(2):S9, 2009.

[44] Perichon N et al. Comparison between absorbed dose to water standards established by water calorimetry at the LNE-LNHB and by application of international air-kerma based protocols for kilovoltage medium energy x-rays. *Phys Med Biol*, 58(9): 2787–2806, 2013.

[45] Chica U et al. Study of the formalism used to determine the absorbed dose for low-energy x-ray beams. *Phys Med Biol*, 53(23):6963–6977, 2008.

[46] Poirier Y et al. Characterization of nanoDot optically stimulated luminescence detectors and high-sensitivity MCP-N thermoluminescent detectors in the 40–300 kVp energy range. *Med Phys*, 45(1):402–413, 2018.

[47] F Tillner et al. Pre-clinical research in small animals using radiotherapy technology - a bidirectional translational approach. *Zeitschrift fur Meditiniche Physik*, 24(4): 335–351, 2014.

[48] Chow JC. Depth dose dependence of the mouse bone using kilovoltage photon beams: a Monte Carlo study for small-animal irradiation. *Radiation Physics and Chemistry*, 79(5):567–574, 2010.

[49] Azimi R et al. Characterization of an orthovoltage biological irradiator used for radiobiological research. *J Radiat Res*, 56(3):485–492, 2015.

[50] Hayden BC et al. Hyperfractionated external beam radiation therapy in the treatment of murine transgenic retinoblastoma. *Archives of Opthamology*, 120(3):353–359, 2002.

[51] van Rongen E et al. Early and late effects of fractionated irradiation and the kinetics of repair in rat lung. *Radiother Oncol*, 17(4):323–337, 1990.

[52] Arndt C et al. Dosimetric calibration and characterization for experimental mouse thoracic irradiation using orthovoltage X rays. *Radiat Res*, 175(6):784–789, 2011.

[53] Xu J et al. MicroRNA-129-5p-mediated inhibition of autophagy enhanced the radiosensitivity of human colon cancer cells. *International Journal of Clinical and Experimental Pathology*, 9(12):12179–12187, 2016.

[54] Aldelaijan S et al. Dosimetry of biological irradiations using radiochromic films. *Physics in Medicine and Biology*, 58(10):3177, 2013.

[55] Huq MS et al. The effect on dose of kilovoltage x-rays backscattered from lead. *International Journal of Radiation Oncology*Biology*Physics*, 24(1):171–175, 1992.

[56] Haagen J et al. Effect of selective inhibitors of inflammation on oral mucositis: preclinical studies. *Radiother Oncol*, 92(3):472–476, 2009.

[57] Medina L-A et al. Use of an orthovoltage X-ray treatment unit as a radiation research system in a small-animal cancer model. *Journal of Experimental & Clinical Cancer Research*, 27(1):57, 2008.

[58] Hillman GG et al. Neutron or photon irradiation for prostate tumors: enhancement of cytokine therapy in a metastatic tumor model. *Clin Cancer Res*, 7(1):136–144, 2001.

[59] Woo M and Nordal R. Commissioning and evaluation of a new commercial small rodent x-ray irradiator. *Biomed Imaging Interv J*, 2(1):e10, 2006.

[60] Butterworth KT et al. Conventional in vivo irradiation procedures are insufficient to accurately determine tumor responses to non-uniform radiation fields. *International Journal of Radiation Biology*, 91(3):257–261, 2015.

[61] Izaguirre E et al. TH-C-204B-10: Implementation of a Small Animal Image Guided Microirradiator: The MicroIGRT. *Med Phys*, 37(6Part13):3457, 2010.

[62] Grams MP et al. Design and characterization of an economical 192Ir hemi-brain small animal irradiator. *International journal of radiation biology*, 90(10):936–942, 2014.

[63] Stojadinovic S et al. MicroRT—small animal conformal irradiator. *Med Phys*, 34 (12):4706–4716, 2007.

[64] Wong J et al. High-resolution, small animal radiation research platform with x-ray tomographic guidance capabilities. *International Journal of Radiation Oncology*Biology*Physics*, 71(5):1591–1599, 2008.

[65] R Thoraeus. A study of the ionization method for measuring the intensity and absorption of x-rays and of different filters used in therapy. *Acta Radiol.*, 15, 1932.

[66] Frank H. Attix and LeRoy DeLaVergne. Plate separation requirements for standard free-air ionization chambers. *Radiology*, 63(6):853–866, 1954.

[67] Berger M et al. Stopping Powers and Ranges for Electrons. http://physics.nist.gov/Star, 1999.

[68] Glenn F. Knoll. *Radiation Detection and Measurement.* Wiley, 4th edition, 2010. ISBN 978047013148.

[69] Almond P et al. AAPM's TG-51 protocol for clinical reference dosimetry of high-energy photon and electron beams. *Med. Phys.*, 26:1847–1870, 1999.

[70] Ritz V. Design of free-air ionization chambers for the soft x-ray region (20–100 kv). *Radiology*, 73:911–922, 1959.

[71] Grimbergen T et al. Correction factors for the NMi free-air ionization chamber for medium-energy x-rays calculated with the Monte Carlo method. *Phys. Med. Biol.*, 43:3207–3224, 1998.

[72] D. T. Burns. consistent set of calculated values for electron-loss and photon-scdatter corrections for parallel-plate free-air chambers. BIPM document CCRI(1)99-04, 1999.

[73] Uei-Tyng Lin and Chien-Hau Chu. Correction factors for the iner-improved free-air ionization chambers calculated with the monte carlo method. *Appl. Radiat. Isot.*, 64 (5):608–614, 2006.

[74] Mainegra-Hing E, Reynaert N, and Kawrakow I. Novel approach for the monte carlo calculation of free-air chamber correction factors. *Medical Physics*, 35(8):3650–3660, 2008. ISSN 2473-4209. doi: 10.1118/1.2955551. URL `http://dx.doi.org/10.1118/1.2955551`.

[75] D.W.O. Rogers. Low energy electron transport with EGS. *Nucl. Instr. Meth. Phys. Res.*, 227(3):535–548, 1984.

[76] Seltzer S and Berger M. Bremsstrahlung spectra from electron interactions with screened atomic nuclei and orbital electrons. *Nucl. Instr. Meth. Phys. Res. B*, 12: 95–134, 1985.

[77] Seltzer S and Berger M. Bremsstrahlung energy spectra from electons with kinetic energy from 1 keV to 10 geV incident on screened nuclei and orbital electrons of neutral atoms with z = 1-100. *Atomic Data DNA Nuclear Data Tables*, 35:345–418, 1986.

[78] Tessier F and Kawrakow I. Calculation of the electron-electron bremsstrahlung cross-section in the field of atomic electrons. *Nucl. Instr. Meth. B*, 266:625–634, 2008.

[79] Koch H and Motz J. Bremsstrahlung cross-section formulas and related data. *Rev. Mod. Phys.*, 31:920–955, 1959.

[80] Berger M and Hubbell J. XCOM: Photon cross sections on a personal computer. Technical Report NBSIR87-3597, 1987.

[81] J Moga. *Characterization of low-energy photon-emitting brachytherapy sources and kilovoltage x-ray beams using spectrometry.* PhD thesis, University of Wisconsin-Madison, 2011.

[82] D. T. Burns et al. Evaluation of measurement data - guide to the expression of uncertainty in measurement. JCGM 100:2008, 2008.

[83] Borges de Oliveira F et al. Experimental investigation of surface determination process on multi-material components for dimensional computed tomography. *Case Studies in Nondestructive Testing and Evaluation*, 6:93–103, 2016.

[84] Ross C. K. Comments on 'Ionization chamber volume determination and quality assurance using micro-CT imaging'. *Phys. Med. Biol.*, 54:23–27, 2009.

[85] Rogers DWO et al. nrc user codes for egsnrc. Technical Report PIRS-702, 2011.

[86] Rogers DWO and Treurniet J. Monte Carlo calculated wall and axial non-uniformity corrections for primary standards of air kerma. Technical Report PIRS-663, 1999.

[87] Rogers DWO and Bielajew A. Monte Carlo calculated wall and axial non-uniformity corrections for primary standards of air kerma. *Phys. Med. Biol.*, 35(8):1065–1078, 1990.

[88] Mainegra-Hing E and Kawrakow I. Efficient x-ray tube simulations. *Med. Phys.*, 33 (8):2683–2690, 2006.

[89] Ding GX et al. Accurate patient dosimetry of kilovoltage cone-beam CT in radiation therapy. *Med. Phys.*, 35(3):1135–1144, 2008.

[90] Michael J. Lawless. *Development of Kilovoltage X-ray Dosimetry Methods and Their Application to Cone Beam Computed Tomography.* PhD thesis, University of Wisconsin-Madison, 2016.

[91] Wulff J et al. Efficiency improvements for ion chamber calculations in high energy photon beams. *Med. Phys.*, 35:1328–1336, 2008.

[92] Hill A. Half value layer measurements to facilitate patient dose assessment for newer CT scanners using published normalized dose data. *The British Journal of Radiology*, 72(860):792–798, 1999.

[93] Natalie N. Viscariello. *Characterization and dosimetry of radiobiology x-ray irradiators*. PhD thesis, University of Wisconsin-Madison, 2019.

[94] Dosimetry in Diagnostic Radiology: An International Code of Practice. *IAEA Report No 457*, pages 55–85, 2007.

[95] New York City Health Code Article 175. § 175.69(b). 2019.